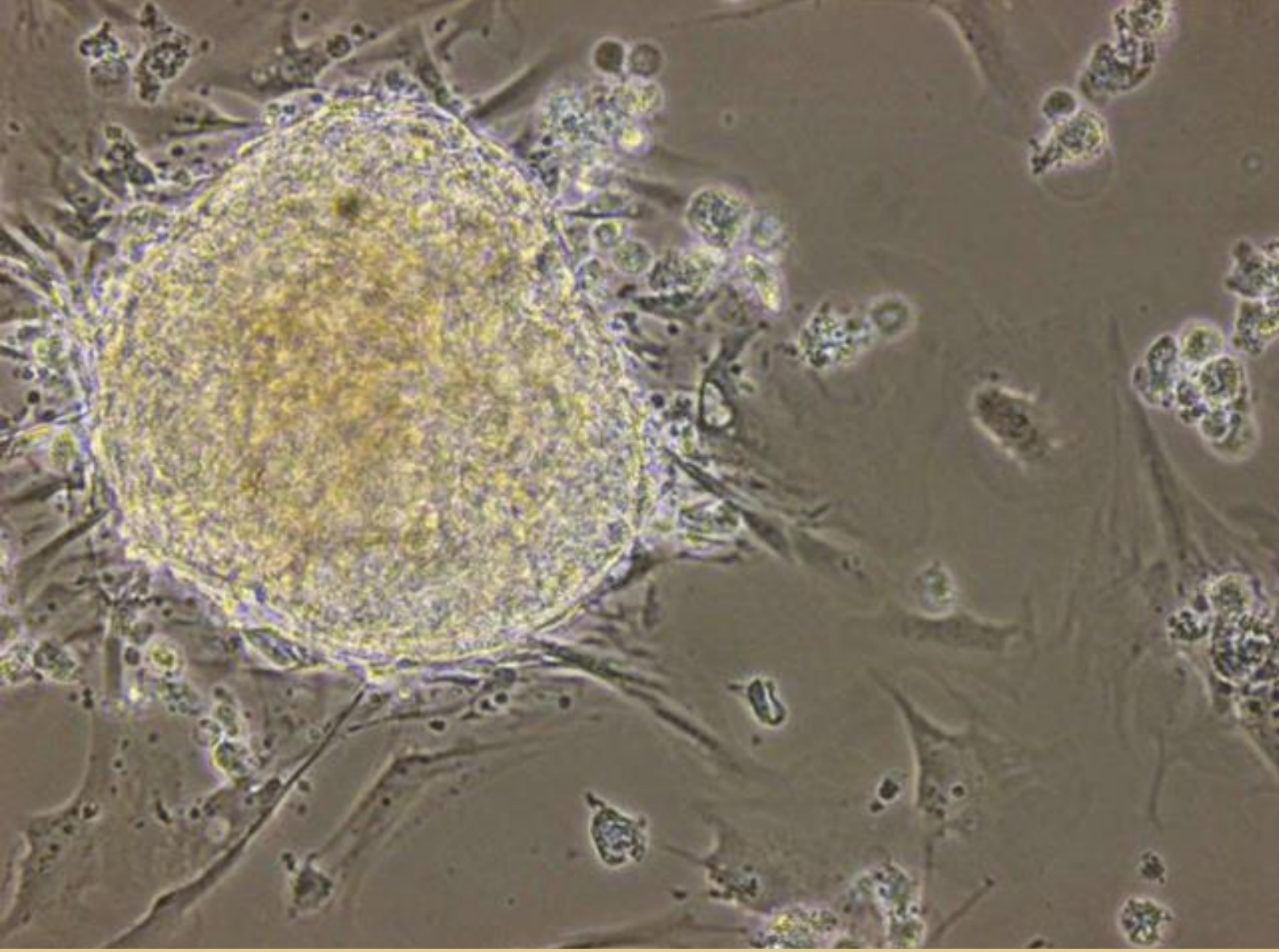

Ana Marguerita Martins Metelo

Therapeutic targeting of CNS Hemangioblastomas in VHL disease

Tese de Doutoramento em Biociências no ramo de especialização em Bioquímica, orientada pelo Professor Othon Iliopoulos e pela Professora Margarida Castro, e apresentada ao Departamento de Ciências da Vida da Faculdade de Ciências e Tecnologia da Universidade de Coimbra.

Setembro de 2016

· U C ·

Universidade de Coimbra

UNIVERSIDADE DE COIMBRA

Therapeutic targeting of CNS Hemangioblastomas in VHL disease

by Ana Marguerita Martins Metelo

Keywords: VHL disease, CNS tumors, hemangioblastomas, targeted therapy, somatic mutations

Tese de Doutoramento em Biociências no ramo de especialização em Bioquímica, orientada pelo Professor Othon Iliopoulos da Escola Médica de Harvard e do Hospital Geral de Massachusetts e pela Professora Margarida Castro do Departamento de Ciências da Vida da Faculdade de Ciências e Tecnologia da Universidade de Coimbra.

Doctoral thesis in Biosciences in the field of Biochemistry, supervised by Professor Othon Iliopoulos from Harvard Medical School and Massachusetts General Hospital and by Professor Margarida Castro from the Department of Life Sciences of the Faculty of Sciences and Technology of the University of Coimbra.

The study presented in this dissertation was supported by a PhD grant from the Portuguese Foundation for Science and Technology, FCT (SFRH/BD/70002/2010).

Therapeutic targeting of CNS Hemangioblastomas in VHL disease

Ana Marguerita Martins Metelo, M.Sc.

TABLE OF CONTENTS

Acknowledgments

I would like to thank my mentor, Othon Iliopoulos, for this inspiring and life-changing opportunity, and for all his guidance and support throughout this journey. He taught me why we should do science and how we should do it. I would like to thank Margarida Castro, for her incredible help and true friendship during all these years. I would like to thank Pilar López, for understanding and supporting all my decisions, and for all her scientific and personal contribution to this doctoral work.

I would like to thank to the many collaborators I had the opportunity to work with during these past five years. This doctoral thesis represents a true collaboration effort between several teams and I would like to thank to all of them. Especially I would like to thank Randall Peterson, Joanna Yeh, Gad Getz, Anat Stemmerrachamimov, Nick Dyson, Andrea Mcclatchey, Mario Suva, Jeff Engelman, David Langenau, Mo Motamedi, David Ting, Daniel Haber and their amazing teams for all the insightful interactions and learning experiences.

I would like to thank to all my friends and colleagues in the Center for Cancer Research at Massachusetts General Hospital. I learned from many of them, from all around the world, and they helped me every step of the way.

I would like to thank to all the past and present members of the Iliopoulos lab, for all their time, help, scientific discussions and fun work environment. Especially, I would like to thank my friends Meike, Laura and Julien for being my lab mates and friends, for helping and teaching me daily and for making my days so much happier! Danke! Merci beaucoup!

I would like to thank my special and forever team mate, Haley! She started in the lab in 2014 and quickly became my right and left hands together! I loved every day and every holiday we spent working together…she is the best scientific partner anyone can have! *Everyday amazing* my dear friend!

I would like to thank everyone in Pilar Lopez's lab in Madrid. Since my time there and during all these years, they have been amazing! A special thank goes to my friend Rocio!

Finally, I would like to thank to all my Portuguese friends in Boston, who followed me closely and allowed me to feel home several times. A special thank goes to my friend Inês, my PhD mate, who followed my work and my life every single day.

Eu gostaria de agradecer à minha mãe, a minha melhor amiga, por me acompanhar sempre. Por me dar força quando preciso e, principalmente, por partilhar a felicidade e emoção das minhas grandes conquistas! Eu gostaria de agradecer ao meu Pai, por todo o apoio, dedicação e motivação constantes, ao longo de toda a minha vida! Eu gostaria de agradecer ao meu irmão, o meu grande companheiro de infância, pelo orgulho, compreensão, companheirismo, e coragem...sempre! Eu gostaria de agradecer aos meus avós por estarem sempre ao meu lado! Eu gostaria de agradecer às minhas amigas, Dayana e Joanas, por me manterem sempre perto mesmo quando eu estou tão longe!

Eu gostaria de agradecer ao amor da minha vida, Paulo, com quem tenho a felicidade e sorte de partilhar os meus dias! Sem ti eu não seria quem sou hoje, não teria a carreira que tenho hoje e não estaria a terminar esta tese. Foste tu o maior impulsionador deste trabalho. Obrigada pela ajuda diária como cientista de excelência, como amigo e como homem da minha vida!

To my family…

Abstract

Central Nervous System Hemangioblastomas (CNS HBs) are benign and highly vascular tumors that arise most frequently in the cerebellum, brainstem, spinal cord and retina. These rare tumors are usually associated with the familial VHL disease, and eighty percent of VHL patients develop sequential or simultaneous HBs throughout their life. The only effective treatment for these lesions is surgery, which can be extremely challenging or impossible to perform due to the sensitive location of these tumors. The lack of scientific studies and experimental resources to study this tumor type strongly compromises the understanding of the disease and the discovery of effective treatments. The main goals of this doctoral work are the identification of novel therapeutic targets for CNS HBs, the testing of potential treatments in a zebrafish model of VHL disease and the establishment of a novel HB mouse model to clarify intriguing questions regarding the biology and cell of origin of HBs.

Taking advantage of HB human samples, we performed next-generation whole-exome sequencing to discover the main genetic alterations that occur in HB tumor cells. We discovered that complete inactivation of the *VHL* gene is necessary for HB formation. The inactivation of this gene occurred in both alleles for all tumors through germline mutations, copy number loss of chromosome 3, somatic point mutations and point deletions. Loss of chromosome 8 was also detected in two out of eight samples. In addition, we identified and confirmed a nonsense mutation in the *PNPLA3* gene. This specific mutation leads to loss of the acyl-transferase activity of the protein, diminishing the accumulation of lipid droplets characteristic of $VHL^{-/-}$ cells. Furthermore, we showed that downregulation of PNPLA3 is a recurrent event in VHL-associated tumors that occurs in both CNS HBs and clear cell renal cell carcinomas. Finally, we demonstrated that low levels of PNPLA3 in $VHL^{-/-}$ cancer cells stimulate oncogenic HIF2α signaling and promote a selective growth advantage in metabolic stress conditions.

Considering that disrupted VHL-HIF signaling is a hallmark of CNS Hemangioblastomas, we tested novel HIF2α small-molecule inhibitors as an innovative targeted strategy for the treatment of $VHL^{-/-}$ tumors. We used the only animal model of VHL disease that faithfully recapitulates the human phenotypes, which is the $vhl^{-/-}$ zebrafish embryo. These embryos develop pathologic angiogenesis with hypervascularization in the brain and in the retina mimicking CNS HBs, abnormal hematopoiesis, renal proliferation, cardiac abnormalities and severe edema. Treatment with the HIF2α inhibitor compound 76 ameliorates the pathologic vessel proliferation and abnormal hematopoiesis, improves the cardiac output and partially rescues the survival of $vhl^{-/-}$ embryos. Moreover, we showed that the VHL phenotype is specifically driven by HIF2α and not HIF1α, and these compounds specifically inhibit Epas1a and Epas1b, which are the zebrafish homologues of the human HIF2α.

In order to expand the scientific resources to study CNS HBs we established HB tumor-derived cell cultures. The highly heterogeneous polyclonal populations express HB tumor cell markers such as PDPN, VEGFα and HIF. Orthotopic injections of these HB-derived cells in the brain of immunocompromised mice generate proliferative brain tumors that recapitulate several features of the human CNS HBs, including their cellular histology and benign profile, the strong uptake of MRI contrast agents and the high lipid content. These characteristics highlight the potential of this model to study the HB disease.

In summary, this doctoral work led to: i) the identification of a novel mutation in CNS HBs, ii) the validation of HIF2α inhibitors for the treatment of VHL-associated phenotypes, and iii) the establishment of an unique mouse model crucial for the study of CNS HB biology and specific therapeutic strategies.

Resumo

Hemangioblastomas (HBs) são tumores benignos muito vascularizados que se desenvolvem em localizações específicas do Sistema Nervoso Central (SNC), maioritariamente no cerebelo, no tronco cerebral, ao longo da espinal medula e na retina. Estes tumores cerebrais são raros e estão muitas vezes associados à doença genética de VHL. Oitenta por cento destes pacientes desenvolvem vários HBs ao longo da sua vida, por vezes sequencialmente ou mesmo simultaneamente. O único tratamento recomendado é a remoção cirúrgica destes tumores cerebrais; contudo, devido à sensibilidade das áreas afectadas, este procedimento é muitas vezes dificultado ou mesmo impossibilitado. Actualmente, existe uma falta de estudos científicos e de modelos experimentais nesta área que permitam estudar a biologia dos HBs, o que compromete directamente o estudo das causas moleculares da doença e a descoberta de fármacos inovadores. Deste modo, os objectivos desta tese doutoral são a identificação de novos alvos terapêuticos em HBs do SNC, o teste de potenciais novos fármacos num modelo peixe-zebra (*Danio rerio*) da doença de VHL e, finalmente, o desenvolvimento de um novo modelo animal de ratinho para estudar a biologia destes intrigantes tumores cerebrais.

A partir de amostras humanas de HBs do SNC, procedeu-se à sequenciação completa do exoma tumoral através de técnicas inovadoras de sequenciação de "nova geração", de forma a identificar mutações genéticas características das células tumorais de HB. Através destes resultados, descobriu-se que a inactivação de ambos os alelos do gene de *VHL* ocorre em todos os tumores e é necessária para o desenvolvimento tumoral. Este processo ocorre através de vários mecanismos genéticos que afectam ambos os alelos do gene de *VHL* incluindo: mutações génicas de substituição, mutações génicas de perda de nucleótidos ou perda do cromossoma 3 (onde se localiza o gene de *VHL*). Outras alterações detetadas no cariótipo das células tumorais incluem a perda do cromosoma 8, que foi detectada pela primeira vez em duas amostras de HB. Finalmente, foi identificada uma mutação oncogénica de substituição no gene *PNPLA3*, que origina um codão de terminação prematuro (mutação de substituição "sem sentido"). Esta mutação específica leva à perda da função enzimática da proteína PNPLA3, causando uma diminuição na quantidade de vacúolos lipídicos característicos das células tumorais $VHL^{-/-}$. A diminuição nos níveis da proteína PNPLA3 é na verdade uma característica recurrente de células $VHL^{-/-}$, ocorrendo não só em células tumorais de HB mas também em células tumorais de carcinoma renal. Finalmente, foi demonstrado que a diminuição dos níveis da enzima PNPLA3 especificamente em células $VHL^{-/-}$ promove a via de sinalização tumorigénica dependente de HIF2α e leva a um crescimento seletivo das células cancerígenas em condições metabólicas específicas.

Uma das características dos HBs do SNC é o aumento patológico dos factores de transcrição HIF e a activação das respectivas vias de signalização como consequência de mutações no gene *VHL*. Deste modo, inibidores do oncogene HIF2α foram testados num modelo peixe-zebra (*Danio rerio*) da doença de VHL como potencial estratégia inovadora para o tratamento desta doença. O modelo animal usado é o único actualmente disponível para estudar a doença de VHL e mimetiza muitos dos fenótipos observados em pacientes com esta doença. Estes embriões peixe-zebra com mutação no gene *vhl* desenvolvem uma extensa vascularização e angiogénese no cérebro e na retina, defeitos no processo de hematopoiese, proliferação anormal das células epiteliais do rim, anomalias cardíacas e edema generalizado. Neste estudo, foi demonstrado que o tratamento de embriões $vhl^{-/-}$ com o inibidor de HIF2α designado "composto 76" melhora significativamente as anomalias identificadas nestes animais, incluindo os

processos angiogénico e hematopoiético, o rendimento cardíaco e ainda a sobrevivência dos embriões *vhl*$^{-/-}$. Finalmente, foi também mostrado que os fenótipos observados neste modelo animal são causados directamente pelo oncogene HIF2α, e não pela sua isoforma (denominada HIF1α), sendo que o inibidor "composto 76" é específico para o alvo HIF2α e inibe unicamente as suas proteínas homólogas *epas1a* e *epas1b* presentes no peixe-zebra.

De modo a expandir o material científico para estudo dos HBs do SNC, foram estabelecidas culturas de células a partir de biópsias de tumores de hemangioblastoma. Estas culturas celulares são bastante heterogéneas e expressam marcadores celulares característicos de células tumorais de HB, tais como as proteínas PDPN, VEGFα e HIF. Injeções ortotópicas destas células no cérebro de ratinhos imunosuprimidos levaram ao desenvolvimento de tumores cerebrais que mimetizam as características dos HBs do SNC em humanos, como por exemplo a histologia do tumor, o seu comportamento benigno e não-invasivo, a captação de agentes de contraste usados em resonância magnética de imagem e, finalmente, a acumulação de lípidos intracelulares. Estas características provam que este modelo de ratinho mimetiza a doença em humanos e deve ser usado para o estudo de HBs do SNC.

Em suma, o trabalho doutoral aqui apresentado levou aos seguintes resultados científicos: 1) identificação de uma nova mutação no gene *PNPLA3* em tumores de HB; 2) validação de um composto terapêutico inibidor da proteína HIF2α para o tratamento dos fenótipos associados à doença de VHL num modelo de peixe-zebra; 3) desenvolvimento do primeiro modelo tumoral de HB em ratinho, o que será essencial para o estudo da biologia destes tumores cerebrais e para o teste de potenciais estratégias terapêuticas.

List of Abbreviations

ADC – Apparent Diffusion Coefficient

ARNT – Aryl Hydrocarbon Receptor Nuclear Translocator

ATP - Adenosine Triphosphate

BSA – Bovine Serum Albumin

ccRCC – clear cell Renal Cell Carcinoma

cDNA – complementary DNA

CE-T1W – Contrast-Enhanced T1-weighted

CHT – Caudal Hematopoietic Tissue

CNS – Central Nervous System

DMEM - Dulbecco's Modified Eagle's Medium

DNA - Deoxyribonucleic Acid

EDTA - Ethylenediaminetetraacetic Acid

EGFP/GFP – Green Fluorescent Protein

EGLN/PHD - Egl nine homolog/Prolyl Hydroxylase Domain containing protein

EMT – Epithelial-Mesenchymal Transition

EPO - Erythropoietin

EPOR – Erythropoietin Receptor

FBS – Fetal Bovine Serum

FDA – US Food and Drug Adminstration

FFPE – Formalin-fixed Paraffin-embedded

gDNA – genomic DNA

HBs - Hemangioblastomas

HIF1α – Hypoxia-inducible Factor 1 alpha

HIF2α – Hypoxia-inducible Factor 2 alpha

HRE – Hypoxia Responsive Element

HRP – Horseradish Peroxidase

HUVEC – Human Umbilical Vascular Endothelial Cells

KO - Knockout

LOH – Loss-of-Heterozygosity

MO - Morpholino

MRI/MRS – Magnetic Resonance Imaging/Spectroscopy

NOD/SCID mouse – Non-obese diabetic/severe combined immunodeficiency mouse

NOS2 – Nitric Oxide Synthase 2

PCR – Polymerase Chain Reaction

PDGFβ - Platelet Derived Growth Factor Subunit Beta

PDGFβR - Platelet Derived Growth Factor Subunit Beta Receptor

PDPN - Podoplanin

qRTPCR – quantitative Real-Time Polymerase Chain Reaction

RBC – Red Blood Cells

RNA - Ribonucleic Acid

RPM – Rotations Per Minute

RT – Room Temperature

SDS – Sodium Dodecyl Sulfate

shRNA – short hairpin RNA

T1W – T1-weighted

T2W – T2-weighted

TCA cycle - Tricarboxylic Acid Cycle

TCGA - The Cancer Genome Atlas

TGFα – Transforming Growth Factor alpha

TKI – Tyrosine Kinase Inhibitor

VEGFα – Vascular Endothelial Growth Factor alpha

VEGFR2 – Vascular Endothelial Growth Factor Receptor

VHL – Von-Hippel Lindau

CHAPTER 1

Introduction

The Chapter 1 of this doctoral thesis is based on the review of the literature previously published in:

Metelo AM. and Iliopoulos O. (2015) Rosenberg's Molecular and Genetic Basis of Neurological and Psychiatric Disease. Academic Press, 5th Edition, 82: 955-959.

1.1. Central Nervous System Hemangioblastomas

Hemangioblastomas (HBs) are benign tumors that develop in specific locations of the Central Nervous System (CNS). Most commonly in the cerebellum (60%), followed by spinal cord (59%), retina (58%) and optic nerve, brainstem (16%), and less often in supratentorial regions (12%) such as the hypothalamus [1,2]. Although rarely, there are some reported cases of hemangioblastomas outside of the CNS including the spinal nerve roots, liver, kidney, stomach, intestine, pelvic and peritoneal cavities and skin [3–5]. ***Figure 1*** depicts the incidence of CNS Hemangioblastomas along the human spinal cranial axis and classic Magnetic Resonance Imaging (MRI) images of cerebellar, brainstem and spinal Hemangioblastomas.

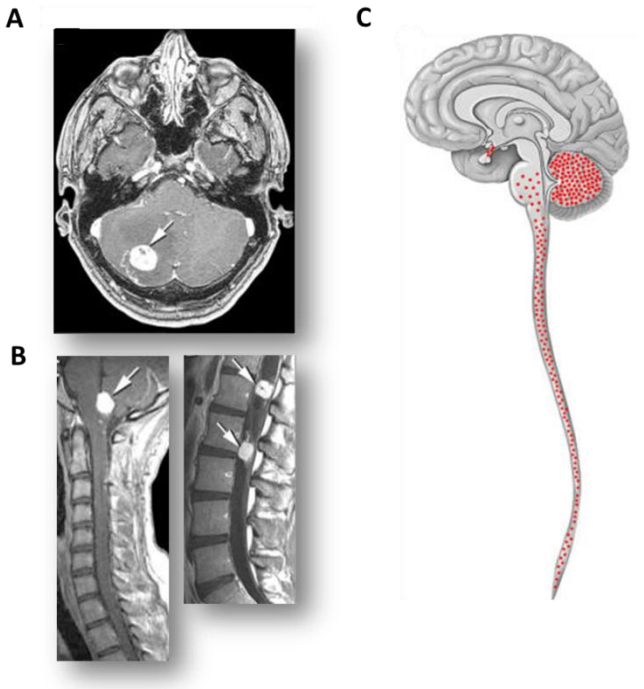

Figure 1 – Incidence of Hemangioblastomas within the Central Nervous System. (A) Representative MRI images of CNS HBs presented in the cerebellum, **(B)** brainstem and spinal cord. **(C)** Most HBs develop in the cerebellum and spinal cord, followed by retina, brainstem and hypothalamus. Image modified from [6].

These benign tumors are usually associated with the Von-Hippel Lindau syndrome (VHL), which is a genetic disorder that affects entire families with an incidence of 1 in 36.000 people around the world [7,8]. VHL patients are characterized by a germline mutation in one *VHL* allele that has 50% chance of being carried to the next generation. According to Knudson's "two-hit" hypothesis [9], loss-of-heterozygosity (LOH) upon inactivation of the second *VHL* allele leads to the development of multiple tumors in different organs including renal cell carcinomas, pheochromocytomas and most commonly CNS Hemangioblastomas [1]. Between sixty and eighty percent of VHL patients will develop multiple synchronous and/or sequential CNS HBs in their lifetime. The mean age of onset is between 25 and 30 years-old but retinal HBs can develop in patients younger than 10 years-old [1,2].

Hemangioblastomas can also appear sporadically, not associated with the VHL genetic disease, although they are usually single lesions that develop later in life. ***Table 1*** describes the differences between VHL-associated and Sporadic Hemangioblastomas in patients.

Table 1 - Clinical features of VHL-associated Hemangioblastomas compared to Sporadic Hemangioblastomas.

Hemangioblastomas		VHL-associated	Sporadic
Mean age of onset		25 years old	50 years old
Number of Hemangioblastomas		Multiple	Single
Location	Cerebellum	60%	Common
	Spinal Cord	59%	Very unusual
	Brain Stem	16%	Very unusual
	Supratentorial	12%	Very unusual
	Retinal	58%	Extremely rare
	Rare locations	Meningeal, liver, skin	---
Associated with		Renal Cell Carcinoma	---
		Pheochromocytoma	---
		Pancreatic Neuroendocrine Tumor	---
		Papillary Cystadenomas	---

1.2. The pathophysiology of CNS Hemangioblastomas

Hemangioblastomas are formed by two main cellular components: large vacuolated tumor cells of unknown origin called "*stromal cells*" and a very rich network of endothelial cells and pericytes [10]. In addition, some tumors are known to have a strong hematopoietic compartment with the presence of red blood cells and, in some cases, mast cells [11,12].

The network of endothelial cells and tumor *stromal* cells in CNS Hemangioblastomas is extremely dense, being pathologically challenging to distinguish between collapsed blood vessels and tumor cells. The vascularization of this tumor type is complex and leaky, which contributes to the formation of a cystic fluid adjacent to the tumor mass, as shown by proteomic profiling [13,14]. HBs are among the most vascularized tumors in the CNS and the blood brain barrier is thought to be disrupted within the lesion areas due to the impaired blood vessel structure. This feature gives the CNS Hemangioblastomas a characteristic magnetic resonance image (MRI) with robust uptake of gadolinium contrast agents and a bright contrast-enhanced T1-weighted MRI [15]. The adjacent peritumoral cyst can be highlighted using a T2-weighted MRI sequence [14].

Hemangioblastomas can be divided into two different categories: *mesenchymal* hemangioblastomas and *epithelioid* hemangioblastomas. The *mesenchymal* subtype is characterized by individual tumor cells involved in an abundant network of capillaries, while the *epithelioid* subtype has predominant clusters of tumor cells described as zellballen nests [16]. *Epithelioid* tumors are less common than *mesenchymal* tumors (approximately 11.4% of total hemangioblastomas) and have worst prognosis, with high proliferation index, presence of recurrence events and shorter progression-free survival [16,17].

Hemangioblastomas are also stratified according to the presence or absence of extra-medullary hematopoiesis. Some hemangioblastomas are able to form blood islands, similar to the blood island formation that occurs during embryonic development, giving rise to primitive red blood cells and other hematopoietic cells *in situ* [11,12]. In 2008, Shively and colleagues hypothesized that there is a differentiation process during HB evolution, which culminates with the presence of extra-medullary hematopoiesis [18]. A small vascularized *mesenchymal* tumor of low-proliferating and poorly differentiated cells is believed to evolve towards a fast-growing *epithelioid* structure able to conduct hematopoiesis *in situ*. Accordingly, the *epithelioid* histology is only found in tumors of larger size and the presence of extra-medullary hematopoiesis is restricted to those *epithelioid* areas [18].

1.3. The unknown origin of CNS Hemangioblastomas

Hemangioblastomas are formed by different cellular components of unclear origin: tumor *stromal* cells, endothelial cells, pericytes and, occasionally, hematopoietic cells [10]. The *stromal* cells harbor the complete *VHL* inactivation and are considered the malignant cells [13,19]. Yet, they appear in a tight interaction with the endothelial compartment, forming a complex vascular network capable of extramedullary hematopoiesis, and the interaction between these different cell types is not well understood. During the last decades, several immunohistochemistry studies aimed to identify the precursor cell of HB *stromal* cells within the CNS, including: glial cells, arachnoid cells, embryonic choroid plexus cells, neuroendocrine cells, fibrohistiocytic cells, neuroectodermal-derived cells and heterogeneous cell populations. To this end, these previous studies focused mainly on glial and neuronal markers, such as factor XIIIa, factor VIII and glial fibrillary astrocytic protein (GFAP) [20–22], or classic neuronal markers, such as neuron-specific

enolase (NSE), neural cell adhesion molecule (NCAM), vimentin and S100 [20,23]. However, most of the described biochemical markers were not consistently expressed in different HB samples thereby preventing a clear identification of the HB cell of origin.

The ability to form hematopoietic cells and endothelial cells *in situ* suggests that HB *stromal* cells might derive from a committed or pluripotent stem cell with angiomesenchymal origin [10,11]. One possible precursor cell could be the *hemangioblast,* a transient progenitor cell formed in the mesoderm during embryonic gastrulation with the potential to originate two distinct cellular lineages: endothelial and hematopoietic. Hemangioblasts are identified by the simultaneous expression of Brachyury and VEGFR2 [24,25]. Additionally, these cells express the mesodermal marker stem-cell leukemia factor (SCL), the endothelial marker Tie2/Angiopoietin 2 and the hematopoietic markers Gata-1 and Csf-1R [24,26]. Interestingly, and following the identification and characterization of the hemangioblast cell *in vitro* and *in vivo* [24,27,28], one study showed that HB *stromal* cells co-express all the hemangioblast-specific proteins [29]. Therefore, one current idea is that CNS HBs are formed by developmentally-arrested hemangioblasts or embryonic progenitors with hemangioblastic potential. In line with this hypothesis, multiple developmentally-arrested structures were found in the cerebellum and spinal cord in VHL patient autopsies[30–32]. Although not fully developed, these embryonic structures express HIF2α and CD31 and therefore are believed to be the precursor lesions of CNS HB tumors.

The idea of an embryonic origin for HBs is further supported by the presence of fetal hemoglobin in these tumors and co-expression of erythropoietin ligand (EPO) and erythropoietic receptor (EPOR), which suggests an embryonic blood island formation within the tumor mass [11]. Additionally, Parker and colleagues demonstrated that HB tumor cells can differentiate into precursor red blood cells and granulocytes *in vitro* in the presence of erythropoietin, supporting

the hematopoietic potential of these tumors [6]. Finally, the expression of OCT4 (an embryonic pluripotency marker) and CD133 (a neural stem cell and brain cancer stem cell marker) in HBs corroborates the idea of an embryonic multipotent undifferentiated HB *stromal* cell [6,33–36].

Altogether, these studies highlight the heterogeneous cellular markers present in HB tumor cells but they do not describe the tumor precursor cell or the interaction between the different cellular components. Unbiased and detailed studies using whole-transcriptome profiling and lineage tracing experiments are necessary to identify the cell of origin and evolutionary pattern of CNS HB tumors. Currently, the pathologic diagnosis of HB tumor cells is based on the expression of podoplanin (PDPN), a transmembrane glycosylated protein involved in the embryonic development of the lymphatic and vascular systems [37]. While CD31 and CD34 are commonly used to identify the vascular and hematopoietic components of HB tumors, PDPN is specifically expressed in HB *stromal* cells, being used to distinguish CNS HB tumors from ccRCC brain metastases [37,38]. The expression of inhibin A, a hormone involved in the female reproductive system, can also be used to distinguish CNS HBs from brain metastases [39].

1.4. Clinical Features of CNS Hemangioblastomas

Hemangioblastomas are benign tumors with very rare cases of metastatic dissemination[3,40]. However they can impose life-threating complications, especially when remained untreated. The symptoms caused by HBs depend on the tumor location and the size of the tumor, and include cerebellar ataxia, pain and dysesthesia, peripheral motor and sensory symptoms, secondary erythrocytosis, retinal hemorrhage and blindness [1,41]. The clinical symptoms of HBs are often caused by a pseudo-cyst that, as described earlier, can develop adjacent to the benign tumor. The cyst is formed by a sac that accumulates fluid and makes

pressure against the nearby neuronal structures, causing the HB-associated neurologic symptoms. A recent study showed that 60% of the VHL-associated HBs patients develop peritumoral cysts[42].

The clinical management of CNS Hemangioblastomas is primarily surgery. Complete resection of the tumor mass is necessary to reduce tumor recurrence and cyst growth [43]. Radiation therapy is applied to control small size tumors without cystic component and with a clear safe margin from healthy tissue [44,45]. However, the control of tumor growth diminishes with long-term treatment and it should only be used for the treatment of tumors that cannot be surgically removed [46]. Although surgical resection leads to an overall good prognosis due to the well circumscribed tumor area, the sequential and simultaneous development of these CNS tumors imposes a clinical problem. The mortality rate associated with HB surgical resection is approximately 8-20% with the major complications being operative massive bleeding and brainstem failure [47,48]. In addition, HBs in the brainstem, optic nerve and hypothalamus or other supratentorial region cannot be surgically removed, leading to blindness and life-threating conditions.

1.5. The VHL disease

Von Hippel-Lindau disease (VHL) is a familial cancer syndrome hereditarily transmitted along generations as it is characterized by a germline mutation in the *VHL* gene, located in the short arm of chromosome 3 (region 3p24-25) [49,50]. The specific germline mutation varies across VHL families with different inactivating mutations being associated with the disease: nonsense mutations, non-synonymous missense mutations, disruption of splicing sites, small point insertions/deletions and large intragenic deletions [51]. Ultimately, all of these mutations lead to

the inactivation of one *VHL* allele in every cell of the patient's body. Inactivation or loss of the second *VHL* allele is the initiating event that leads to tumor formation in specific tissues (*Knudson's two-hit hypothesis*) [9]. Patients with VHL disease develop multiple, sequential or simultaneous tumors during their life-time including hemangioblastomas of the central nervous system (CNS HBs), clear cell renal cell carcinomas (ccRCCs), pheochromocytomas, pancreatic neuroendocrine tumors, liver and pulmonary hemangiomas and finally, papillary cystadenomas in the pancreas, epididymis, adnexal organs and in the endolymphatic system of the inner ear. ***Figure 2*** resumes the cancer lesions and specific organs affected in VHL patients.

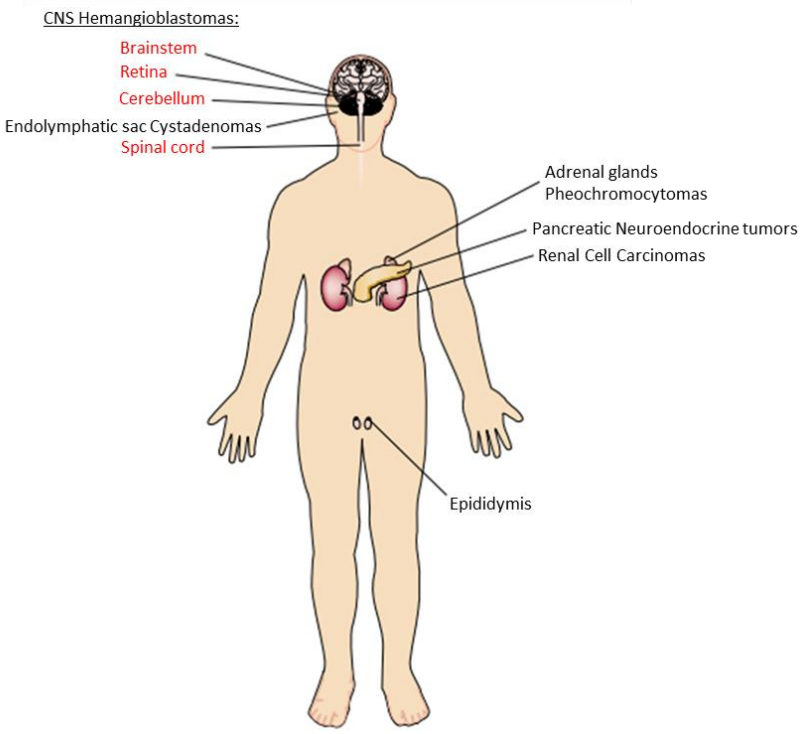

Figure 2 – Phenotypic lesions commonly developed in VHL patients. Hemangioblastomas develop in specific locations of the CNS mainly in the cerebellum, brainstem, spinal cord and retina (in red). Single and bilateral clear cell renal cell carcinomas appear often in the kidneys of VHL patients as well as pheochromocytomas in the adrenal glands. Cystadenoma lesions in the endolymphatic sac and pancreatic neuroendocrine tumors are less common. Image modified from [1].

Depending on the germline mutation and extend of *VHL* inactivation, VHL patients can be divided into two large categories: Type I and Type II (the latter sub-divides into IIA, IIB and IIC). Type I patients have large deletions or intragenic mutations that lead to the complete inactivation of the *VHL* gene. These patients develop HBs, ccRCCs and other VHL-tumors with the exception of pheochromocytomas. On the other hand, Type 2 mutations are usually missense mutations that can impact differently on the protein stability and VHL function [52]. Consequently, Type 2 patients develop pheochromocytomas but have low (IIA), high (IIB) or no incidence (IIC) of ccRCCs.

VHL patients are monitored every year to screen for the development of VHL-associated tumors. The most common lesions are CNS HBs (80% of patients) and ccRCCs (60% of patients) [1]. The standard of care for ccRCCs depends on the tumor grade and includes tumor resection with partial or complete nephrectomy, radiotherapy, chemotherapy and targeted therapy. Unfortunately, CNS Hemangioblastomas constitute a bigger challenge and represent the main cause of death among the VHL population [53].

In addition to VHL-associated tumors, the *VHL* tumor suppressor gene is also significantly mutated in sporadic ccRCCs, not associated with VHL disease. ***Figure 3*** describes the somatic mutations in the *VHL* gene found across different tumor types (pan-cancer samples).

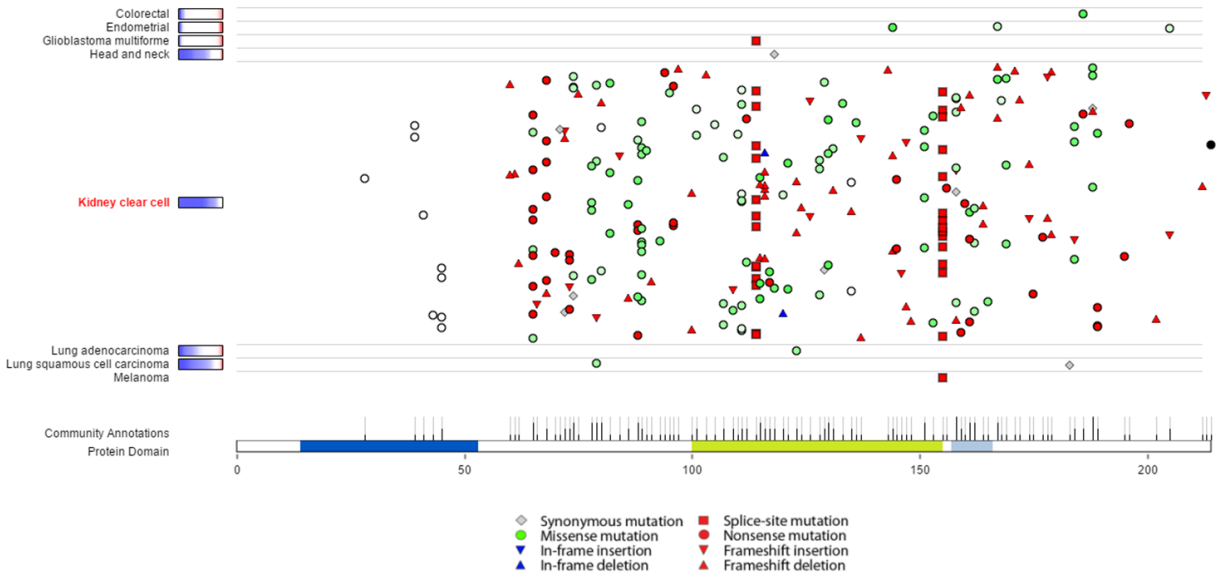

Figure 3 – Identified mutations in the *VHL* gene across pan-cancer samples. *VHL* is significantly mutated in sporadic clear cell renal cell carcinomas (Kidney clear cell) with a range of different mutations that lead to the loss-of-function of the protein. Adapted from tumorportal.org using data from Zack et al [54].

1.6. The VHL-HIF signaling pathway

The *VHL* tumor suppressor gene generates a 30KDa cytosolic protein. Internal translation leads to the synthesis of a smaller 19KDa isoform that is equally active, and sufficient to suppress tumor formation when introduced in $VHL^{-/-}$ cell lines [49,55]. VHL is an E3 ubiquitin ligase that selectively binds to hydroxylated-target proteins and signals their degradation through the proteasome by interacting with Cullin 2, Elongin B and Elongin C [56–58]. The first genes to be identified as VHL-target subtracts were the Hypoxia-inducible factor 1 alpha (HIF1α) and the Hypoxia-inducible factor 2 alpha (HIF2α) [59,60]. Of note, VHL is also known to have HIF-independent roles involving WNT signaling, cilia biogenesis and maintenance of the extracellular fibronectin matrix [61–63].

Hypoxia-inducible factors (HIFs) are heterodimeric basic helix-loop-helix transcription factors formed by the dimerization of one alpha (α) and one beta (β) subunits. In mammalian cells there are three α subunits (HIF1α, HIF2α and HIF3α) and two β subunits (HIF1β/ ARNT and ARNT2) [52]. The β subunits are constitutively expressed in the cell nucleus, while the α subunits are regulated by oxygen levels in the cytoplasm. In the presence of oxygen and 2-oxoglutarate, HIFα subunits are hydroxylated in two specific proline residues in their oxygen-dependent degradation domain (ODD). This enzymatic reaction is undertaken by a family of prolyl hydroxylases (PHD), also called EGLNs [64–67]. The two hydroxylated prolines are then recognized by and bound to the VHL protein. The HIFα-VHL binding recruits the complete E3 ubiquitin complex, leading to the ubiquitination of the HIFα proteins and their subsequent degradation in the proteasome, as depicted in ***Figure 4***.

In contrast, in conditions of low oxygen pressure (below 5% O_2), PHDs are inhibited and the HIFα subunits become stabilized in the cytoplasm, translocating to the nucleus through importin nuclear receptors [68]. Once in the nucleus, the HIFα subunit dimerizes with the nuclear HIFβ subunit to form the active HIF transcription factor (heterodimer), which binds to hypoxia-responsive elements (HRE) enriched in the promoter region of specific target genes. The binding of HIF transcription factors to HRE elements leads to the recruitment of additional protein cofactors such as p300 and CREB binding protein (CBP), resulting in activation of gene transcription at the target sites. The binding of these co-activators can also be inhibited by oxygen through the Factor Inhibiting HIF (FIH) that hydroxylates an asparagine residue of HIFα and thereby blocks the binding of p300 [69–71].

Mutations in the *VHL* gene leading to VHL loss-of-function mimic the hypoxic environment in the cell, since they promote to the stabilization of HIFα subunits in the

cytoplasm. As a result, VHL-associated tumors such as CNS HBs are known to maintain high levels of HIF1α and HIF2α proteins [32]. ***Figure 4*** illustrates the VHL-HIF signaling pathway in the absence of oxygen (hypoxia) or in conditions of loss of VHL function.

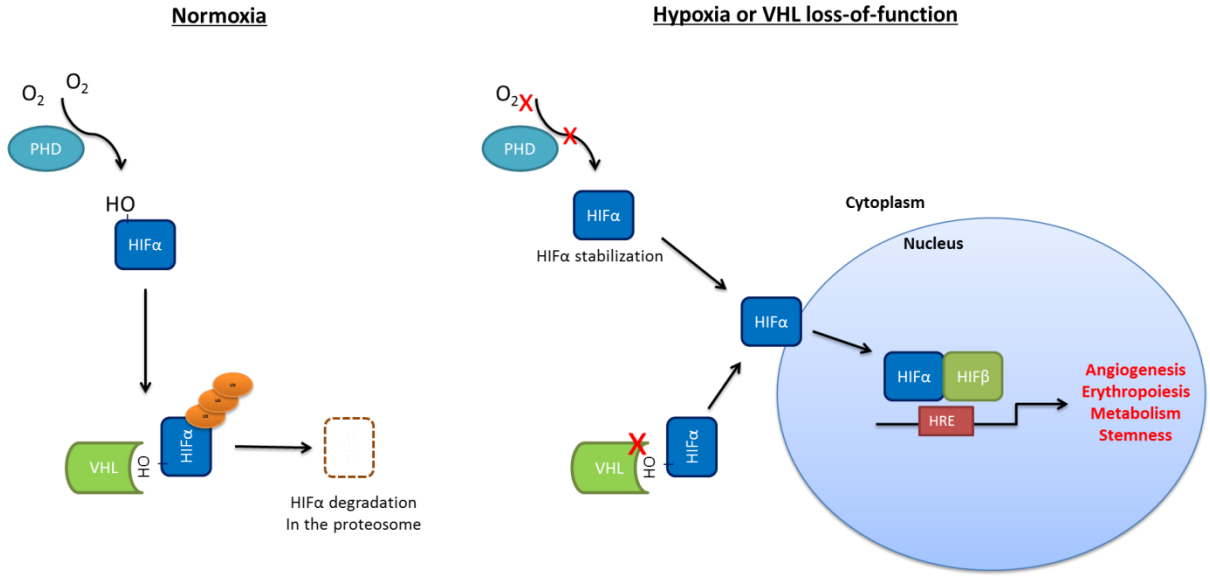

Figure 4 – The VHL-HIF signaling pathway in low oxygen conditions (hypoxia) or loss of VHL function. In normoxia conditions PHDs hydroxylate HIFα subunits that are consequently recognized by VHL and degraded in the proteasome. In conditions of low oxygen levels (hypoxia) or mutations that lead to VHL loss-of-function, the HIFα subunits are stabilized and translocate to the nucleus, where they activate specific target genes involved in angiogenesis, erythropoiesis, metabolic reprogramming and stemness.

The two main HIFα subunits are HIF1α and HIF2α (also known as EPAS1) and both dimerize with the β-subunit ARNT [72–76]. Although HIF3a and ARNT2 have been identified, their function remains unknown as well as their role in the cellular hypoxic response. For this reason, this thesis will focus on the transcription factors HIF1α and HIF2α as their link to cancer development is well established and studied.

1.7. HIF downstream signaling

The HIF1α and HIF2α transcription factors are the master regulators of the cellular response to hypoxia. In hypoxic conditions HIFs activate more than 300 specific-target genes involved in angiogenesis, erythropoiesis, stemness, anaerobic metabolism, growth and metastasis, in order to preserve cellular energy, restore oxygen supply and survive [52,77]. Angiogenesis is one of the main pathways activated under hypoxia conditions, which supports the branching of new blood vessels from existing ones [78]. Tumor angiogenesis is stimulated by HIF1α and HIF2α by promoting the secretion of pro-angiogenic factors such as Vascular Endothelial Growth alpha (VEGFα), Platelet Derived Growth Factor beta (PDGFβ) and Angiopoietin 2, all bona-fide HIF-target genes [77,79–81]. As a consequence VHL-associated tumors are especially angiogenic, presenting an extended network of impaired and leaky blood vessels. Angiogenesis is therefore a tumor phenotype characteristic of VHL-associated tumors, being therapeutically targeted using VEGFα and VEGF receptor 2 (VEGFR2) inhibitors as described below.

Erythrocytosis is another cellular process regulated by HIFs. Both the erythropoietin ligand (EPO) and the erythropoietin receptor (EPOR) are important HIF target genes [82,83]. These proteins are strongly involved in red blood cell proliferation and differentiation. Therefore, VHL patients commonly develop primary or secondary erythrocytosis (increased number of red blood counts), mostly caused by the high levels of EPO released by their VHL-associated tumors [1,41].

Metabolism remodeling is an important feature of hypoxic cells when compared to normal cells. The lack of oxygen inhibits the oxidative phosphorylation pathway and the cell prioritizes other metabolic pathways (such as glycolysis) to generate energy (ATP). This metabolic remodeling occurs through the presence of hypoxia responsive elements (HRE) in the

promoter regions of several metabolic enzymes, which are then activated upon binding of HIF1α and/or HIF2α transcription factors. Glucose uptake increases after overexpression of the HIF target gene *SCL2A1*/GLUT1 and glycolysis is stimulated during hypoxia by several glycolytic enzymes: Hexokinase 1 (*HK1*), Hexokinase 2 (*HK2*), Phosphofructokinase (*PFK1*), Aldolase (*ALDOA*), Phosphoglycerate kinase 1 (*PGK1*) and Lactate Dehydrogenase (*LDHA*) [77,84,85]. On the other hand, while the glycolytic flux is increased by HIFs, the entry of glycolytic products into the TCA cycle is inhibited by the expression of another HIF-target gene, Pyruvate Dehydrogenase (*PDK1*) [86,87]. The HIF-expressing cells become therefore dependent on glucose for ATP generation (using the glycolytic pathway) and dependent on glutamine for biomass production (through the TCA cycle) [88]. The direct use of glutamine to produce lipids utilizes a pathway described as *reductive carboxylation.* This metabolic pathway recently discovered by the *Iliopoulos lab and collaborators* is known to be a characteristic of hypoxic and cancer cells and it is now being clinically targeted [88,89].

In addition to the metabolic changes described above, hypoxic conditions have a profound impact on lipid metabolism. The degradation of fatty acids through the beta-oxidation pathway is repressed, as well as *de novo* biosynthesis of fatty acids from acetyl-coenzyme A (Acetyl-CoA) [90]. Therefore, hypoxic cells become therefore dependent on extracellular lipids and their intracellular lipid content increases dramatically. Consequently, large amounts of triglycerides are stored in cytoplasmic lipid droplets, forming the classic *clear cell phenotype* exhibited by ccRCC and HB tumor cells [91–93]. Perilipin 2 is also a HIF target gene and stabilizes the lipid droplet membrane, being upregulated in ccRCC tumors [92,94].

Both HIF1α and HIF2α are also important mediators of cell differentiation and embryogenic development, being involved in placental growth, cardiovascular morphogenesis, adipogenesis, bone morphogenesis, tracheal development and hematopoiesis [84,85,95,96].

Interestingly, embryonic stem cells require low oxygen conditions to maintain their full pluripotency [97]. While HIF1α is ubiquitously expressed in the embryo, HIF2α is restricted to certain tissues and developmental stages [98]. In fact, HIF1α and HIF2α specifically promote certain cell fates, stimulating the proliferation of CNS precursor cells [99], neural crest stem cells [100] and embryonic hemangioblasts [101].

Adult stem cell niches are also characterized by low oxygen levels, such as the bone marrow, where hematopoietic stem cells require HIFs to maintain their self-renewal and undifferentiated state [102,103]. Finally, hypoxia and HIFs have an important role in cancer development by promoting the survival and proliferation of undifferentiated and cancer stem cells [104]. NOTCH transcriptional targets and the known reprogramming factors OCT4 and MYC are strongly upregulated by HIF2α and are thought to be involved in the undifferentiated cell state caused by hypoxic conditions [105–107].

Finally, HIF transcription factors stimulate additional target genes known to be involved in cellular transformation and tumor development. The HIF-target gene transformed growth factor alpha (*TGFA*) is implicated in cellular transformation and cell growth [108,109]. *NOS2* and *IL6* are involved in inflammation and cancer [110–112]. The membrane type-1 metalloproteinase (*MMP14*), the lysyl oxidase (*LOX*) as well as the carbonic anhydrase 9 (*CA9*), carbonic anhydrase 12 (*CA12*) and *CXCR4* are HIF-target genes widely associated with cancer invasion and metastasis [113–116]. Moreover, overexpression of HIFs inhibits E-cadherin and promotes epithelial-mesenchymal transition (EMT), stemness and the metastatic potential of tumor cells[117].

In summary, while both HIF1α and HIF2α are linked to tumorigenesis in several cancer types, HIF2α (and not HIF1α) is the main validated oncogene in ccRCC, neuroblastoma and

glioblastoma multiform [77,108,118–122]. ***Table 2*** summarizes the main HIF-target genes involved in cancer development and progression.

Table 2 – List of target genes involved in cancer and directly activated by the HIF1α and HIF2α transcription factors.

Signaling Pathway	HIF-target Gene	Gene Name
Angiogenesis	*VEGFA*	Vascular Endothelial Growth Factor A
	KDR	Kinase Insert Domain Receptor/VEGFR2
	PDGFB	Platelet Derived Growth Factor B
	PDGFRB	Platelet Derived Growth Receptor Factor B
	ANGPT2	Angiopoietin 2
	TEK	TEK Receptor Tyrosine Kinase/Tie2
Erythropoiesis	*EPO*	Erythropoietin
	EPOR	Erythropoietin Receptor
Cell proliferation	*TGFA*	Transforming Growth Factor Alpha
	TGFB1	Transforming Growth Factor Beta 1
Metabolism	*SLC2A1*	Solute Carrier Family 2 Member 1/GLUT1
	HK1	Hexokinase 1
	HK2	Hexokinase 2
	ALDOA	Aldolase, Fructose-Bisphosphate A
	PGK1	Phosphoglycerate Kinase 1
	PFKL	Phosphofructokinase, Liver Type
	LDHA	Lactate Dehydrogenase A
	PLIN2	Perilipin 2
Metastasis	*CDH1*	Cadherin 1/E-Cadherin
	CXCR4	C-X-C Motif Chemokine Receptor 4
	CA9	Carbonic Anhydrase 9
	CA12	Carbonic Anhydrase 12
	MMP2	Matrix Metallopeptidase 2
	MMP9	Matrix Metallopeptidase 9
	TIMP1	TIMP Metallopeptidase Inhibitor 1
Stemness	*POU5F1*	POU Class 5 Homeobox 1/OCT4
	MYC	V-Myc Avian Myelocytomatosis Viral Oncogene Homolog

Most of the described bona fide HIF-target genes are expressed in CNS HBs. These highly angiogenic tumors produce high levels of VEGFα and VEGFR2 [123] as well as PDGFβ and its receptor PDGFβR [124,125], which strongly stimulate reactive angiogenesis. Other angiogenic markers such as Angiopoietin 2 and Tie2 have also been detected in human HB samples [29].

In addition, HBs express aberrant levels of EPO and EPOR, which produce secondary erythropoiesis in VHL patients [11] and might be responsible for the extramedullary hematopoiesis within the tumor mass. Both EPO/EPOR proteins contribute to a paracrine signaling pathway within the tumor microenvironment with potential formation of blood islands *in situ*. The hematopoietic receptor CXCR4 and its ligand SDF-1 are also produced by HB and ccRCC tumor cells [126], which might allow the recruitment of other hematopoietic cells to the tumor microenvironment. TGFα and EGFR are also expressed in HB tumor cells, which further potentiates tumor proliferation [127]. Finally, the undifferentiated state of HB stromal cells might be maintained by the expression of pluripotent HIF-target gene OCT4 [33]. The expression of all of these HIF downstream targets forms a complex tumor microenvironment within HB tumors, where different cells are stimulated by growth factors and correspondent receptors by autocrine and paracrine signaling mechanisms.

An additional signaling pathway involved in stem cell development known to be active in CNS HBs is the NOTCH pathway [128]. NOTCH receptors are not described as HIF-target genes; yet, the intracellular NOTCH domain has been shown to physically interact with the HIF1α subunit, increasing the NOTCH transcriptional activity through the recruitment of p300/CBP [107]. Overall these studies highlight the importance of HIF activation in the oncogenic pathways present in HB cells and the dependence of VHL-associated tumors on HIF expression. ***Image 5***

depicts the heterogeneity of HB tumors and pinpoints some HIF-target genes that contribute to this complex tumor microenvironment.

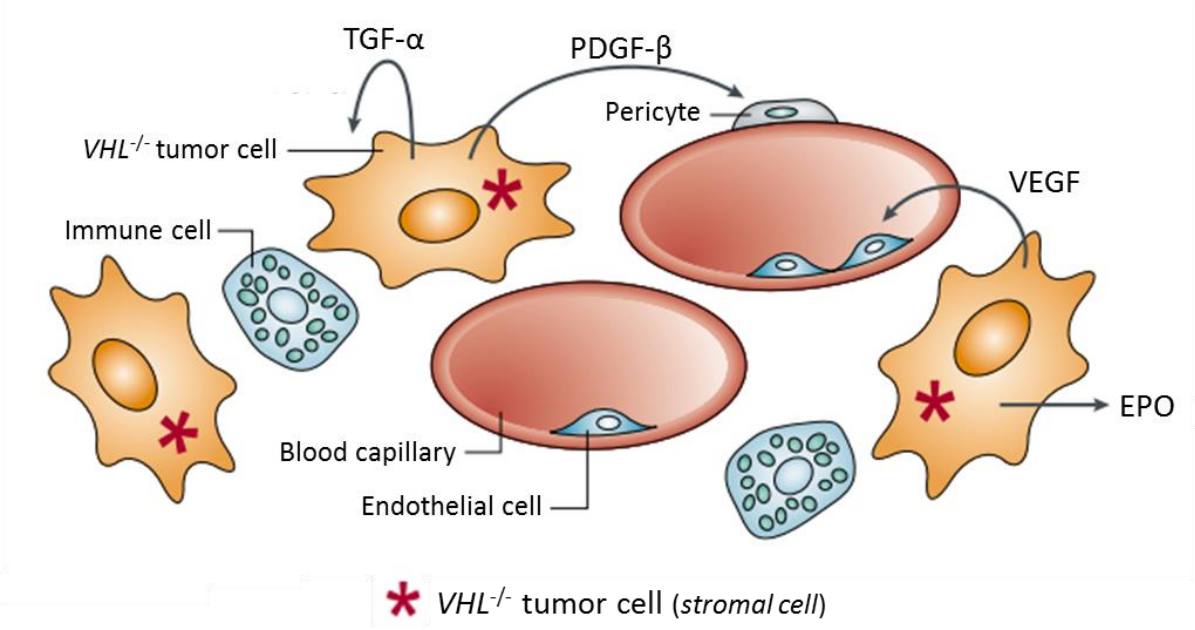

Figure 5 – Schematic representation of the cellular components and oncogenic pathways present in CNS Hemangioblastomas. CNS HBs are formed by VHL$^{-/-}$ tumor *stromal* cells (in orange), endothelial cells (in blue) lining the extensive blood vasculature (in red), pericytes and immune cells (such as mast cellsm in blue). TGFα, PDGFβ, VEGFα and EPO are all HIF-target genes directly involved in angiogenesis, erythropoiesis and cell proliferation pathways that sustain the tumor growth. Image modified from [129].

1.8. Targeted therapy in VHL-associated tumors

Targeted therapy takes advantage of the oncogenic dependence of tumor cells and is an innovative and exciting strategy to treat different tumor types. This method targets genes uniquely mutated in tumor cells, ideally not interfering with normal healthy cells. With the advances in sequencing technologies and the establishment of next-generation sequencing approaches, oncogenic mutations can now be detected and targeted in different tumor types [130–136]. Most of these studies are catalogued and funded by international platforms such as The

Cancer Genome Atlas (TCGA) (http://cancergenome.nih.gov/) or the International Cancer Genome Consortium (http://www.icgc.org/). One of the most successful cases of targeted therapy is the inhibition of mutant $BRAF^{V600}$ found in more than 40% of human melanomas (COSMIC. http://www.sanger.ac.uk/genetics/CGP/cosmic/)[137]. Mutated tumor cells depend on the constitutive active form of $BRAF^{V600}$ to grow; and small-molecule inhibitors of the mutated BRAF form, such as *Vemurafenib* and *Dabrafenib*, have resulted in landmark tumor regression responses in melanoma patients [138,139]. Other examples include the targeting of oncogenic EGFR, KRAS and PI3K in lung and colorectal cancers, among others [140–142].

VHL is a classic *tumor suppressor gene*. Driver mutations in *VHL* are the origin of tumor development and VHL-associated tumor cells depend on this mutational defect to survive. *VHL* is not only associated with the cancer syndrome *VHL disease* but it is also significantly mutated in sporadic ccRCCs [130]. One strategy to target VHL-associated tumors would be to design drugs against HIF2α, which was shown to be necessary for ccRCC tumor formation *in vivo* [119]. However, transcription factors are challenging molecules to target therapeutically and instead HIF-downstream targets were used for drug development.

Antiangiogenic therapy with anti-VEGF antibodies and anti-VEGFR2 tyrosine kinase inhibitors (TKI) are currently used as first-line drugs for the treatment of ccRCC [143]. The FDA-approved agents (*Sunitinib*, *Sorafenib*, *Bevacizumab* with IFN-α, *Pazopanib* and *Axitinib*) have been shown to significantly increase progression-free survival and/or overall survival of metastatic ccRCC patients, dramatically changing the treatment options and outcome of the disease [144–149]. More recently, new genomic studies have identified additional driver mutations in ccRCC tumors including mTOR, SETD2, BAP1 and PBRM1 [130]. mTOR inhibitors (such as *Temsirolimus* and *Everolimus*) are also now clinically approved for the treatment of these tumors

[150,151]. In summary, ccRCC tumors became a good example of the potential of targeted therapy strategies, with different drugs being used separately or in tandem to efficiently treat these tumors in the clinic. Unfortunately the same does not occur for CNS HBs.

The genomic landscape of CNS HBs remains largely unknown, which strongly compromises the development of new targeted therapies. Although VHL inactivation and enhanced HIF signaling are known to occur in CNS HB tumors, these tumors do not seem to respond to targeted agents that block HIF downstream targets. The current clinical protocol for CNS HBs relies mainly on surgery and only few studies evaluated the effect of targeted therapy for this tumor type. One study used the VEGFR2 inhibitor *Sunitinib* to simultaneously treat ccRCCs and CNS HBs in VHL patients [152]. While the ccRCC tumors decreased their size after *Sunitinib* treatment, the CNS HBs remained stable. Kim and colleagues evaluated the efficacy of *Pazopanib* in CNS HBs, a pan-tyrosine kinase inhibitor that targets not only VEGFR2 but also PDGFβR [153]. This study was performed in one VHL patient with several CNS HB tumors and showed a modest regression in 3 out of 5 tumors. A subsequent case study also described the use of *Pazopanib* to stabilize a 37 year-old VHL patient with fast-growing CNS HB lesions for 3 years [154]. Finally, some reports showed the use of *Bevacizumab* (an antibody against soluble VEGFα) in the treatment of retinal, cervical cord and multifocal HBs, resulting in modest therapy responses with disease progression after prolonged treatment [155–157]. In conclusion, and unfortunately, these therapeutic studies have had modest results at best and did not support any larger clinical trial so far.

One innovative idea to abolish HIF signaling in CNS HBs would be to target the HIF2α protein itself, instead of a single downstream target. Furthermore, the identification and characterization of additional driver mutations in CNS HBs would be helpful for the understanding of HB biology and the design of new therapeutic strategies. Targeting secondary

driver mutations is already successfully implemented for metastatic ccRCC [150] and it might be a good strategy for the treatment of CNS HBs.

1.9. Animal Models of VHL disease

Currently, there is no mouse model that faithfully recapitulates CNS Hemangioblastomas or the VHL disease. The *VHL* knockout (KO) mouse is embryonically lethal between embryonic day E10.5-E12 [158]. Although the embryos have clear vascular abnormalities, they do not develop CNS tumors or ccRCC. The conditional *VHL* KO mouse in the renal proximal tubule and hepatocytes (using the Lox-VHL-Lox system with PEPCK-Cre) develops kidney cysts and polycythemia, but does not form HBs or ccRCCs [159]. In addition, the conditional *VHL* KO in the liver (using the Lox-*VHL*-Lox system with Albumin-Cre) produces vascular hepatic lesions (cavernous hemangiomas) and increased steatosis, but does not develop HBs [160]. A subsequent mouse model was developed with conditional *VHL* KO under the control of β-actin promoter, in order to mimic the human disease and achieve a mosaic inactivation of *VHL* in multiple organs [161]. These mice developed multiple hepatic hemangiomas, abnormal angiogenesis in multiple organs and defects in spermatogenesis; but, surprisingly, they did not develop CNS HBs or ccRCCs, which may indicate that additional oncogenic drivers are necessary for the formation of these tumors. Finally, to the best of our knowledge, there are no reports of a conditional *VHL* KO mouse that targets the CNS, which might be due to the lack of scientific knowledge regarding the cell of origin of CNS HBs.

The only animal model that seems to recapitulate some of the biology of CNS HBs and VHL disease *in vivo* is the *vhl*$^{-/-}$ zebrafish mutant [162,163]. Although these embryos do not form

CNS tumors - most likely because they only survive until day 12 to 13 post-fertilization - they develop a hypervascularization in the brain and retina that mimics HB formation. In addition, the *vhl*$^{-/-}$ zebrafish mutants exhibit an abnormal expansion of their embryonic caudal hematopoietic tissue with an increased number of precursor red blood cells, which mimics the blood island formation and hematopoietic abnormalities seen in VHL patients [162,163]. Finally, they seem to represent a faithful model of early ccRCC development with abnormal growth of epithelial cells in their kidney proximal tubule [164]. So far, the *vhl*$^{-/-}$ zebrafish embryo is considered the most faithful animal model to study the biology of CNS HBs and potential therapeutic strategies in VHL disease.

1.10. Scientific Challenge

There is an urgent need to understand the biology of CNS HBs. Scientific research has been intensely developed for VHL-associated ccRCC tumors, which resulted in a dramatic improvement in the outcome of VHL patients. Unfortunately, no major scientific advance has been made in the recent years in the field of VHL-associated or sporadic CNS HBs; and today, those are the tumors that represent the major challenge and threat to VHL patients. There is a lack of cell lines and animal models that recapitulate this disease. Likewise, most of the signaling pathways that control HB development and evolution are unknown, as well as, the cell of origin of these brain tumors. The only treatment option is surgery, and this is not a permanent response to this lifelong disease. This doctoral thesis aims to contribute to the scientific field of CNS HBs by i) expanding the understanding of HB biology, ii) testing potential lead compounds to treat the disease and iii) creating scientific resources to study this intriguing tumor type.

CHAPTER 2

Materials and Methods

2.1. Methodologies of Chapter 3- *Whole-exome sequencing identifies therapeutic targets in CNS Hemangioblastomas*

Collection of CNS Hemangioblastoma samples

Eighteen VHL patients were identified in the VHL Clinic at Massachusetts General Hospital (Clinical Director, Dr. Othon Iliopoulos). Formalin-fixed Paraffin embedded (FFPE) Hemangioblastoma samples from diagnosed VHL patients were collected from the Neuropathology Brain Tumor bank at the Massachusetts General Hospital, in Boston US. All the patients have been previously diagnosed based on the presence of a germline mutation in the *VHL* gene. Eight tumor FFPE samples and correspondent peripheral blood were collected as part of the Discovery cohort and used for whole-exome sequencing analysis. The study was approved by the Institutional Review Board (IRB) and all the patients provided informed consent. Additional ten FFPE tumor samples were collected for the validation cohort.

DNA extraction for whole-exome sequencing and targeted-DNA libraries

FFPE HB tumor blocks were cut into 7µm slices and collected for DNA extraction. The QIAamp DNA FFPE extraction kit (from Qiagen) was used to remove the paraffin and to extract purified DNA. Briefly, tissue specimens were scraped into a 2mL tube and deparaffinized using CitriSolv solution. The supernatant containing paraffin was discarded and the tissue pellets were washed with ethanol and dried at 56˚C. The dried samples were incubated with 180µL of buffer ATL and 20µL of Proteinase K at 56˚C, on a 500 rpm shaker, until the tissue was completely digested. Samples were then incubated at 90˚C for 1 hour. After a quick spin, 4µL RNase A was added to the samples. The tissue was then incubated at room temperature for 2 minutes, then 200µL of buffer AL was added, and the samples were vortexed and briefly centrifuged. Finally,

the samples were washed with 200µL of 100% ethanol, vortexed and briefly centrifuged. Samples were then transferred onto QIAamp MinElute spin columns and centrifuged for 1 minute at 8000 rpm. The flow through was then discarded. Samples were washed with 500µL buffer AW1, centrifuged for 1 minute at 8000 rpm, then washed with 500µL buffer AW2 and centrifuged for 1 minute at 8000 rpm. Flow through was discarded. Sample tubes were centrifuged at maximum speed for 3 minutes to dry out the membrane of the QIAamp MinElute spin columns. Purified DNA was eluted with 20µL of buffer ATE and then quantified using the fluorescence-based PicoGreen assay (Molecular Probes Quant-IT broad range dsDNA kit, Life Technologies, #Q33120).

Whole blood samples were collected from each VHL patient and used as germline control for the whole-exome sequencing experiment. DNA was extracted via the Chemagic MSM I with the Chemagic DNA Blood Kit-96 (Perkin Elmer). This kit combines a chemical and mechanical lysis with magnetic bead-based purification. Whole blood samples were incubated at 37°C for 5-10 minutes to thaw. The blood was then transferred to a deep well plate with protease and placed on the Chemagic MSM I. The following steps were automated on the MSM I machine. M-PVA Magnetic Beads were added to the blood with protease solution, then the lysis buffer was added and the final solution was vortexed. The bead-bound DNA was then removed from solution using a 96-rod magnetic head and washed three times with Ethanol-based wash buffers, and once with water wash buffer. Finally, the DNA was eluted from the beads with the elution buffer and the purified DNA was quantified using the fluorescence-based PicoGreen assay (Molecular Probes Quant-IT broad range dsDNA kit, Life Technologies, #Q33120).

Whole-exome sequencing library construction

Whole-exome sequencing libraries from whole blood DNA and tumor DNA were constructed based on the Automated Solution hybrid Selection with specific exome enrichment protocol adapted for next generation sequencing at the Broad Institute [165]. The automated process was performed using the automated Bravo liquid holding station (Agilent Automation Solutions, #5400A). Briefly, purified DNA from whole blood or tumor samples (genomic DNA input, 10-100ng) was randomly fragmented using the Covaris adaptive focused acoustics instrument (Covaris, Inc., #E210), achieving a mean fragment length of 150 bp. The fragment size distribution should be between 75 and 300 bp for each sample and it was confirmed using the Caliper GX system with the HT DNA 1K LabChip (Caliper LifeSciences, #122000, #760517). After shreading, a clean-up step was performed with 150 µl of SPRI AMPure XP beads (Beckman Coulter Genomics, #A63881) in 20% polyethylene glycol (PEG) and 2.5 M NaCl buffer. This step also allowed the fragment size selection of the shredded DNA. After mixing the SPRI beads with the DNA, the samples incubated at room temperature for 2 minutes and were placed in a magnet to remove the supernatant. The beads were then washed twice with 100µL 70% ethanol. After the last wash, the beads dried at room temperature for 6 minutes. After this procedure, the DNA SPRI beads remained in solution (in-bead protocol) to avoid DNA fragment loss and to purify the DNA after each reaction. The following enzymatic reactions were then performed using the correspondent kits from New England Biolabs: end repair (New England Biolabs, #M0201B-96, M0203B-96), A-base addition (New England Biolabs, #M0212B-96) and adaptor ligation reaction (New England Biolabs, #M2200B-96). Between the enzymatic reactions, a SPRI clean-up step was performed as described before. After the final adaptor ligation reaction, an optimization PCR was performed in 40µl of eluted DNA with Illumina F&R

PE Enrichment Primers (Illumina, Inc., #1002290) in order to select the fragments containing both adaptors. PCR reaction was performed as follows: 120s at 95°C, 6 cycles (30s at 95°C, 30s at 65°C, 60s at 72°C).

The whole-exome selection was then performed using the Agilent Sure-Select Human All Exon Kit v2 (Agilent Technologies, #G3360-90000), which is based on the hybridization of the DNA fragment pools and specific exome RNA baits. The DNA fragment pools (25-60ng/µl) were hybridized with the biotinylated exome RNA baits for 5 minutes at 95°C, followed by 72 hours at 65°C. After the hybridization reaction, the double-strand molecules were captured using M280 Streptavidin Dynabeads (Life Technologies, #112-05D). Finally, the exome-specific DNA fragments were removed from the exome RNA baits by an "off-bead catch" PCR performed with Illumina PE enrichment primers (Illumina, Inc., #1002290). The PCR reaction was performed as follows: 120s at 95°C, 20 cycles (30s at 95°C, 30s at 65°C, 60s at 72°C), and then 10 minutes at 72°C. The final PCR products were purified with SPRI Ampure beads as described above and represent the final library for sequencing. The concentration of the final library (greater than 5ng/µl) was determined using the KAPA Library Quantification Kit (KAPA Biosystems, #KK4832). All the other DNA quantification steps throughout the protocol were performed using PicoGreen fluorescence using Molecular Probes Quant-IT broad range dsDNA kit (Life Technologies, #Q33120).

Finally, all the libraries were normalized to 2nM, pooled together and denatured with 0.1M NaOH. Each pool of whole-exome libraries was run on paired 76bp runs, with an 8 base index sequencing read. The individual libraries were pooled considering the number of lanes needed to meet 300x of depth coverage for all libraries. The pooled libraries were sequenced on a HiSeq 2500 sequencer (Illumina, Inc.).

Targeted-DNA sequencing library construction

To confirm the identified mutations through targeted sequencing, we amplified the targeted regions from extracted tumor DNA using the following gene-specific forward and reverse primers, respectively:

5'-TTGGACGTGTGGTCTGTGTT-3' and 5'-CTCCGTCTCTTCCTCCACAG-3' for *TRAF2*; *5'*-CTCTATGTTTGCGGGGATGT-3' and 5'-TGGTCCAGGATGTGCAGTAA-3' for *NOS2*; 5'-TCCATTTGTTGCCACTGAAA-3' and 5'-TTTGGATTGCACTTTCCCTT-3' for *ASH1L*; 5'-AGAAGATGAGCAGCATTCTGAAG-3' and 5'-GGGCTTATTTAGGTTTTTGTGCT-3' for *TET1*; 5'-GAGTGAGTGACAACGTACCCTTC-3' and 5'-GCCTTTTATTTCCGTTAACCATC-3' for *PNPLA3*.

Targeted libraries were then prepared from the amplified PCR products using the NEBNext Ultra DNA Library Prep Kit (New England Biolabs, #E7370S). Briefly, 1µg of amplified targeted DNA was mixed with End Repair Reaction Buffer and Enzyme Mix to correct potential fragmented regions. The Illumina adaptors were then ligated to the PCR products. The final products were then purified using AMPure XP beads (Beckman Coulter) with a size selection of 300-400bp fragments. A final PCR step was performed with NEBNext Q5 Hot Start HiFi to add the indexes i7 and i5 and barcode the samples (New England Biolabs, #E7335). The final libraries were once again purified with AMPure XP beads (Beckman Coulter) and run in the Bioanalyzer (Agilent) for quality control purposes. The final targeted-DNA libraries were run in a MiSeq sequencer (Illumina, Inc.) with a 300-bp paired-end sequencing kit (Illumina, Inc., #MS-102-2002).

Data analysis

All the sequencing data were processed by a computational biology team collaborating in the project. After sequencing, the raw sequencing data were processed in terms of read alignment, sequencing quality control and sample contamination estimation with the standard Broad Institute Picard pipeline v3. One tumor and one normal (blood) sample were sequenced for each patient in order to identify somatic DNA changes. A target sequencing coverage of 300x was chosen for the tumor samples (150x for normal samples) to ensure discovery of somatic mutations with low allelic fraction, given that hemangioblastoma tumors are known to be heterogeneous and with relatively low tumor cell fraction.

The sequencing data were further processed using Broad Institute's Firehose data analysis system to remove sequencing artifacts and to subsequently detect mutated genes and copy-number variations. To increase data quality, we applied several filters: 1) filters that identify and remove DNA changes likely caused by sample preparation (FFPE, OxoG and OxoQ filters); 2) realignment filter to remove sequencing reads incorrectly mapped due to homologous genomic regions; 3) exclusion of DNA changes frequently observed in a standard panel of approximately 5000 normal (blood) samples, likely caused by sequencing errors. We then used the processed whole-exome sequencing data to identify copy-number variations, DNA base substitutions and insertions/deletions using Allelic CapSeg (read capture-based segmentation), MuTect [166] and IndeLocator, respectively. We used GISTIC 2.0 [167,168] and MutSig [135] to find significant copy number changes and significantly mutated genes, respectively.

The normalized mRNA levels of *PHD3* and *PNPLA3* from 72 pairs of ccRCC tumors and respective normal kidney control were generated by the TCGA Research Network and collected from http://cancergenome.nih.gov/.

Vectors and cloning

The pCMV6 vector containing the full-length human PNPLA3 cDNA sequence upstream of myc and FLAG tags (PNPLA3-myc-DDK) was purchased from Origene (#RC209577). The identified nonsense mutation PNPLA3 Y191* was produced by PCR mutagenesis by two fragments that included the specific mutation using the following forward and reverse primers, respectively, flanked with SalI and MluI restriction sites:

Fragment 1: 5'-CGCGTCGACCCGCGATCGCCATGTACGACGCAGAGCGC-3' and 5'-GGCAGATGTCCTACTCCCCA-3'; Fragment 2: 5'-TGGGGAGTAGGACATCTGCC-3' and 5'- GCGACGCGTCAGACTCTTCTCTAGTGAAAAACTGG -3'. Both fragments were then joined by PCR with the following forward and reverse primers, respectively: 5'-CTCGCGTCGACCCGC-3' and 5'-GCGACGCGTCAGACTCTTC-3'. The final mutated PCR product was cut with SalI and MluI enzymes and sub-cloned into the pCMV6 vector. The vector sequence was confirmed by Sanger sequencing.

The short hairpin RNA sequences targeting the coding region of the human *PNPLA3* were obtained from the MPL (Molecular Profiling Laboratory) at the Center for Cancer Research at the Massachusetts General Hospital. To specifically target the PNPLA3 coding sequence, the pLKO lentiviral vectors harbored the following sequences: shRNA#1 (GATATGCCTTCGAGGATATTT) and shRNA #2 (GTGTCTGACTTTCGGTCCAAA).

The full-length human cDNA sequence of *VHL* was previously sub-cloned into the retroviral vector pBABE hygro, originating the vectors VHL and pBABE empty control [49].

Cell transfections and infections

The cultured cells were maintained at 37ºC in a humidified incubator with 5% CO_2 and grown with Dulbecco's Modified Eagle's Medium (regular DMEM, Thermo Fisher Scientific, #11995040) with 10% fetal bovine serum (FBS) and 1% PenStrep Glutamine (Invitrogen). U2OS cells were transiently transfected with pCMV6 PNPLA3-myc-ddk wild-type, pCMV6 PNPLA3 Y191* or empty vector control, with the transfection reagent PolyJet (SignaGen Laboratories). Eight hours after transfection, the cell culture medium was changed to regular DMEM with 10% FBS. The transfected cells were used for subsequent experiments 36 hours after transfection.

The ccRCC parental cell line 786-O was used as a $VHL^{-/-}$ cell line and 293T cells were used to grow retrovirus and lentivirus. For retrovirus production, we used Lipofectamine 2000 (Invitrogen) to transfect 293T cells with the Amphopac vector, the VSVG vector and the DNA vector of interest, in this case, VHL or pBABE puro. We collected the virus-containing media 36 hours after the transfection and centrifuged at 1200rpm for 5 minutes. We collected the supernatant and then added Polybrene to a final concentration of 4µg/mL. The virus-containing media were then filtered and diluted 1:1 with regular DMEM. 786-O target cells were incubated with the final diluted media and centrifuged for 45 minutes at 4000rpm. After selection with 2µM puromycin in regular DMEM, the pBABE and VHL isogenic pairs were used for subsequent analysis.

For lentivirus production, we used Lipofectamine 2000 (Invitrogen) to transfect 293T cells with the RSV-REV vector, the lentivirus VSVG vector, the RER and the DNA vector of interest, in this case, pLKO containing shRNA anti-GFP, shRNA anti-PNPLA3 hairpin #1 or shRNA anti-PNPLA3 hairpin #2. The lentivirus were collected and processed as previously

described. The 786-O cells were then infected with the different lentiviruses, selected with 2µM puromycin in regular DMEM 10% FBS and used in further experiments.

Protein extracts and Immunoprecipitation

Total cellular protein was extracted from cultured cells with RIPA buffer (50mM Tris, pH 8, 150mM NaCl, 1% NP-40, 0.5% DOC, 0.01% SDS and 0.02% NaAzide) and protease inhibitors (trypsin inhibitor 20µg/mL, leupeptin 10µg/mL, sodium vanadate 0.2mM, pepstatin A 5µg/mL, aprotinin 10µg/mL, NaFI 0.1M and PMSF 100µg/mL). For immunoprecipitation experiments we used EBC buffer (50mM Tris pH8, 120mM NaCl and 1% NP-40) with the protease inhibitors previously described. Protein extracts were then quantified using Bradford. To prepare samples for western-blotting, 60 µg of protein per sample were diluted in 3x sample buffer (187.5mM Tris pH 6.8, 6% SDS, 35% Glycerol and 0.01% BPB) and incubated at 95ºC for 5 minutes. For immunoprecipitation of PNPLA3-myc-ddk protein, 1µg of protein extract per sample was incubated with anti-ddk FLAG M2 beads (Sigma-Aldrich, #A2220) for 3 hours at 4ºC. The immunoprecipitate extracts were washed five times with NET-N buffer (100mM NaCl, 20mM Tris-HCl pH8, 1mM EDTA and 0.5% NP-40) and eluted with 1.5x loading buffer (93.8mM Tris pH 6.8, 3% SDS, 17.5% Glycerol and 0.005% BPB) at 95ºC for 5 min.

Western-Blotting

Protein extracts were resolved in SDS-PAGE gels with 7.5% or 12% acrylamide. The proteins were then transferred to a PVDF membrane (BioRad), blocked with blocking buffer (10mM Tris, pH 8, 150mM NaCl, 0.5% Tween, 4% BSA, 0.02% Sodium Azide) for 1 hour at 4ºC rocking and incubated overnight rocking at 4ºC with the following antibodies in blocking

buffer: 1:1000 anti-PNPLA3 rabbit polyclonal (Sigma-Aldrich, #AV48936), 1:250 anti-HIF2α rabbit polyclonal (D9E3) (Cell Signaling Technologies, #7096), 1:250 anti-HIF1α rabbit monoclonal (D2U3T) (Cell Signaling Technologies, #14179), 1:100 anti-VHL IG32 mouse monoclonal (obtained from Kaelin lab at Harvard Medical School) [55], 1:2000 anti-HA tag mouse monoclonal (6E2) (Cell Signaling Technologies, #2367) and 1:10000 anti-pan actin ab-5 mouse monoclonal (Neo-markers, #MS-1295-B). Membranes were then washed three times with TBST (10mM Tris, pH 8, 150mM NaCl, 0.5% Tween) for 15 min rocking at RT and incubated with ECL Mouse IgG, HRP-linked whole antibody (GE Healthcare Lifesciences, #NA931-1ML) or ECL Rabbit IgG, HRP-linked whole antibody (GE Healthcare Lifesciences, #NA934-1ML) at a concentration of 1:10000 in TBST, for 1 hour rocking at RT. The membranes were washed again three times for 15 min rocking at RT with TBST. Finally, the protein bands were developed with the ECL western blotting substrate (Thermo Fisher Scientific, #32106) and the chemiluminescence was measured in a ChemiDoc Imaging system (BioRad).

Lipid droplet staining and confocal microscopy

Cultured cells were plated on top of glass coverslips within 6-well plates the day before the staining. In the next day, 400μM of oleic acid conjugated with BSA (Sigma-Aldrich, #O3008-5ML) was added to the cell medium (DMEM, 10% FBS) and incubated for 5 hours. The cells were fixed to the glass coverslips with 1.5% glutaraldehyde for 5 minutes and washed twice with PBS. The Nile Red stock solution (Sigma-Aldrich #72485-100MG, 0.1mg/mL in acetone) was diluted 1:100 in PBS and added to the cells for 30 minutes at room temperature (protected from light). The cells were then washed twice with PBS and the coverslips were mounted in slides with Vectashield Mounting Medium with DAPI (Vector Laboratories, #H-1200). Stained slides were imaged on a Zeiss LSM 700 confocal microscope using a 63x oil objective. Z-stack

images were acquired (n=3 per sample) and maximum intensity projections were processed using Image J. The total Nile Red staining per image was quantified using Image J as mean grey value and normalized to the number of nuclei.

Immunohistochemistry

Formalin-fixed parafin embeded (FFPE) blocks of VHL-associated HB tumors were collected from the Neuropathology Department at Massachusetts General Hospital. Normal liver and normal cerebellum blocks were collected from the same department. The tissue blocks were cut in 7µm slices and deparaffinized in xylene for 10 minutes. After hydration, with sequential washes in 100% ethanol, 0.5% H_2O_2 in MeOH, 90% ethanol and 70% ethanol, the slides were rinsed three times with PBS. Sodium citrate (1M) was used as antigen retrieval for 30 minutes at 95ºC. After cooling down to room temperature, the slides were rinsed with PBS three times. The slides were then blocked for 30 minutes at room temperature with 1:250 BGAR (biotinylated goat anti-rabbit IgG antibody) (Vector, #BA-1000) diluted in 1% BSA in PBS, and incubated overnight at 4ºC with 1:50 anti-PNPLA3 rabbit polyclonal antibody (Sigma Aldrich, #AV48936). In the next day, the slides were rinsed with PBS three times, incubated with 1:250 BGAR (Vector, #BA-1000) for 30 minutes at room temperature, and rinsed again with PBS. Vectastain ABC HRP solution (Vector, #PK-6100) was then added to the slides and incubated for 30 minutes at room temperature. After a final washing step with PBS, the staining was developed for 5 minutes with DAB Peroxidase (HRP) substrate (Vector, # SK-4100). The slides were then washed with ddH_2O, stained with hematoxylin, dehydrated to xylene and coverslip with permount.

Quantitative Real-Time Polymerase Chain Reaction

RNA was harvested from 786-O cells infected with shRNA GFP, shRNA PNPLA3 #1 or shRNA PNPLA3 #2 using the RNAeasy Mini Kit (Qiagen). Purified RNA was treated with RNA-free gDNA wipeout to remove genomic DNA and cDNA was synthesized using the Quantitect Reverse Kit (Qiagen). PCR was performed using Fast SYBR Green Master Mix (AB Applied Biosystems) and run on a 7500 Fast Real-Time PCR System machine (AB Applied Biosystems). The following intron-spanning forward and reverse primers, respectively, were used:

5'-CCGGTTCTCAGGGACAGTG-3' and 5'-CTCGCTCTGACTCCAAAAGG-3' for *28S*; 5'- GCTTCCTGGGCTTCTACCAC-3' and 5'- AGATGCCAATGTTCCGACTC-3' for *PNPLA3*; 5'- ATCAGCTTCCTCCTGTCCCT-3' and 5'- GGGCTGCACTTCGTGTGGGT-3' for *EGLN3*; 5'-CCAGTGACACAGGATGACCTTC-3' and 5'-GCTTGAGGTAGAAGCTCATCTGG -3' for *NOS2*; 5'- CTTGGCATCTGTATTGTGGT -3' and 5'- GGGTGGCCATGGTCCCAAGG -3' for *CA12*; 5'- CTCATCCTCGTGGTCATCCT-3' and 5'- CCTTCAAACTCGCTCTCTGG-3' for *EPOR*.

HIF2α palmitoylation assay

293A cells were transfected with HA-HIF2A pcDNA 3.1 (with constitutively active form of HIF2α P405A/P531A) or pcDNA3.1 empty vector control, using the transfection jetPRIME reagent (Polyplus transfection). After 24 hours, the cells were treated overnight with 50μM of palmitate probe (16C-YA) or DMSO in regular DMEM, 10% dialyzed FBS. The cells were then washed in PBS (without Ca^{2+} and Mg^{2+}) and harvested using protein lysis buffer (50mM TEA-HCl pH 7.4, 150mM NaCl, 1% Triton X-100, 0.2% SDS, 1x Protease inhibitor-EDTA free (Roche)). Protein quantification was performed using the Bradford Assay (BioRad, # 500-0006).

For the click chemistry reaction, 1.5mg of cell lysates were reacted with 50µL of freshly premixed click chemistry solution (100uM Biotin-azide; 1mM TCEP: Tris(2-carboxyethyl) phosphine hydrochloride; 100uM TBTA: Tris[(1-benzyl-1*H*-1,2,3-triazol-4-yl)methyl]amide and 1mM $CuSO_4$) for 1 hour at room temperature. After the click chemistry reaction, the protein samples were immunoprecipitated with anti-streptavidin beads (Thermo Scientific, #15942-050) for 1 hour at room temperature. Protein samples were finally eluted with 3x loading buffer (95% Formamide and 10mM EDTA) and incubated at 95ºC for 5min before loading into the gel. As input control we loaded ten percent of the total protein extract. The 786-O cells were treated with palmitate probe (16C-YA) or DMSO and processed, as described above, to detect endogenous HIF2α palmitoylation.

Growth curves

786-O cells infected with shRNA GFP, shRNA PNPLA3 #1 or shRNA PNPLA3 #2 were counted and plated in triplicate into 24-well plates at a confluency of 12.000 cells per well, in Dulbecco's Modified Eagle's Medium (Thermo Fisher Scientific , #11995040) with 10% FBS. At day 1, the medium was changed to Dulbecco's Modified Eagle's Medium Base (Sigma Aldrich, #D5030) with 10% dialyzed FBS, 10mM glucose and different glutamine concentrations: 2mM, 0.9mM or 0.6mM). At day 5, cells were fixed with 2% glutaraldehyde for 10 minutes at RT. The cells were then washed twice with ddH_2O and stained with crystal violet solution (0.1% crystal violet powder in water) for 30 minutes at RT. After staining, the plates were washed again twice with ddH_2O and dried overnight at RT. To develop the staining, 10% acetic acid was added per well and the plates were incubated rocking at RT for 30 minutes. The

crystal violet absorbance was measured at 590nm in a black 96 well plate. The number of cells per sample in Day 1 was quantified in parallel and used to normalize the final number of cells.

Statistics

Statistical analysis was performed for all the experiments. Unpaired, two-tailed *t* test was used for all the analysis. Differences between two groups were considered significant when the *p* value was less than 0.05 ($p<0.05$).

2.2. Methodologies of Chapter 4 – *Inhibition of HIF2α is a therapeutic strategy for treatment of VHL disease*

Zebrafish strains

Zebrafish (*Danio rerio*) embryos were grown in the dark at 28.5ºC in Tübingen E3 HEPES buffer. Animal experiments were conducted based on standard fish husbandry protocols according to U.S. national guidelines. *Vhl*^{hu2117} fish were kindly provided by Dr. Fredericus van Eeden from Utrecht, Netherlands. *Vhl*$^{-/-}$ embryos were obtained as needed from breeding pairs of *Vhl*$^{hu2117+/-}$ adult fish and their genotype was confirmed by PCR using the following forward and reverse primers, respectively, that span the mutation site, 5'-CGTTGAAGCTTTAGTCTAACTCGG-3' and 5'-CGAACCCACAAAAGTTGTTATTCT-3'.

Zebrafish *HIF1αb* (ENSDARG00000034293) and *epas1b* (ENSDARG00000057671) mutants were generated using engineered transcription activator-like effector nucleases (TALENs) as previously described [169]. The *HIF1αb* mutant allele contains a 4-bp deletion in intron 1, causing a disruption of its splice donor site. The *epas1b* mutant allele contains a 10-bp deletion in exon 3, resulting in a frameshift mutation that will affect 754 out of the total 834 amino acids (***Figure S5***).

Tg (GFP:Fli1) breeding pairs were kindly provided by Dr. David Laugenau (MGH Cancer Center, Boston, MA). Heterozygous *Vhl*$^{hu2117+/-}$ mutants were crossed with the transgenic line Tg (GFP:Fli1) in order to obtain Tg (GFP:Fli1;*vhl*$^{+/-}$) and Tg (GFP:Fli1;*vhl*$^{-/-}$) embryos. *Vhl*$^{-/-}$ embryos and siblings (*wt* and *vhl*$^{+/-}$ embryos) were divided at 3dpf according to phenotypic differences. Treatments with HIF2α inhibitor compound 76 or 0.01% DMSO (in E3 buffer) to assess the expression of Hif-target genes were started in 3dpf embryos. Treatment with

dimethyloxaloylglycine (DMOG) at 100µM was performed in 5dpf *wt* embryos for 48 hours, unless described otherwise.

Morpholinos

The *HIF1αa*, *HIF1αb*, *epas1a* and *epas1b* morpholinos were designed to specifically block the translation of the specific mRNAs. The following sequences were used: *hif1αa* morpholino (TTTTCCCAGGTGCGACTGCCTCCAT), *hif1αb* morpholino (CAGTGACAACTCCAGTATC CATTCC), *epas1a* morpholino (ATGATGCTGAAGAACCTTGTCCTGC), *epas1b* morpholino (TCATCGCGCCGTTCTCGCGTAATTC).

To test the activity and specificity of the morpholinos, the pTol2 vector was engineered to contain the different morpholino target sequences upstream of EGFP cDNA: HIF1αa-ATGMO-EGFP, HIF1αb-ATGMO-EGFP, Epas1a-ATGMO-EGFP and Epas1b-ATGMO-EGFP. RNA was synthetized in vitro from each vector using the mMESSAGE mMACHINE T3 kit (Ambion). Single-cell stage *wt* embryos were injected with 150ng/µL of RNA and 0.2mM of the correspondent morpholino or scrambled morpholino control. At 24hpf, the embryos were imaged for EGFP signal on an Olympus MVX10 microscope using a 6.3X objective.

To test the contribution of the different Hif paralogs to the hypoxia response in zebrafish, HIF1α*a* and *HIF1αb* morpholinos in combination, *epas1a* and *epas1b* morpholinos in combination or the control morpholino were injected (at 0.2mM) into single-cell stage *wt* embryos. The total number of normal, developmentally abnormal or dead embryos was counted 24 hours after injections. At 3dpf, injected *wt* embryos were treated with 100µM DMOG for 24 hours and their total RNA was then extracted for qRTPCR analysis.

Quantitative Real-Time Polymerase Chain Reaction

RNA was harvested from zebrafish embryos, at the indicated developmental stage, using the RNAeasy Mini Kit (Qiagen). Purified RNA was treated with RNA-free gDNA wipeout to remove genomic DNA and cDNA was synthesized using the Quantitect Reverse Kit (Qiagen). PCR was performed using Fast SYBR Green Master Mix (AB Applied Biosystems) and run on a 7500 Fast Real-Time PCR System machine (AB Applied Biosystems). The following intron-spanning forward and reverse primers, respectively, were used:

5'-TCGCTAGTTGGCATCGTTTATG-3' and 5'-CGGAGGTTCGAAGACGATCA-3' for *18S*; 5'-CCTGGAAATGGAGCTGGATA-3' and 5'-CCGGTCAAATAAAGGCTCAA-3' for *phd3*; 5'-TGTTGGTGGAAATTCAGCAG-3' and 5'-CACCCTGATGACGAAGAGGT-3' for *vegfab*; 5'-GCATCAGACAAGTGCTGCG-3' and 5'-AGACAGGTGCATTGGCGAG-3' for *epo*; 5'-GCCTTGTTCAAACCCTACCA-3' and 5'-TGGAGAAGAATGTCGCCTCT-3' for *epas1a*; 5'-CTCATCATCTTCCCCTTCCA-3' and 5'- GCCACCGAGTGACTTCAGAT-3' for *epas1b*; 5'-AGCGTCACCTCTAACCTGGA-3' and 5'-AAAAGAAACCCGTCCAGAGC-3' for *HIF1αa*; 5'-CCTGGACAAAGCCTCCATTA-3' and 5'-CCATCCTCAGACAGGACCAT-3' for *HIF1αb*; 5'-AAATGGGCACCAGTCTTCTG-3' and 5'-ATTGGTGGACAGCGAGTTCT-3' for angiopoietin 1 (*angpt1*); 5'-TTGCAACCACGACAACAACT-3' and 5'-AACGACATGTGCCATGAAAA-3' for *tgfa*; 5'- TTACATGGGAGGG TCCTAATGAG-3' and 5'-GGACACAACTGCTCGAGAAGAA-3'for transferrin (*tfa*).

Zebrafish 5'-UTR vectors and in vitro experiments

The pTol2 vector was engineered to contain the 5'-UTR of each of the zebrafish genes *HIF1αa*, *HIF1αb*, *epas1a* and *epas1b*, upstream of the Luciferase ORF: pTol2-HIF1αa 5'-UTR-

Luc, pTol2-HIF1αb 5'-UTR-Luc, pTol2-epas1a 5'-UTR-Luc, pTol2-epas1b 5'-UTR-Luc and pTol2-Luc control. U2OS cells (human bone osteosarcoma cell line) were stably transfected with pTol2-Luc, pTol2-HIF1αa 5'UTR-Luc, pTol2-HIF1αb 5'UTR-Luc, pTol2-epas1a 5'UTR-Luc or pTol2-epas1b 5'UTR-Luc. U2OS transfected cells were treated for 30 hours with 5μM of compound 76 or vehicle control (DMSO). The total protein was extracted and the luciferase activity was measured using the Dual-Glo Luciferase Kit (Promega). The luciferase activity was normalized to total protein levels and the normalized signal from compound 76-treated cells was normalized to DMSO-treated cells. Experiments were performed in biological triplicates.

O-dianisidine staining

Embryos were incubated in a 12-well plate with O-dianisidine solution (O-dianisidine from Sigma-Aldrich in 100% ethanol with 0.1M sodium acetate and 30% H_2O_2 in ddH_2O) for one hour. The embryos were then washed with ddH_2O and fixed with 4% paraformaldehyde in PBS overnight at 4ºC. A bleaching solution (0.8% KOH, 0.9% H_2O_2, 0.1% Tween in ddH_2O) was added to the embryos for 30 minutes to remove their natural pigmentation. After another fixation step with 4% paraformaldehyde overnight, embryos were immersed in 30% glycerol solution in a depression slide and imaged on an Olympus MVX10 microscope with 6.3X objective. At least 8 embryos were stained and analyzed for each experimental condition. Experiments were performed in biological triplicates.

Computer-assisted quantification of image intensity

Ilastik [170], an open-source interactive learning and segmentation toolkit was used to train classifiers to recognize stained pixels in the images. The Ilastik version 0.5 was used in this study. The open-source CellProfiler software [171] was then applied in order to determine the

likelihood of a pixel being stained, using the Ilastik classifiers, and to estimate the total number of stained pixels in each image by summing these likelihoods. The Ilastik classifier and the CellProfiler pipeline are provided at CellProfiler website (http://www.cellprofiler.org/published_pipelines.shtml).

In situ hybridization

Whole-mount *in situ* hybridization was performed as previously described [162]. Anti-sense digoxygenin-labeled probe for *c-myb* was obtained as previously described [172]. 5dpf treated animals were fixed in 4% paraformaldehyde in PBS overnight at 4ºC. Embryos were washed with PBS/0.2% Tween-20 (PBST) and incubated with bleaching solution (0.8% KOH, 0.9% H_2O_2, 0.1% Tween in ddH_2O) to remove natural pigmentation. After a second wash step with PBST, embryos were permeabilized with Proteinase K at 10µg/mL during 60 minutes at 28.5ºC. Embryos were then fixed with 4% formaldehyde/0.2% glutaraldehyde in PBS for 20 minutes at room temperature. After pre-hybridization in Hyb^+ solution for at least 2 hours at 65ºC, embryos were then hybridized with 500µL of anti-sense mRNA probe (1ng/µL) in Hyb^+ solution (50% Formamide, 5x SSC, 0.1% Tween, 9mM citric acid, 0.5mg/mL yeast torula RNA, 0.1mg/mL heparin, pH6) at 65ºC overnight. After several washes with Hyb^- solution (Hyb^+ without yeast torula RNA and heparin) at 65ºC, embryos were incubated with blocking solution (0.1M maleic acid, 150nM NaCl, 0.2% Tween, 2mg/mL BSA, 5% sheep serum, pH 7.5) for 2.5 hours at room temperature. The embryos were then incubated overnight at 4ºC with alkaline phosphatase conjugated anti-Dig antibody (Roche, product number: 11093274910) in blocking solution, to recognize digoxygenin residues. The substrates NBT/BCIP (Roche) were incubated with the embryos until the staining was developed. Embryos were imaged on an Olympus MVX10

microscope with 6.3X objective and divided into normal *cmyb* staining *vs.* highly expanded staining in the CHT. Between 20 and 30 embryos were analyzed in each group, and the experiment was performed in biological duplicate.

Collection of blood smears and May-Grunwald/Giemsa staining

Treated *vhl*$^{-/-}$ embryos and siblings were anesthetized with 0.4% tricaine. At least 20 embryos of each group were moved to a solution containing 0.033% heparin, 1% BSA, 0.006% tricaine in PBS. The tail was cut off in a region posterior to the cloaca with a razor blade. The red blood cells were collected and stored at 4ºC. The cells were spun down into a Superfrost Plus microscope slide (Fisherbrand) using a cytospin machine. The cells were dried at room temperature overnight and fixed with 100% methanol. May-Grunwald/Giemsa staining was performed using a kit (American MasterTech). The slides were dried at room temperature overnight and imaged on an Olympus BX41 microscope with a 40X objective. Images were acquired with an Olympus DP72 camera. Undifferentiated and differentiated red blood cells were identified and counted according to their staining pattern and morphology. In each experiment, between 50 and 100 cells were counted per sample in quadruplicate.

Fluorescent and Confocal Microscopy

Tg (GFP:Fli1)(*vhl*$^{+/-}$ or *vhl*$^{+/+}$) and Tg (GFP:Fli1)(*vhl*$^{-/-}$) treated embryos were anesthetized with 0.4% tricaine. Embryos were immobilized in 1% low melting point agarose and mounted. Confocal images were taken on a Zeiss LSM 700 microscope using 10X objective. Maximum intensity projections were obtained by running multiple Z-stack slides and 3D reconstructions were made using the Zen 2009 software. Fluorescent images were acquired on an Olympus MVX10 microscope using a 6.3X objective. Using Image-J, a region of interest (ROI)

was selected in the caudal hematopoietic system (CHT) and used to calculate the mean intensity value for each image. Each experiment had 5 embryos per sample and was performed in triplicate.

Cardiac contractility

The method for quantification of cardiac contractility was previously described [173]. In brief, cardiac image analysis was performed using the Measurement Studio and IMAQ Vision software packages (National Instruments) with VisualStudio 6.0 (Microsoft). Sequential still frames were analyzed to identify ventricular end systole (ES) and end diastole (ED). The endocardial boundary was traced, and the area of the region defined by this trace was recorded. Five sequential cardiac cycles were recorded at a minimum. Fractional area change (FAC), an established parameter of ventricular performance, was calculated based on the formula: FAC = 100 x (EDA - ESA)/EDA, where EDA and ESA indicate ED and ES areas.

Statistics

Statistical analysis was performed for all the experiments. Unpaired, two-tailed *t* test was used for all the analysis except for the ventricle fractional shortening experiment in which first way ANOVA test was used. Differences between two groups were considered significant when the *p* value was less than 0.05 ($p<0.05$).

2.3. Methodologies of Chapter 5 – Establishment of Hemangioblastoma cell lines and an orthotopic mouse model

Establishment of Hemangioblastoma cell lines

The HB tumor specimen was collected directly from the operation room in the Neurosurgery Department at Massachusetts General Hospital. Upon tissue resection, the sample was immediately stored in ACL4 10% FBS on ice (Thermo Fisher Scientific, #0890137DK). The sample was transported to the lab and centrifuged at 1200rpm for 5 minutes in a 50mL falcon tube. The pelleted tissue was placed in a p100 plate and covered with 1-2mL of ACL4 0% FBS. With two sterile scalpels, the tumor specimen was cut into small pieces that were collected into a 15mL falcon tube. ACL4 0% FBS medium was added to the falcon (5mL) and the sample was centrifuged at 1200rpm for 5 minutes. The red blood cells were removed from the tumor specimen by adding 5mL of RBCs lysis buffer (diluted 1:10 in sterile H_2O, Biolegend, #420301) for 10 minutes at RT in the dark. The sample was then centrifuged at 1200rpm for 5 minutes and the supernatant discarded. ACL4 0% FBS with 50µL of Liberase (2.5mg/mL, Sigma-Aldrich #5401054001) was added to the tumor sample to promote tumor cell dissociation. The sample was incubated for 1 hour at 37ºC with manual agitation every 15 minutes. After 1 hour of incubation, 500µL of FBS was added to the sample to inactivate the liberase. The sample was then centrifuged at 1200rpm for 5 minutes, washed with 5mL of ACL4 10% FBS and centrifuged again at 1200rpm for 5 minutes. Finally, the pelleted cells were resuspended in 5mL of ACL4 10% FBS and plated in 100mm culture plates. The cells grown using the Schlegel method were plated in 60mm culture plates with a monolayer of irradiated feeder cells (normal foreskin fibroblasts) and cultured with 10 µg/mL of ROCK inhibitor (Enzo Life Sciences, #Y-27632) in TCM medium (3:1 (v/v) F-12 Nutrient Mixture (Ham)/Dulbecco's modified Eagle's medium (Invitrogen), 5% fetal bovine serum, 0.4 µg/mL hydrocortisone (Sigma-Aldrich),

5µg/mL insulin (Sigma-Aldrich), 8.4 ng/mL cholera toxin (Sigma-Aldrich), 10ng/mL epidermal growth factor (Invitrogen) and 24 µg/mL adenine (Sigma-Aldrich)) [174,175]. The cells were maintained at 37ºC in a humidified incubator with 5% CO_2 and fresh media was added once or twice a week.

Cell lines

The ccRCC cell lines 786-O and UMRC2, the osteosarcoma cell line U2OS, the human umbilical vascular endothelial cells (HUVEC) and the foreskin human fibroblasts (feeders) were maintained at 37ºC in a humidified incubator with 5% CO_2. 786-O, UMRC2, U2OS and feeder cells were cultured in Dulbecco's Modified Eagle's Medium (regular DMEM, Thermo Fisher Scientific, #11995040) with 10% fetal bovine serum (FBS) and 1% PenStrep Glutamine (Invitrogen). HUVEC cells were grown in 0.1% gelatin-coated plates with EBM medium + EGM supplements (Lonza, #CC-3121, #4133).

The full-length human cDNA sequence of *VHL* was previously sub-cloned into the retroviral vector pBABE hygro, originating the vectors VHL and pBABE empty control [49]. The ccRCC parental cell lines 786-O and UMRC2 were used as $VHL^{-/-}$ cell lines and 293T cells were used to grow retrovirus. For retrovirus production, we used Lipofectamine 2000 (Invitrogen) to transfect 293T cells with the Amphopac vector, the VSVG vector and the DNA vector of interest, in this case, VHL or pBABE puro. We collected the virus-containing media 36 hours after the transfection and centrifuged at 1200rpm for 5 minutes. We collected the supernatant and then added Polybrene to a final concentration of 4µg/mL. The virus-containing media were then filtered and diluted 1:1 with regular DMEM 10% FBS. 786-O cells or UMRC2 target cells were incubated with the final diluted media and centrifuged for 45 minutes at 4000rpm. After

selection with 2μM puromycin in regular DMEM, the pBABE and VHL isogenic pairs were used for subsequent analysis.

Protein extracts

Total cellular protein was extracted from cultured cells with RIPA buffer (50mM Tris, pH 8, 150mM NaCl, 1% NP-40, 0.5% DOC, 0.01% SDS and 0.02% NaAzide) and protease inhibitors (trypsin inhibitor 20μg/mL, leupeptin 10μg/mL, sodium vanadate 0.2mM, pepstatin A 5μg/mL, aprotinin 10μg/mL, NaFI 0.1M and PMSF 100μg/mL). Protein extracts were then quantified using Bradford. For western-blotting, 60 μg of protein per sample were diluted in 3x sample buffer (187.5mM Tris pH 6.8, 6% SDS, 35% Glycerol and 0.01% BPB) and incubated at 95ºC for 5 minutes.

Western-Blotting

Protein extracts were resolved in SDS-PAGE gels with 7.5% or 12% acrylamide. The proteins were then transferred to a PVDF membrane (BioRad), blocked with blocking buffer (10mM Tris, pH 8, 150mM NaCl, 0.5% Tween, 4% BSA, 0.02% Sodium Azide) for 1 hour at 4ºC rocking and incubated overnight rocking at 4ºC with the following antibodies in blocking buffer: 1:250 anti-HIF2α rabbit polyclonal (D9E3) (Cell Signaling Technologies, #7096), 1:250 anti-HIF1α rabbit monoclonal (D2U3T) (Cell Signaling Technologies, #14179), 1:100 anti-VHL IG32 mouse monoclonal (obtained from Kaelin lab at Harvard Medical School) [55] and 1:10000 anti-pan actin ab-5 mouse monoclonal (Neo-markers, #MS-1295-B). Membranes were then washed three times with TBST (10mM Tris, pH 8, 150mM NaCl, 0.5% Tween) for 15 minutes rocking at RT and incubated with ECL Mouse IgG, HRP-linked whole antibody (GE Healthcare Lifesciences, #NA931-1ML) or ECL Rabbit IgG, HRP-linked whole antibody (GE Healthcare

Lifesciences, #NA934-1ML) at a concentration of 1:10000 in TBST, for 1 hour rocking at RT. The membranes were washed again three times for 15 minutes rocking at RT with TBST. Finally, the protein bands were developed with the ECL western blotting substrate (Thermo Fisher Scientific, #32106) and the chemiluminescence was measured in a ChemiDoc Imaging system (BioRad).

Quantitative Real-Time Polymerase Chain Reaction

RNA was harvested from irradiated fibroblasts (feeders), 786-O, AM1 ACL4 and AM2 ACL4 using the RNAeasy Mini Kit (Qiagen). Purified RNA was treated with RNA-free gDNA wipeout to remove genomic DNA and cDNA was synthesized using the Quantitect Reverse Kit (Qiagen). PCR was performed using Fast SYBR Green Master Mix (AB Applied Biosystems) and run on a 7500 Fast Real-Time PCR System machine (AB Applied Biosystems). The following intron-spanning forward and reverse primers, respectively, were used:

5'-CCGGTTCTCAGGGACAGTG-3' and 5'-CTCGCTCTGACTCCAAAAGG-3' for *28S*; 5'-AGTCCAACATCACCATGCAG-3' and 5'-TTCCCTTTCCTCGAACTGATTT-3' for *VEGFA*.

Fluorescence-activated cell sorting (FACS)

AM1 ACL4, AM2 ACL4, U2OS and HUVEC cells were grown in culture in the conditions previously described. Eighty percent confluent adherent cells were washed with sterile cold PBS, trypsinized with 1.5mL Trypsin-EDTA (0.25%) (ThermoFisher Scientific, #25200056) for 5 minutes at 37ºC and centrifuged at 1200 rpm for 5 minutes. The pelleted cells were then washed in 5mL of sterile PBS with 10mM glucose and centrifuged at 1200 rpm for 5

minutes. The supernatant was discarded and the cell pellet resuspended in 100µL of sterile PBS with 10mM glucose. The cells were blocked with Fc Receptor blocking (Biolegend, #422301) at 1:30 dilution and incubated on ice for 10min. The cells were then centrifuged at 1200rpm for 5 minutes. The cell pellet was resuspended in 100µL of sterile PBS with 10mM glucose and the following antibodies were added separately into the solution: PE-PDPN (Biolegend, #337003), APC-CD31 (Biolegend, #303105), PE_Cy7-VEGFR2 (Biolegend, #359911), APC-VECadherin (Biolegend, #138011), APC_Cy7-CD11b (Biolegend, #301341), APC-CD133 (Biolegend, #141207), APC-CXCR4 (Biolegend, #306509) and APC-CD45 (Biolegend, #304011). The antibodies were incubated with the cells for 30 minutes at 4ºC protected from light. The cell solutions were then washed with 5mL of PBS with 10mM glucose and centrifuged at 1200rpm for 5 minutes. The supernatant was discarded and the cell pellet was resuspended in 300µL of PBS with 10mM glucose and filtered through the 35µm filtered FACS tubes (BD Biosciences, #352235). Cell surface markers were analyzed using a SORP 5 Laser BD FACSAria Fusion Cell Sorter, BSL2+ (BD Biosciences). A minimum of 5.000 cells were analyzed per experiment and each experiment was performed in biological triplicate.

Mice models

All the animal experiments were performed at the Instituto de Investigaciones Biomedicas 'Alberto Sols' in Madrid and were approved by the internal ethical committee and by the Spanish and European Community guidelines. The animals were maintained in a controlled room with a 12 hours cycle of light and *ad libitum* access to water and food. Eight weeks-old NOD/SCID mice were orthotopically injected in the brain with *AM1 ACL4* (n=7 mice) or *AM2 ACL4* cells (n=8 mice). Briefly, the animals were anaesthetized using an induction box with 3-4% isofluorane in pure oxygen, and then placed on a stereotaxic device to inject

100.000 cells into the right caudate nucleus [176]. Anesthesia was maintained during the surgery with a flow of 1-1.5% isofluorane in oxygen. Prior to the surgery, and during 3 days after, the mice received intraperitoneally the analgesic drug buprenofine (0.1mg/Kg). Tumor development was followed by Magnetic Resonance Imaging up to a maximum limit size, at which moment the mice were sacrificed (usually up to 20 days). The brain tumors and normal brain parenchyma were then resected, fixed in formalin and embedded in paraffin for histological analysis.

Magnetic Resonance Imaging and Spectroscopy

The Magnetic Resonance experiments were performed *in vivo* on a Bruker Biospect system (Bruker Medical GmbH®, Ettlingen, Germany) with a 7.0 Tesla horizontal superconducting magnet. The ParaVision 5.1 software (Bruker Medical Gmbh) was used to acquire all the data. The animals were maintained throughout the studies in a heated probe at 37ºC and anesthetized with 1.5% isofluorane in O_2. In order to follow tumor initiation, anatomical images T2-weighted (T2W) spin-echo images were acquired for each animal on a weekly basis (using a RARE sequence – Rapid Acquisition with Relaxation Enhancement – with repetition time TR of 3.000 ms, echo time TE of 60 ms, averages of 3 and RARE factor of 8). Once a brain tumor was detected, T2W images were performed every 2-3 days to measure tumor development. Tumor volume was calculated for every study based on the serial T2W axial images, with a thickness of 1.5mm per slice. The tumor volume was determined using Image J by measuring the tumor area per slice. Once the tumor reached a maximum limit size, contrast-enhanced T1-weighted (CE-T1W) spin-echo images were acquired (with repetition time TR of 300 ms, echo time TE of 10 ms and averages of 3), after intravenous injection with the contrast

agent Gd(III)-DTPA (Gd-diethylene triamine pentaacetic acid, Magnevist®, Bayer) at 0.3 mmol/Kg.

The diffusion studies were acquired with a StejskalTanner sequence (with four shots echo-planar readout gradient, TR of 3.000 ms, TE of 40 ms, average of 1, acquisition matrix of 128×128 with an in-plane resolution of 273 × 273 μm^2, diffusion gradient separation (Δ) = 10 ms, diffusion gradient duration (δ) = 3 ms) and b factors of 0, 60, 200 and 500 s/mm^2 applied in three orthogonal directions corresponding to a gradient strength of 30, 50 and 80%. MR images were computed to generate ADC maps and ADC values were obtained using the following equation: $\boldsymbol{S_b = S_0\ exp\ (-ADC\ x\ b)}$, where S_b is the signal intensity at any *b* value and S_0 is the intensity with the diffusion gradient switched off.

In vivo spectroscopy was performed within a region of interested (ROI) within the tumor area or normal brain parenchyma. Once selected the 27mm^3 voxel, a PRESS spectrum (Point-Resolved Spacial Spectroscopy) was acquired within the region (with TR of 3.000 ms, TE of 35 ms and 128 scans). The ^{1}H MRS spectra were processed with LCModel [177]. The peaks of methylene groups (-CH_2-) were detected at approximately 1.3ppm and the correspondent areas were quantified to determine the intracellular lipid content. The peak areas were normalized to the internal control creatinine and phosphocreatine peaks (lipid ratio= lip1.3ppm/Cr+PCr).

H&E staining

The formalin-fixed paraffin embedded (FFPE) blocks containing the brain tumors and the normal brain parenchyma were cut into 7µm slices and stained with hematoxylin and eosin (H&E) as described [178]. FFPE blocks from human CNS Hemangioblastoma tumors were collected for comparison purposes from the Neuropathology Department at Massachusetts General Hospital. After staining, the slides were dried at room temperature overnight and imaged

on an Olympus BX41 microscope with 20X and 40X objectives. Images were acquired with an Olympus DP72 camera.

Statistics

Statistical analysis was performed for all the experiments. Unpaired, two-tailed *t* test was used for all the analysis. Differences between two groups were considered significant when the *p* value was less than 0.05 ($p<0.05$).

CHAPTER 3

Whole-exome sequencing identifies therapeutic targets in CNS Hemangioblastomas

The *Chapter 3 o*f this doctoral thesis is based on the research work:

Metelo AM et al. (2016) Loss of PNPLA3/Adiponutrin is a recurrent molecular event in VHL-associated CNS Hemangioblastomas. In preparation.

3.1. Scientific Background

Hemangioblastomas (HBs) are tumors of the Central Nervous System (CNS) that can develop sporadically or as a clinical manifestation of the familial cancer syndrome - VHL disease [1]. HBs are benign tumors from the cerebellum, spinal cord, brainstem, retina and hypothalamus formed by tumor cells (called *stromal* cells), endothelial cells and perycites [1,10]. Despite their benign behaviour, these lesions significantly compromise the life of HB patients and often lead to blindness, ataxia, and death. Currently, HBs represent the main cause of morbidity and mortality among VHL patients [53]. And so far the only treatment option is surgical resection, which can be complicated by the presence of multifocal lesions and their specific location in the CNS.

The genomic landscape of CNS Hemangioblastomas is underexplored. Most of the HB tumors arise in association with the familial VHL disease, in which patients harbor a germline mutation in the *VHL* tumor suppressor gene. VHL patients develop multiple synchronous or sequential HBs throughout their life, as well as clear cell Renal Cell Carcinomas (ccRCCs), adrenal gland pheochromocytomas, pancreatic neuroendocrine tumors, and cystadenomas in the pancreas and in the middle ear. The current hypothesis for HB development is based on the inactivation of the second *VHL* allele in addition to the germline mutation in *VHL*. Indeed, several studies showed loss-of-heterozigosity (LOH) of the chromosomic region 3p25 in HB tumor cells, which is the genomic location of *VHL* [19,179]. However, other copy number variation events were also detected in a subset of Hemangioblastomas, such as gain of chromosome 1 and chromosome 4, loss of chromosome 6, 9 and 22q13 [16,180]. Unfortunately, most of these studies do not distinguish between sporadic and familial HBs, and the molecular functions of these additional genomic alterations and their impact on HB development are not known.

VHL is an E3-ubiquitin ligase that in normoxia conditions targets Hypoxia-Inducible Factors (HIFs) for proteosomal degradation. Tumors with inactivation of the VHL protein have estabilized HIF expression and consequent activation of the HIF downstream target genes involved in angiogenesis, erythropoiesis, metabolic reprogramming and metastasis [52,77]. Lipid metabolism is a major target of HIF signaling, which represses β-oxidation and lipogenesis and stimulates lipid storage enzymes such as perilipin 2 [90,92,94]. These metabolic changes in $VHL^{-/-}$ cells lead to the abnormal accumulation of tryglycerides in the form of cytoplasmatic lipid droplets, which results in the "*clear cell*" phenotype characteristic of HB *stromal* cells and other VHL-related tumors [91,92]. Interestingly, while HBs display an obvious HIF-dependent phenotype with strong upregulation of VEGFα, EPO and PDGFβ, they respond poorly to anti-angiogenic inhibitors when compared to ccRCC tumors [152,155]. This clinical evidence suggests that additional oncogenic pathways are involved in the development of CNS HBs.

Recent genome-wide sequencing studies have characterized the complex genomic landscape of ccRCC tumors [130]. The *VHL* tumor suppressor gene is inactivated in more than 90% of sporadic renal cell carcinomas and it is significantly mutated in other tumor types. *VHL* is not uniquely responsible for tumor development, and there are additional driver mutations that significantly contribute to ccRCC tumor progression. Epigenetic remodelers and modifiers including BAP1, PBRM1 and SETD2 were found to be significantly mutated in ccRCC tumors, as well as genes involved in the PI3K-mTOR pathway, and the tumor suppressors PTEN and p53[130]. These studies clarified the idea that different oncogenic mutations can synerzige with loss of *VHL* and promote tumor development. Similarly, HBs might have additional genomic abnormalities that, in addition to loss of *VHL*, contribute to tumor growth on a manner that is dependent on the specific biology of VHL-associated brain tumors.

In this study, we performed whole-exome sequencing in a discovery cohort of VHL-associated Hemangioblastomas with the aim of identifying novel oncogenic drivers. We confirmed that somatic *VHL* inactivation occurs in all the tumor samples, in addition to the germline mutation, and it is restricted to a small fraction of the tumor sample. Interestingly, we found a case of tumor whole-exome duplication with consequent loss of all of the four *VHL* alleles, which shows that complete inactivation of *VHL* is indeed necessary for CNS HB formation. In adition, recurrent loss of chromosome 8 was detected in the analyzed tumor cohort. Moreover, and for the first time, we identified a nonsense inactivating mutation in the *PNPLA3* gene. PNPLA3 (or adiponutrin) is an acyl-transferase that belongs to the patatin-like phospholipase family of proteins [181]. Its function has been controversial over the years, but a recent study clarified its enzymatic activity as a lysophosphatidic acid acyl-transferase (LPAA) that incorporates long-chain fatty acids into newly synthetized triglycerides [182]. Here, we showed that PNPLA3 is downregulated in 83% of CNS VHL-related Hemangioblastomas. This specific downregulation is a characteristic of $VHL^{-/-}$ cells and also occurs in VHL-associated ccRCCs. Furthermore, we showed that a decrease in PNPLA3 levels leads to the oncogenic stimulation of HIF-target genes, possibly caused by HIF2α palmitoylation. Finally, we show that this downregulation of PNPLA3 significantly contributes to a selective growth advantage of $VHL^{-/-}$ cells under metabolic stress. This is the first report identifying a genomic alteration in a lipid metabolic enzyme in CNS HBs that synergizes with *VHL* loss to promote oncogenic signaling and cell growth.

3.2. Experimental Results

VHL-associated Hemangioblastomas are characterized by a small tumor fraction with a reactive tumor microenvironment.

In order to explore the mutational landscape of CNS VHL-associated HBs, we collected a discovery cohort of eight formalin-fixed paraffin embedded (FFPE) tumor samples from the Neuropathology Department at the Massachusetts General Hospital in Boston, US. All the eight tumors were resected from diagnosed VHL patients. ***Figure 6A*** depicts the clinical data from each tumor patient, four males and four females, with ages ranging from 17 to 63 years-old. Seven of these tumors were resected from the cerebellum and one tumor was collected from the spine. Considering the categorization of HBs based on the presence of intratumoral hematopoiesis, we evaluated each collected tumor and included tumors with (3 out of 8) and without (3 out of 8) a clearly defined hematopoietic component.

To identify the oncogenic drivers that promote HB formation, we created DNA libraries enriched for the exomes of individual tumors and compared to those of the respective germline blood, as controls. In order to capture low frequency mutations in these highly heterogeneous tumors, an average coverage of 200 reads per gene was achieved. Using the ABSOLUTE algorithm, we calculated the tumor purity of each tumor sample (***Figure 6B***), which represents the fraction of tumor cells, as determined by the somatic mutational events. The median tumor fraction for VHL-associated HBs was 0.23 ± 0.08 among the eight samples, which means that almost 80% of the tumor is formed by reactive (normal) cells of the microenvironment (mainly endothelial cells, pericytes and in some cases, hematopoietic cells). The only exception was the sample XTB1, which exhibited a surprisingly high tumor fraction value (0.84), suggesting that

the presence of additional driver mutations may confer a highly proliferative capacity to the specific tumor cells.

A

Discovery group

HB Patients	Gender	Age	Tumor location	Hematopoiesis
XT3012	Male	38	Cerebellum	Yes
XT3082	Female	63	Cerebellum	No
XT5104	Male	17	Spine	Yes
XT5752	Male	31	Cerebellum	No
XT6479	Male	39	Cerebellum	-
XT6956	Female	43	Cerebellum	No
XT6956	Female	47	Cerebellum	Yes
XT7193	Female	34	Cerebellum	-

B

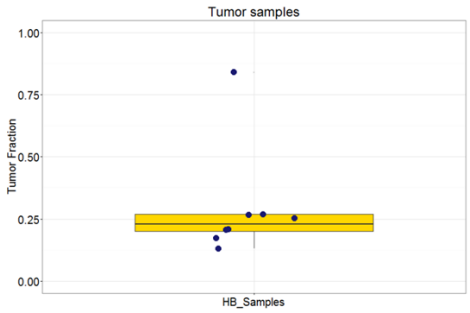

C

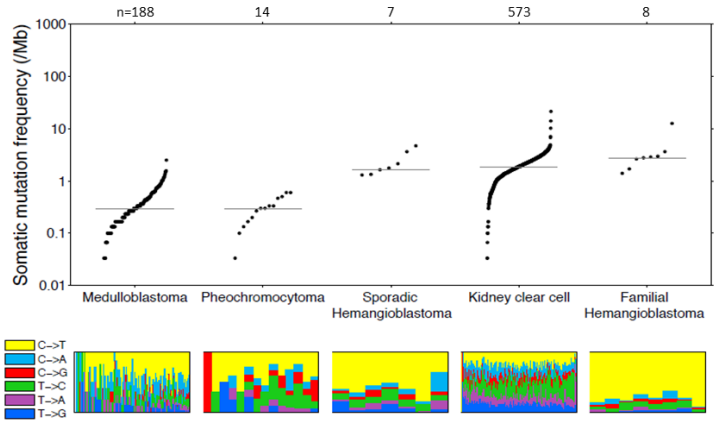

Figure 6 - VHL-associated Hemangioblastomas are characterized by a small tumor fraction and a reactive microenvironment. (A) Clinical details of eight VHL-associated Hemangioblastomas selected to integrate the discovery group. The gender, age, tumor location and presence of hematopoietic compartment are described for each patient. **(B)** Percentage of tumor cells (tumor fraction) in each tumor sample based on copy-number variation events and somatic point mutations, calculated using ABSOLUTE. **(C)** Somatic mutation frequency of non-synonymous mutations (per Mb) in VHL-associated Hemangioblastomas (familial HBs), VHL-associated Clear Cell Renal Cell Carcinomas (ccRCC) and VHL-associated Pheochromocytomas. The cerebellar tumors Sporadic Hemangioblastomas and Medulloblastomas were also included for comparison purposes. The specific mutation types present in the different tumors are described for each sample.

The mutational landscape of a specific tumor can be assessed by determining the mutation frequency across the tumor exome. This parameter varies dramatically among tumor types and individual patients [135]. Our discovery cohort of VHL-associated HBs had an average mutation frequency of 2.3 mutations per megabase (Mb), which is similar to the other VHL-associated ccRCCs (2.2 mutations/Mb) but significantly higher than VHL-associated Pheochromocytomas (1.3 mutations/Mb) (***Figure 6C***). Interestingly, sporadic HBs and familial VHL-associated HBs have a similar mutation frequency, both significantly higher than medulloblastoma, a pediatric cerebellar tumor. In addition, the majority of the non-synonymous mutations found in VHL-associated HBs are C to T transitions (***Figure 6C***). This mutational profile is distinct from the other VHL-associated tumors (ccRCCs and Pheochromocytomas) that harbor a significant percentage of other substitutions; mainly T to C transitions.

Loss of chromosome 3 and chromosome 8 are recurrent copy-number variation events in VHL-associated Hemangioblastomas.

In order to identify copy number variation (CNV) events for each HB tumor we compared the allelic copy number profile of tumor samples with the respective blood normal control using the GISTIC 2.0. ***Figure 7*** summarizes the CNV events across the different samples, with color coding ranging from chromosomal deletion in blue and amplification in red. The intensity of the color coding varies proportionally with the tumor fraction.

The main CNV event detected in the HB discovery cohort was loss of chromosome 3 or 3p that occurred in 6 out of 8 samples (in the tumor samples XT3012, XT5104, XT5752, XT6479, XT7193 and XTB1). The genomic location of the *VHL* tumor suppressor gene is chromosome 3p25, which confirms the inactivation of the second *VHL* allele in the majority of

the HB samples. In addition, loss of chromosome 8 was detected for the first time in two out of eight HBs (XT6479 and XTB1) and gain of chromosome 1q was detected in the sample XTB1.

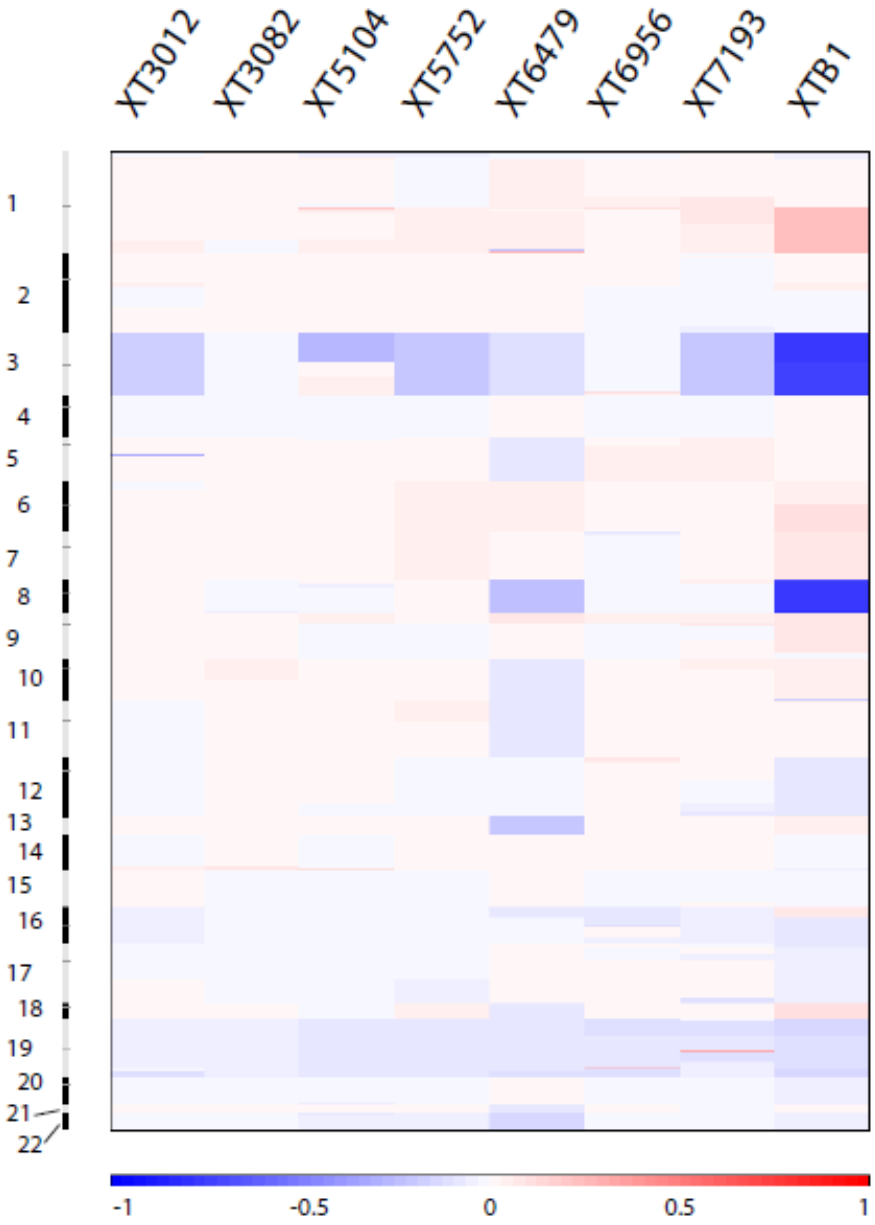

Figure 7 - Loss of chromosome 3 and chromosome 8 are recurrent copy-number variation events in VHL-associated Hemangioblastomas. Copy number variation analysis in eight Hemangioblastoma tumors across the 22 different chromosomes using GISTIC 2.0. The copy number variation events were normalized to the respective germline blood control and are shown as amplification (in red) or deletion (in blue).

Inactivation of the tumor suppressor gene *VHL* occurs through LOH and somatic point mutations.

We confirmed that all the eight patients harbor a germline mutation in one *VHL* allele, which is a common feature of VHL patients and confirms the VHL disease diagnosis. Single-nucleotide point mutations (p.S65W and p.C162F), frameshift mutations (p.P103fs, p.Q132fs), small point deletions (p.F76del) and splicing sites mutations (rs10146636 and rs5030814) were identified in the *VHL* germline of HB patients (***Figure 8A***). All these VHL-inactivating mutations are known to be present in VHL families and inactivate the VHL protein function.

In order to identify the acquired somatic mutations in HB tumors, we detected and ranked the mutated genes (using MuTect and MutSig, respectively) based on: a) conservation of the mutated amino acid among species, b) clustering of mutations among different tumor samples and c) background mutation frequency for the specific gene [135]. According to these requirements, the gene found to be significantly mutated among the HB tumors was *VHL*, with two independent samples showing the same N78S mutated residue (samples XT6479 and XT6956, p= 2.9E-05).

With these data, we identified two different mechanisms for complete *VHL* inactivation in CNS HBs (***Figure 8A***): loss-of-heterozygosity (with loss of chromosome 3/3p) and somatic point mutations in the *VHL* gene. Six out of eight HB samples showed loss of chromosome 3/3p in the tumor, indicating that LOH is the main mechanism of *VHL* inactivation in familial HBs. Sample XT6956 did not show somatic deletion of chromosome 3, but instead had a somatic point mutation in the second *VHL* allele (p.N78S). Sample XT3082 had a low sequencing coverage (LC) that compromised the CNV analysis.

A

HB patients	XT3012	XT3082	XT5104	XT5752	XT6479	XT6956	XT7193	XTB1
Germline Mutations in VHL	p.S65W	p.F76del	rs10146636	p.P103fs	p.C162F	rs5030814	p.Q132fs	p.S65W
Somatic Mutations in VHL					p.N78S	p.N78S		
Somatic Chromosome Loss	3	LC	3p	3	3	-	3	3

B

Tumor specific whole-exome duplication

XT6479	VHL inactivation mechanism
Allele 1	Germline mutation p.C162F
Allele 2	Loss of chromosome 3
Allele 3	Loss of chromosome 3
Allele 4	Somatic mutation p.N78S

Figure 8 - Inactivation of the *VHL* tumor suppressor gene occurs through LOH and somatic point mutations. **(A)** Description of all mutations and copy number variation events that affect the *VHL* gene in the HB samples from the discovery cohort. Germline mutations and somatic point mutations in *VHL* were identified in the germline blood control and in the tumor samples respectively, using Mutect. *VHL* is the only gene significantly mutated in the discovery cohort according to MutSig (p=2.9E-05). Somatic loss of chromosome 3 or 3p was analyzed for each tumor using GISTIC 2.0. **(B)** Whole-exome duplication was identified in the tumor sample XT6479 compared to the respective germline control. The specific mechanisms of *VHL* inactivation in each of the four tumor alleles are described.

Interestingly, the tumor sample XT6479 underwent whole-exome duplication during tumor evolution, which is a genomic phenomenon that occurs in 37% of human tumors [183]. As described in ***Figure 8B***, the tumor cells of XT6479 had a total of four different *VHL* alleles and, remarkably, all of them were inactivated through distinct genetic mechanisms: one germline point mutation (p.C162F), one somatic point mutation (p.N78S) and two allelic deletions of

chromosome 3. This specific case highlights the critical role of *VHL* in HB development and confirms that complete inactivation of *VHL* is necessary for CNS HB formation.

Somatic point mutations in NOS2 and PNPLA3 were identified and confirmed in familial Hemangioblastoma tumors.

Despite the fact that *VHL* was the only gene found significantly mutated in the discovery cohort, we decided to investigate and manually check additional genes that might contribute to HB formation. Using the IgV software, we examined the top100 mutated genes and focused our analysis in cancer-related genes and genes located in chromosome 1q, 3p, 4, 8 and 22q. These genomic locations are specifically relevant for our study as they represent the main CNV events reported in CNS HBs [16,180]. We identified five genes that passed our bioinformatics cutoffs: *TRAF2*, *NOS2*, *ASH1L*, *TET1* and *PNPLA3*. All these mutations had: a) a minimum of 100 reads spanning the mutation region; b) absence of additional mismatched bases in the specific read compared to the standard human exome sequence; c) several reads showing the exact same mutation; d) the same mutation in both the positive and negative strands. Importantly, by employing targeted next-generation sequencing, we confirmed the missense mutation in *NOS2* (sample XT6956, p.E1108G) and the nonsense mutation in *PNPLA3* (sample XTB1, p.Y191*). No other mutation or focal CNV event was found for these specific genes (*PNPLA3* and *NOS2*) in the other HB samples of the discovery cohort. The mutations detected by whole-exome sequencing in the genes *ASH1L*, *TET1* and *TRAF2* were not confirmed by targeted sequencing, indicating that they were false positives.

Newly identified nonsense mutation in the PNPLA3 gene inactivates the acyl-transferase function of the protein.

HB tumor cells have a characteristic "clear cell" phenotype with a large cytoplasm rich in lipid droplet vesicles [91]. In this context, we decided to further explore the mutation detected in the *PNPLA3* gene, which codes for a lysophosphatidic acid acyl-transferase required for the synthesis of triglycerides. Interestingly, the genomic location of this gene (chromosome 22q13) has been previously reported as lost in a subset of CNS HBs [180].

The identified nonsense mutation in *PNPLA3* (p.Y191*) harbors a single nucleotide change (TAC → TAG) coding for a premature stop codon that leads to the truncation of the protein (***Figure 9A and 9B***). In order to characterize the function of this mutation, we overexpressed the wild-type (WT) or the mutated (Y191*) protein in U2OS cells. The C-terminus of the WT protein is detected by IP/WB while the nonsense mutation Y191* leads to a truncated and unstable protein that lacks the PNPLA3 C-terminus (***Figure 9C***).

To test whether the identified *PNPLA3* mutation disrupts its activity as an acyl-transferase (that incorporates free fatty acids for triglyceride synthesis), we overexpressed PNPLA3 WT, PNPLA3 Y191* or the empty vector control in U2OS cells, and assayed the lipid droplet accumulation after incubation with oleic acid. Nile red staining was used as a common marker of neutral lipids, and DAPI as the nuclear staining [184,185]. Representative confocal images of U2OS cells expressing the different proteins are shown in ***Figure 9D***. Compared to the empty vector control, the overexpression of the PNPLA3 WT protein leads to a two-fold increase in the Nile Red staining (p=0.012), while the overexpression of the mutant form Y191* does not (***Figure 9E***). These data confirm that the PNPLA3 WT protein is functional *in vitro* and

promotes triglyceride accumulation in the presence of oleic acid, whereas the nonsense p.Y191* mutation leads to loss of the acyl-transferase activity of the PNPLA3 protein.

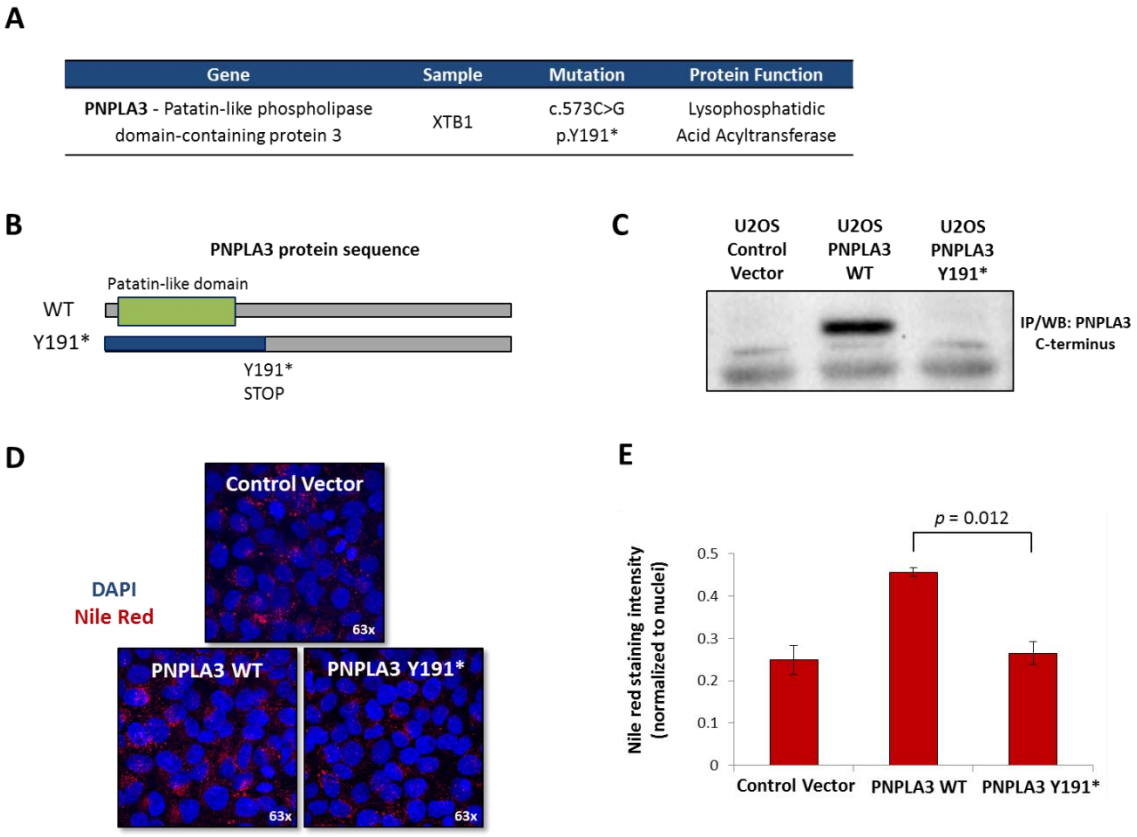

Figure 9 - Newly identified nonsense mutation in the PNPLA3 gene inactivates the acyl-transferase function of the protein. (A) Description of the identified nonsense mutation in the *PNPLA3* gene (patatin-like phospholipase domain-containing protein 3) and recognized function of the protein. **(B)** Scheme describing the wild-type (WT) and the mutated Y191* versions of the PNPLA3 coding region. The putative patatin-lipase domain is highlighted in green. **(C)** Immunoprecipitation/Western blotting for the C-terminus region of PNPLA3. U2OS cells were stably transfected with empty vector control, PNPLA3-myc-ddk wild-type (WT) or PNPLA3 Y191* mutant. **(D)** Representative z-stacked confocal images of U2OS cells stably transfected with empty vector control, PNPLA3 wild-type (WT) or PNPLA3 Y191* mutant, after treatment with 400µM oleic acid for five hours. Nile Red stains lipids and is shown in red while the nuclei are stained with DAPI in blue. Image magnification is 63x. **(E)** Quantification of the Nile red staining normalized to the number of nuclei per image. Image J was used for the analysis and three independent z-stacked images were used for each experiment. The experiments were performed in biological triplicates. Data represent mean ± SEM. p=0.012, unpaired, 2-tailed t test.

The majority of VHL-associated HB tumors do not express PNPLA3.

The nonsense mutation found in *PNPLA3* was only detected in one out of eight HBs from the discovery cohort (sample XTB1). As previously described, no other somatic mutation or focal CNV was detected for *PNPLA3* in the other tumor samples. Nevertheless, the fact that the identified *PNPLA3* mutation resulted in protein inactivation (***Figure 9***) led us to hypothesize that downregulation of PNPLA3 may be required for the development of HBs, and different mechanisms – genetic, epigenetic and post-transcriptional programs – may lead to this outcome independently of the mutations in the *PNPLA3* gene. To test whether loss of PNPLA3 expression is detected in several HBs we employed immunohistochemistry and compared with normal cerebellum, which is the main location of CNS HBs. We used human liver as a positive control for PNPLA3 expression.

We found that PNPLA3 is expressed in specific cell types of the human normal cerebellum including dentate nucleus neurons (black arrows), endothelial cells (asterisks), pericytes, hematopoietic cells and some glial cells (***Image 10A***). Importantly, only one out of eight HBs from the discovery cohort expresses moderate levels of PNPLA3, all the other tumors being negative (***Image 10B***). To further corroborate our results, we collected an independent cohort of ten additional VHL-associated HBs. From this new cohort, eight out of ten VHL-associated HB tumors have weak or no expression of PNPLA3 (***Image 10C***). Overall, the combined cohorts show that 83% of VHL-associated HBs downregulate or lack expression of PNPLA3 (***Image 10D***). Interestingly, we detected the presence of rare hematopoietic cells with strong PNPLA3 expression in several HB specimens (***Image 10B***, black arrow), which may indicate the presence of normal macrophages and mast cells in the tumor samples.

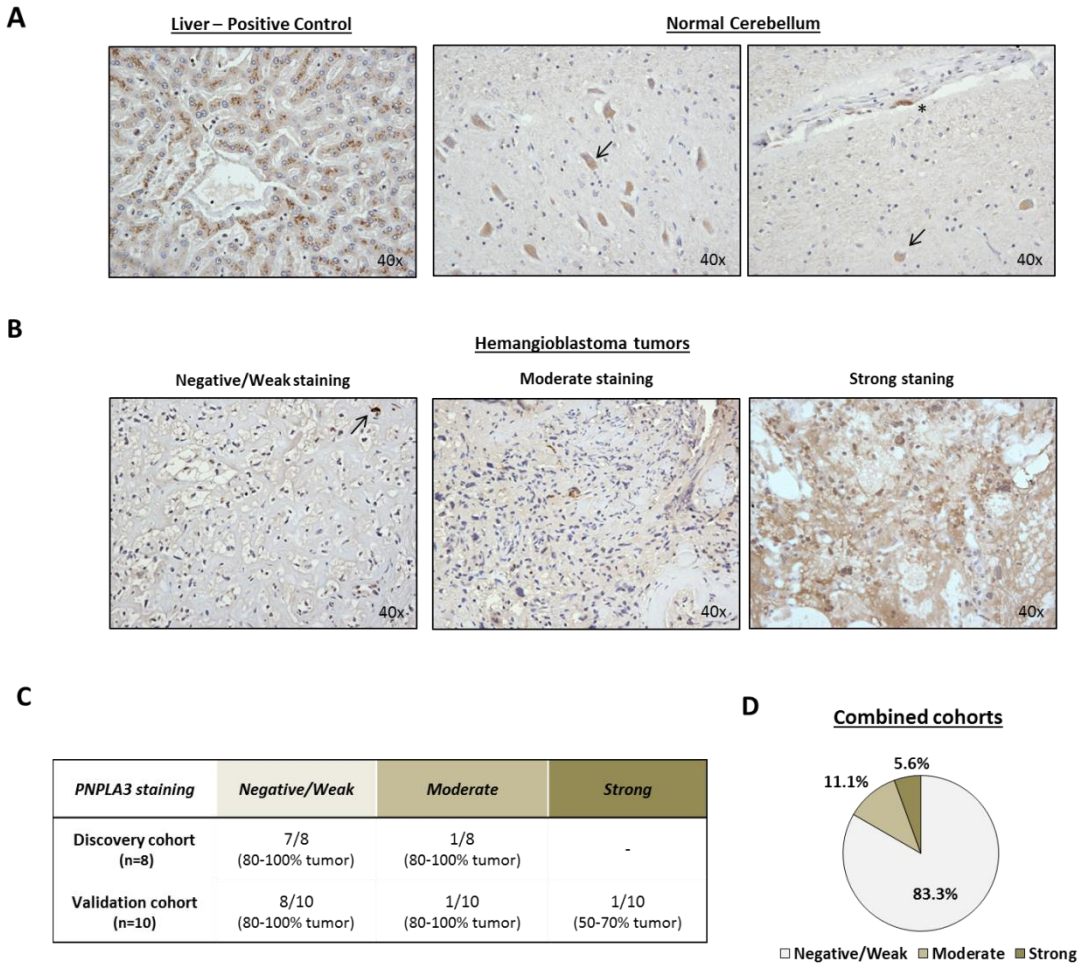

PNPLA3 staining	*Negative/Weak*	*Moderate*	*Strong*
Discovery cohort (n=8)	7/8 (80-100% tumor)	1/8 (80-100% tumor)	-
Validation cohort (n=10)	8/10 (80-100% tumor)	1/10 (80-100% tumor)	1/10 (50-70% tumor)

Figure 10 - PNPLA3 is frequently downregulated in VHL-associated Hemangioblastomas. (A) Immunohistochemistry images detecting PNPLA3 protein in formalin fixed paraffin-embedded (FFPE) slides of human liver (positive control) and adult normal cerebellum. PNPLA3 is expressed in different cells of the normal cerebellum: cerebellar dentate nucleus neurons (black arrow), endothelial cells and pericytes (asterisk), hematopoietic cells and some glial cells. Image magnification is 40x. **(B)** Immunohistochemistry images of PNPLA3 protein in CNS VHL-associated HBs. A range of PNPLA3 staining was detected across samples that were divided into three staining groups: Negative/Weak, Moderate and Strong. Representative images of the distinct staining groups are shown. Rare hematopoietic cells with strong PNPLA3 staining were detected in several tumors (black arrow). Image magnification is 40x. **C)** Evaluation of PNPLA3 expression in VHL-associated HBs in the discovery (n=8) and in the validation cohorts (n=10). **D)** Distribution of PNPLA3 expression across CNS VHL-associated HBs (combined cohorts, n=18).

Downregulation of PNPLA3 occurs in VHL-negative ccRCC tumors.

Lipid metabolism is altered in $VHL^{-/-}$ cells as a consequence of HIF activation. Also, accumulation of triglycerides in the form of lipid droplets and abnormal lipid metabolism are characteristics of not only HBs, but also clear cell Renal Cell Carcinoma (ccRCC) tumors.

Therefore we hypothesized that downregulation of PNPLA3 might be a common mechanism among $VHL^{-/-}$ tumors. To test this hypothesis, we collected transcriptional data from the TCGA database from 72 ccRCC patients. We compared the expression levels of the bona-fide HIF target gene *EGNL3* and the *PNPLA3* gene in ccRCC tumors and paired normal kidneys. As expected, our positive control the HIF-target gene *EGNL3* is significantly increased in the ccRCC tumors compared to normal samples (10624.9 ± 820.5 *vs.* 481.6 ± 111.7 *normalized reads, p<0.001*) (***Figure 11A***). Remarkably, PNPLA3 levels exhibited the opposite trend, being significantly decreased in ccRCC tumors compared to normal samples (12.6 ± 2.0 *vs.* 30.9 ± 8.9 *normalized reads, p<0.001) (**Figure 11B**).* Together with the IHC results from VHL-associated HBs, these data strongly suggest that PNPLA3 is significantly downregulated in both $VHL^{-/-}$ tumor types.

Low levels of PNPLA3 in $VHL^{-/-}$ cells stimulate oncogenic HIF signaling and cell growth.

To further understand the functional effect of PNPLA3 downregulation in $VHL^{-/-}$ cells, we used the ccRCC cell line 786-O. These cells have detectable levels of endogenous PNPLA3 despite their loss of VHL (***Figure 11C***), making them the ideal cellular context to study the functional role of PNPLA3 downregulation. We used two independent shRNA molecules targeting the coding region of PNPLA3 to suppress the protein expression. Downregulation of PNPLA3 in 786-O cells was confirmed by qRTPCR and achieved at least sixty percent when compared to the shRNA GFP control (***Figure 11C***). The knockdown of PNPLA3 with both hairpins was followed by a significant upregulation of *NOS2* and an increase in the other HIF target-genes *EGLN3*, *CA12* and *EPOR* (***Figure 11C***, *p<0.05*). The same effect was observed upon downregulation of PNPLA3 in another ccRCC cell line (UMRC2, data not shown). This

result indicates that downregulation of PNPLA3 synergizes with the VHL$^{-/-}$ phenotype and further stimulates the oncogenic activity of HIF signaling in VHL$^{-/-}$ cells.

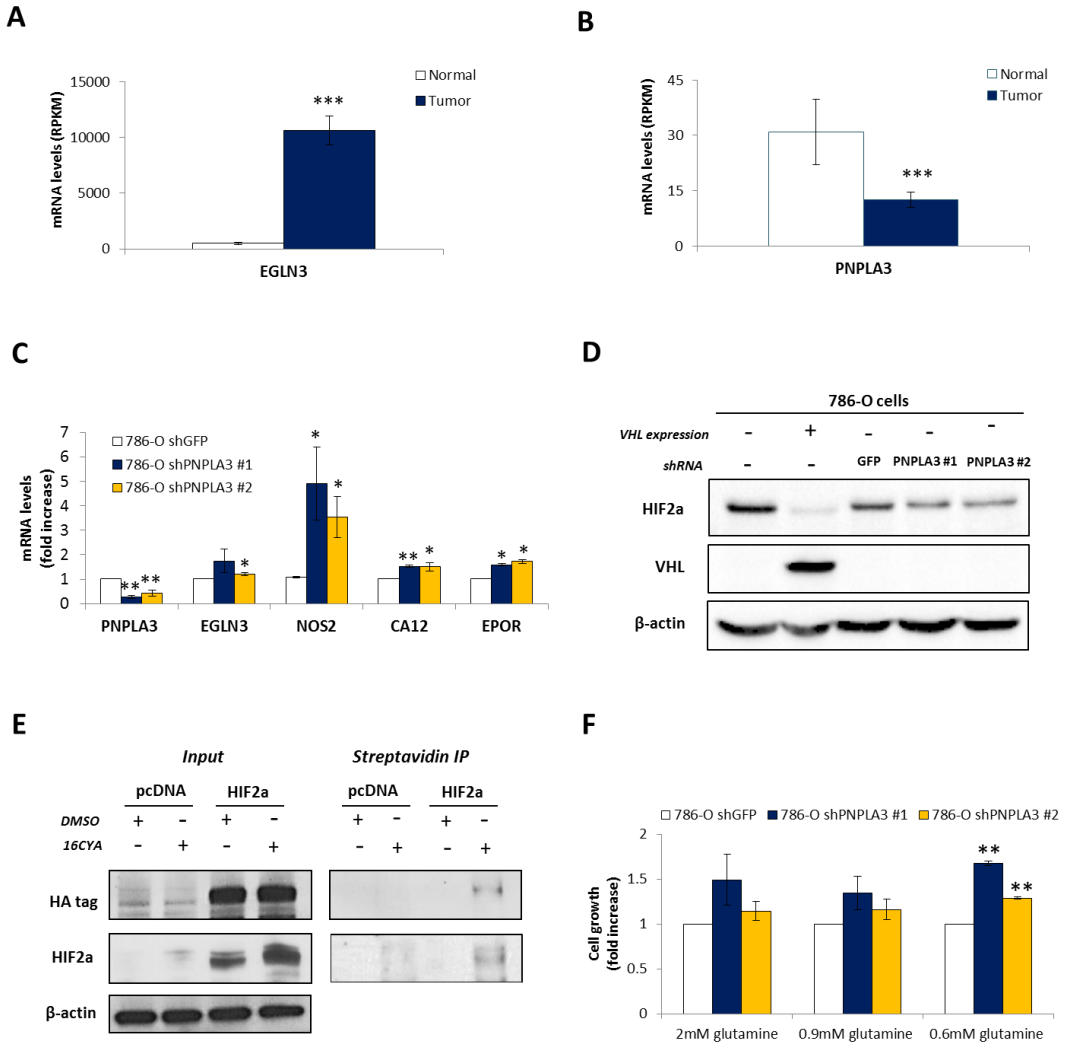

Figure 11 - Downregulation of PNPLA3 occurs in VHL-negative ccRCC tumors and stimulates HIF signaling and cell growth. (A) mRNA levels of the bona-fide HIF target gene *EGLN3* and the *PNPLA3* gene **(B)** in ccRCC tumors and respective normal kidney (72 pair samples, TCGA data) (in reads per kilobase per million reads - RPKM). **(C)** Effect of PNPLA3 knockdown in the expression of HIF target genes. mRNA levels of *PNPLA3* and the HIF-target genes *EGLN3*, *NOS2*, *CA12* and *EPOR* were measured in ccRCC 786-O cells infected with shRNA against GFP (control) or two different shRNA against PNPLA3 (#1 and #2). Gene expression levels were measured by qRTPCR and normalized to the expression of *28S* (n=3). **(D)** Western blotting for HIF2α, VHL and the internal control beta-actin in ccRCC cell line 786-O with or without reconstituted VHL protein, in comparison with 786-O cells infected with shRNA GFP, shRNA PNPLA3 #1 or shRNA PNPLA3 #2. **E)** Posttranslational binding of palmitate to HIF2α. 293A cells were transfected with constitutive active HA-HIF2α (P405A/P531A) or pcDNA3.1 empty vector control. After incubation with the palmitate-alkine probe (16CYA) or DMSO, and subsequent click chemistry, palmitate-bound proteins were immunoprecipitated with anti-streptavidin conjugated-beads and immunoblotted with anti-HA and anti-HIF2α antibodies. **F)** Effect of PNPLA3 knockdown in the growth of ccRCC cells cultured under different glutamine concentrations. ccRCC 786-O cells were infected with shRNA GFP, shRNA PNPLA3 #1 or shRNA PNPLA3 #2. Cell growth was quantified by crystal violet and normalized to the shRNA GFP control cells (n=3). Data represent mean ± SEM. *P ≤ 0.05, **P <0.01, ***P < 0.001, unpaired, 2-tailed t test.

Importantly, the enhanced activity of HIF signaling after downregulation of PNPLA3 did not correlate with higher levels of the HIF2α protein, the only HIF isoform expressed in 786-O cells (***Figure 11D***). Thus, we explored other potential mechanisms of HIF2α activation, including posttranslational protein modification. In fact, the covalent binding of lipids to proteins is a major mechanism used in the cell to regulate protein activity [186]. Considering the role of PNPLA3 as an acyl-transferase, which uses different lipid substrates (such as palmitate) to synthesize triglycerides, we tested whether HIF2α is directly modified by palmitoylation. Using the CSS Palm 4 software, we predicted three putative cysteines in the HIF2α coding sequence (and conserved among different species) with high probability of being palmitoylated (data not shown) [187]. To test this hypothesis *in vitro*, we overexpressed the constitutive active form of HIF2α (P to A mutated form) with an upstream HA tag or the pcDNA 3.1 empty vector control in 293A cells. Overnight incubation of the transfected cells with palmitate probe for click chemistry (palmitate-alkine) reveals that HIF2α can be specifically modified by palmitate, as detected by anti-streptavidin immunoprecipitation and sub-sequent immunoblotting for both HA tag and HIF2α (***Figure 11E***). This result was further confirmed in the $VHL^{-/-}$ 786-O cells that express endogenous levels of HIF2α, showing for the first time that the HIF2α transcription factor can be modified by lipids (***Figure S1***). Moreover, preliminary data indicate that downregulation of PNPLA3 using shRNA seems to decrease endogenous HIF2α palmitoylation in $VHL^{-/-}$ cells.

Finally, we evaluated the impact of PNPLA3 downregulation and consequent HIF2α activation in tumor cell growth. We showed that $VHL^{-/-}$ cells with PNPLA3 knockdown (shPNPLA3 #1 and shPNPLA3 #2) grow moderately faster than the control cells (shGFP) *in vitro* ***(Figure 11F)***. This growth difference is significantly enhanced upon metabolic stress

conditions, such as low glutamine levels (p<0.01), which is a relevant stress condition for tumor cells. Taken together, these data demonstrate that downregulation of PNPLA3 is a feature of *VHL*$^{-/-}$ tumors, and strongly suggest that combined loss of PNPLA3 and VHL might provide a selective growth advantage to HB tumor cells, in particular in metabolic stress conditions such as those experienced within the tumor microenvironment.

3.3. Discussion

Hemangioblastomas are heterogeneous tumors formed by two or three cellular components: cancer cells of unknown origin (called *stromal* cells), a rich network of endothelial cells and pericytes, and in some cases hematopoietic cells. Here, we performed whole-exome sequencing in order to characterize the genomic landscape of VHL-associated HB tumors. The origin of the HB *stromal* cells remains unclear and some recent studies hypothesized that these tumor cells are formed by developmentally-arrested hemangioblasts [11,29,32], which would differentiate into distinct cell lineages sharing the same mutational defects. In this study, we showed that only a small fraction of the tumor (median value of 0.23 ± 0.08) is formed by *VHL*$^{-/-}$ tumor cells. Complete inactivation of *VHL* is an early and clonal event that is present in all the HB tumor cells. However, the rest of the cells in the tumor (approximately 80%) do not show biallelic loss of *VHL*, which indicates that they are reactive cells from the tumor microenvironment and are not derived from HB *stromal* cells. The determined tumor fraction in VHL-associated CNS HBs is considerably lower than the average tumor fraction among different cancer types (pan-cancer tumor fraction of 0.79) [188]. A similar result was previously shown for sporadic HBs [125], supporting the hypothesis that both VHL-associated and sporadic HBs are formed by a small percentage of tumor cells and a strong tumor microenvironment. Nevertheless,

the reactive cells of VHL-associated HBs do have a germline mutation in the *VHL* gene ($VHL^{+/-}$). It is possible that a *dose effect* in this tumor suppressor gene implicates a different microenvironmental response. And in fact, a recent study showed that heterozygous deletion of *VHL* delays apoptosis in human hematopoietic cells [189]. Therefore, it remains to be clarified the functional effect of the heterozygous loss of *VHL* ($VHL^{+/-}$) in reactive endothelial and hematopoietic cells, and whether this genotype contributes to tumor proliferation.

The frequency of mutations in the tumor genome is another feature that varies among cancer types, correlating with the origin of tumorigenesis. Carcinogenic and UV-derived tumors achieve very high mutation frequencies while pediatric tumors show very low mutational levels [135,190]. VHL-associated CNS HBs presented a mutational frequency comparable to ccRCCs and significantly higher than Pheochromocytomas (***Figure 6C***). In addition, the mutational signature of both familial and sporadic CNS HBs was very rich in C→T substitutions, which is a consequence of cytosine deamination usually associated with aging [135,190]. This result corroborates with the benign phenotype of CNS HBs that develop slowly during the lifetime of VHL patients. In contrast, while ccRCC tumors and Pheochromocytomas also exhibited C→T transitions, they shared other mutation types such as C→A, C→T, T→C and T→G, showing that their tumorigenesis process is molecularly different from CNS HBs.

Previous studies have identified loss of chromosome 3 as the major CNV event occurring in CNS HBs [125,191]. Here, we confirmed that deletion of chromosome 3 is the main genomic event used in CNS HBs to inactivate *VHL*, as it is present in six out of eight tumors of the discovery cohort. Interestingly, other tumor suppressor genes also localize in this area of chromosome 3p, including PBRM1, BAP1 and SETD2, and are known to be additionally mutated in a subset of ccRCCs [130]. Our analysis of CNS HBs did not detect any mutation in these

other tumor suppressor genes present in chromosome 3. And so far, there are no reports of mutations in those genes contributing to the development of CNS HBs, which may indicate a distinct genomic evolution between CNS HBs and ccRCCs.

In addition to loss of chromosome 3, other CNV events have been identified in CNS HBs, such as gain of chromosome 4 and 1 and loss of chromosomes 19, 22q13.2 and 6 [16,180]. Here, we reported for the first time the complete deletion of chromosome 8 in two independent HB samples (XT6479 and XTB1). Loss of chromosome 8 and specifically 8p is a recurrent CNV event in epithelial cancers and has been associated with poor prognosis in breast cancer patients [192]. This genomic abnormality has been reported to affect the tumor response to chemotherapy (and statins treatment) and has a strong effect in lipid metabolism. Moreover, breast cancer cells lacking the region 8p have a significant upregulation of metabolic enzymes involved in fatty acid synthesis and cholesterol and, interestingly, show a selective growth advantage in conditions of hypoxic stress [192]. In light of this knowledge, our data suggest that loss of both chromosome 3 and chromosome 8 may synergize for the aberrant growth of HB tumor cells in a HIF-dependent microenvironment.

In this study, we identified and validated a somatic mutation in the *PNPLA3* gene. As introduced earlier, PNPLA3 codes for an acyl-transferase that participates in the acylation of the lysophosphatidic acid (LPA) using long-chain free fatty acids to produce phosphatidic acid [182]. This is a key step in the triglyceride synthesis pathway and, for that reason, PNPLA3 is associated with non-alcoholic fatty liver disease and liver adenocarcinoma [193,194]. We showed that the nonsense mutation identified in this study (*PNPLA3* Y191*) leads to a truncated peptide lacking the acyl-transferase activity of the protein, and cancer cells overexpressing the mutant PNPLA3 were no longer able to accumulate triglycerides in the form of lipid droplets. This result raises the possibility that HB cells with loss of PNPLA3 might use LPA and free fatty acids as

substrate molecules for other cellular pathways. Interestingly, LPA has been shown to be an important signaling molecule in the adult and developing brain [195].

The *PNPLA3* mutational event identified herein is relevant to the biology of CNS HBs because these tumor cells are known to exhibit a "clear cell" phenotype, which is due to abnormal lipid metabolism and consequent lipid accumulation [91]. Furthermore, the genomic location of *PNPLA3* (chromosome 22q13) has been reported to be lost in a subset of CNS HBs [16,180], making *PNPLA3* a candidate of high interest for further scientific exploration. Here, we showed that while specific normal cells of the adult cerebellum express PNPLA3, 83% of the analyzed CNS VHL-associated HBs from two independent cohorts (n=18) expressed very low or no levels of PNPLA3. While normal hematopoietic cells in the HB tumors retain strong expression of PNPLA3, most of the $VHL^{-/-}$ HB tumor cells lack PNPLA3 expression. Interestingly, the downregulation of PNPLA3 was also observed in $VHL^{-/-}$ ccRCC tumors (***Figure 11B***). We collected these data from a cohort of 72 sample pairs of ccRCCs and normal kidneys and verified a significant decrease in PNPLA3 levels in the tumor samples. Together these results shed light into the genetics of VHL-associated tumors, revealing that downregulation of PNPLA3 is a feature of $VHL^{-/-}$ cells shared by both VHL-related HBs and ccRCCs. We speculate that the decrease in PNPLA3 activity might occur through different cellular mechanisms including small point mutations (as identified in this study), large chromosomal deletions or epigenetic and transcriptional programs.

Cancer cells exert a tight control over their metabolic pathways as they have a high demand for energy, oncogenic signaling factors and structural molecules to support increased cellular proliferation. Cancer cells lacking VHL exhibit stabilization of the HIF2α oncogene, which represses lipogenesis and β-oxidation, and also promotes the lipid-droplet binding protein

perilipin 2 [90,92,94]. VHL$^{-/-}$ cells are therefore highly dependent on extracellular lipid pools used as substrates and/or stored in cytoplasmatic lipid droplets. Considering the downregulation of PNPLA3 shown in the majority of the analyzed VHL$^{-/-}$ tumors, we investigated the relationship between PNPLA3 levels and HIF signaling. In this study, we found that downregulation of PNPLA3 in a specific HIF2α-driven cell line (786-O), using shRNAs, leads to increased oncogenic HIF signaling with upregulation of bona-fide HIF target genes such as *NOS2*, *CAIX* and *EPOR*. Surprisingly, the enhanced activity of HIF2α upon PNPLA3 downregulation occured independently of changes in HIF2α protein levels. Considering previous studies focused on NRAS and EGFR palmitoylation [186,196], our finding that HIF2α is palmitoylated (***Figure 11D***) provides evidence for a new posttranslational mechanism by which loss of PNPLA3 might decrease HIF2α palmitoylation and promote its oncogenic activity in VHL-associated HBs.

Finally, VHL$^{-/-}$ cells expressing low PNPLA3 levels (shRNA#1 and shRNA#2) exhibited a selective growth advantage compared to control cells, particularly under glutamine-limited conditions. This result highlights the importance of metabolic control in VHL$^{-/-}$ cells, which depend on glutamine for biomass production [88]. Once in metabolic stress conditions (such as low glutamine), VHL$^{-/-}$ cells rely on alternative substrates to survive. Based on these findings, we propose that downregulation of PNPLA3 metabolically adapts these cells to grow faster because long free-fatty acids would be no longer incorporated in lipid droplets and therefore become available for other cellular pathways. Indeed LPA, palmitate and arachidonic acid were shown to promote not only angiogenesis but also oncogenic growth [197]. Loss of PNPLA3 might therefore increase the availability of lipid substrates, having a positive impact in the context of VHL$^{-/-}$ cells.

Here we showed that VHL-associated CNS HBs significantly downregulate PNPLA3 protein levels. This mechanism is likely to synergize with loss of VHL to promote oncogenic

signaling and selective cancer growth. This study reveals a new mechanism of HIF regulation and shows the importance of metabolic control in a fashion that is dependent on the tumor genotype. HIF2α is recognized as the main oncogene responsible for ccRCC development and is expressed in the precursor lesions of VHL-associated HBs [31,32,119]. This new connection between HIF2α oncogenic signaling and the PNPLA3 metabolic enzyme should be explored in the future as a novel strategy to target not only HBs but also other VHL-associated tumors.

3.4. Supplemental data

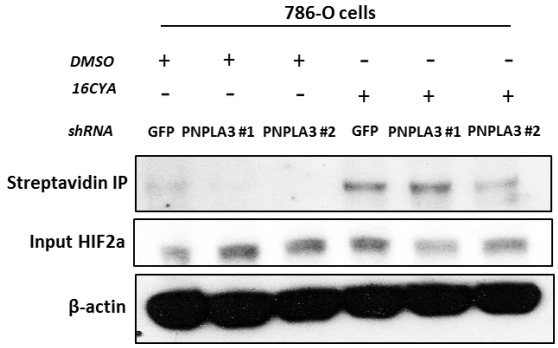

Figure S1: Endogenous HIF2α expressed in VHL$^{-/-}$ 786-O cells is palmitoylated. Posttranslational binding of palmitate to endogenous HIF2α in the VHL$^{-/-}$ cells with downregulation of PNPLA3 (shRNA#1 and shRNA#2) or control shRNA GFP. After incubation with the palmitate-alkine probe (16CYA) or DMSO, and subsequent click chemistry, palmitate-bound proteins were immunoprecipitated with anti-streptavidin conjugated-beads and immunoblotted with anti-HIF2α antibody.

CHAPTER 4

Inhibition of HIF2α is a therapeutic strategy for treatment of VHL disease

The *Chapter 4* of this doctoral thesis is based on the previously published work:

Metelo AM et al. (2015) Journal of Clinical Investigation; 125(5): 1987-97.

4.1. Scientific Background

Patients with a germline mutation in the Von Hippel-Lindau (*VHL*) tumor suppressor gene develop a characteristic constellation of hypervascular tumors, which includes retinal and central nervous system hemangioblastomas (HB), renal cell carcinomas (RCC), pheocromocytomas, pancreatic neuroendocrine tumors, and papillary cystadenomas of the pancreas and middle ear as well as erythrocytosis [198]. The VHL protein targets the Hypoxia Inducible Factor (HIF) family members for destruction, therefore loss-of-pVHL function in cells leads to constitutive upregulation of HIF1α and 2a. HIFs transactivate genes involved in angiogenesis, erythropoiesis, metabolism, cell proliferation and metastasis [52]. Typical HIF-target genes include vascular endothelial growth factor alpha (*VEGFA*), transforming growth factor beta (*TGFB1*), erythropoietin (*EPO*), erythropoietin receptor (*EPOR*), transferrin, and angiopoietin 1 [52,199].

Most human epithelial cells express both *HIF1α* and *HIF2α* paralogs, with overlapping but also distinct and opposing functions [110]. While both are activated by hypoxia and loss-of-VHL, it is well established that HIF2α, in contrast to HIF1α, acts as an oncogene, at least in the case of VHL-related and sporadic RCC. Developmentally-arrested structures present in the CNS of VHL patients express HIF2α and not HIF1α, indicating that specifically HIF2α is also involved in CNS Hemangioblastoma formation [18,31]. HIF2α promotes cellular proliferation, cancer metabolism, stemness and c-MYC activity, and its expression in human RCC tumors correlates with poor prognosis [88,119,200]. Expression of HIF1α, on the other hand, displays tumor suppressor activity, inhibiting the growth of RCC cells in culture and in xenograft animal models[201]. It is therefore not surprising that xenograft and transgenic animal models strongly

indicate that inactivation of HIF2α is both necessary and sufficient for the tumor suppressor function of VHL protein [108,119,121,202].

Currently, there is no medical therapy available for treatment or prevention of VHL disease [1]. Surgery is the main treatment modality. Unfortunately, VHL patients have to undergo multiple surgical procedures for tumors that appear serially over a lifetime. Repeated surgeries often lead to significant injury to the normal renal or brain parenchyma and result in serious morbidity or mortality. Often, surgical intervention is not even feasible because of the location of the HB in the brain stem or other vital structures. Sunitinib, an oral inhibitor of receptor tyrosine kinase VEGFR2, targets only one of multiple downstream targets of HIF2α. Medical treatment of a small cohort of VHL patients with sunitinib showed only a modest effect in RCC, and no effect in brain or retinal HB [152].

Pharmacologic inhibition of HIF2α appears an ideal therapeutic strategy for VHL disease and HIF2α-driven tumors [203,204]. HIF2α inhibitors should yield a wide therapeutic window, since VHL proficient, well-oxygenated cells require minimal HIF2α expression. We identified such inhibitors in a mammalian cell-based screen [205]. We previously showed that they promote selectively the binding of intracellular Iron Regulatory Protein 1 (IRP1) to the 5'-UTR of *HIF2α* mRNA, resulting in repression of HIF2α, but not HIF1α, translation [205]. There is now compelling evidence that IRP1 is critical for regulation of HIF2α activity in mammalian cells [205,206]. In addition to cell culture experiments, it has been shown that mice engineered to lack IRP1 develop HIF2α-dependent erythrocytosis and pulmonary hypertension [207–209].

Here we provide for the first time evidence that HIF2α inhibitors significantly improve the phenotype of VHL disease in a vertebrate animal model. Zebrafish embryos which are homozygous for loss-of-*vhl* function mutations develop Epo-driven erythrocytosis, similarly to VHL patients [162,163]. In addition to erythrocytosis, *vhl*$^{-/-}$ embryos develop complex blood vessel

networks in the brain and in the retina, resembling the highly vascular hemangioblastomas encountered in VHL patients. Moreover, *vhl*$^{-/-}$ embryos exhibit a proliferative liver and kidney phenotype that likely reflects aspects of the *VHL*-associated tumor biology as well as cardiomegaly with decreased cardiac contractility. Taking into account that hypoxia, angiogenesis and erythropoiesis constitute pathways conserved between humans and fish [210–212], the *vhl* zebrafish model currently stands as the best animal model to study HIF2α inhibitors and the biology of VHL disease *in vivo*.

In this study we show that systemic administration of HIF2α inhibitor compound 76 significantly decreases HIF2α signaling *in vivo* in both hypoxia-challenged and *vhl*$^{-/-}$ zebrafish models. This HIF2α repression rescues *vhl*$^{-/-}$ embryo pathologic angiogenesis and erythropoiesis, normalizes *vhl*$^{-/-}$embryo impaired cardiac contractility and improves their survival during early larval stage. To the best of our knowledge, this is the first time that the transcription factor HIF2α is targeted *in vivo*. Optimization of these HIF2α small molecule inhibitors through structure-function analysis and medicinal chemistry approaches are required for further development of these compounds for pre-clinical and clinical use, which may have a profound impact on the treatment of human VHL disease.

4.2. Experimental Results

HIF2α inhibitors suppress hypoxia-induced HIF target genes in vivo

The signaling pathways regulating angiogenesis, erythropoiesis and the cellular response to hypoxia are highly conserved among vertebrates, rendering zebrafish embryos attractive models to test therapeutic compounds *in vivo*. Protein alignment reveals a 70% similarity between human HIF2α and zebrafish Epas1b and a 64% similarity between human HIF2α and zebrafish Epas1a. Both of these zebrafish genes harbour an IRE (Iron Responsive Element) loop in their 5'-UTRs, where the IRE consensus sequence and the mandatory 5' cytosine are conserved (***Figure 12A***). Previously, we showed that the presence of an IRE in the 5'-UTR of human *HIF2α* is necessary and sufficient for the activity of HIF2α inhibitors [205]. These inhibitors repress HIF2α translation by promoting the binding of IRP1 to the 5'-UTR IRE in *HIF2α* mRNA (***Figure 12B***). In contrast to *HIF2α*, the 5'-UTR of *HIF1α* does not contain a functional IRE and, consequently, compound 76 fails to suppress HIF1α translation in mammalian cells [205]. Similarly to mammalian genes, zebrafish *HIF2α* orthologs *epas1a* and *epas1b,* but not the *HIF1α* orthologs *HIF1αa* and *HIF1αb,* contain an IRE within the 5'-UTR (***Figure 12A***). To functionally validate the zebrafish IREs we subcloned the zebrafish 5'-UTR corresponding to each paralog (*epas1a, epas1b, HIF1αa* and *HIF1αb*) upstream of the luciferase coding sequence of reporter plasmids. We transfected the reporter plasmids into mammalian cells and tested the ability of compound 76 to suppress luciferase translation regulated by each zebrafish 5'-UTR. Compound 76 suppressed the *epas1a* and *epas1b* 5'-UTR-directed luciferase translation, but not the *HIF1αa* and *HIF1αb* 5'-UTR-directed translation of luciferase (***Figure 12C***). These data suggest that the zebrafish *epas1a* and *epas1b* retain functional IREs within their 5'-UTR, similarly to their

mammalian ortholog *HIF2α*, while *HIF1αa* and *HIF1αb* do not. In addition they suggest that compound 76 specifically represses *epas1a* and *epas1b* but not *HIF1αa* and *HIF1αb* translation.

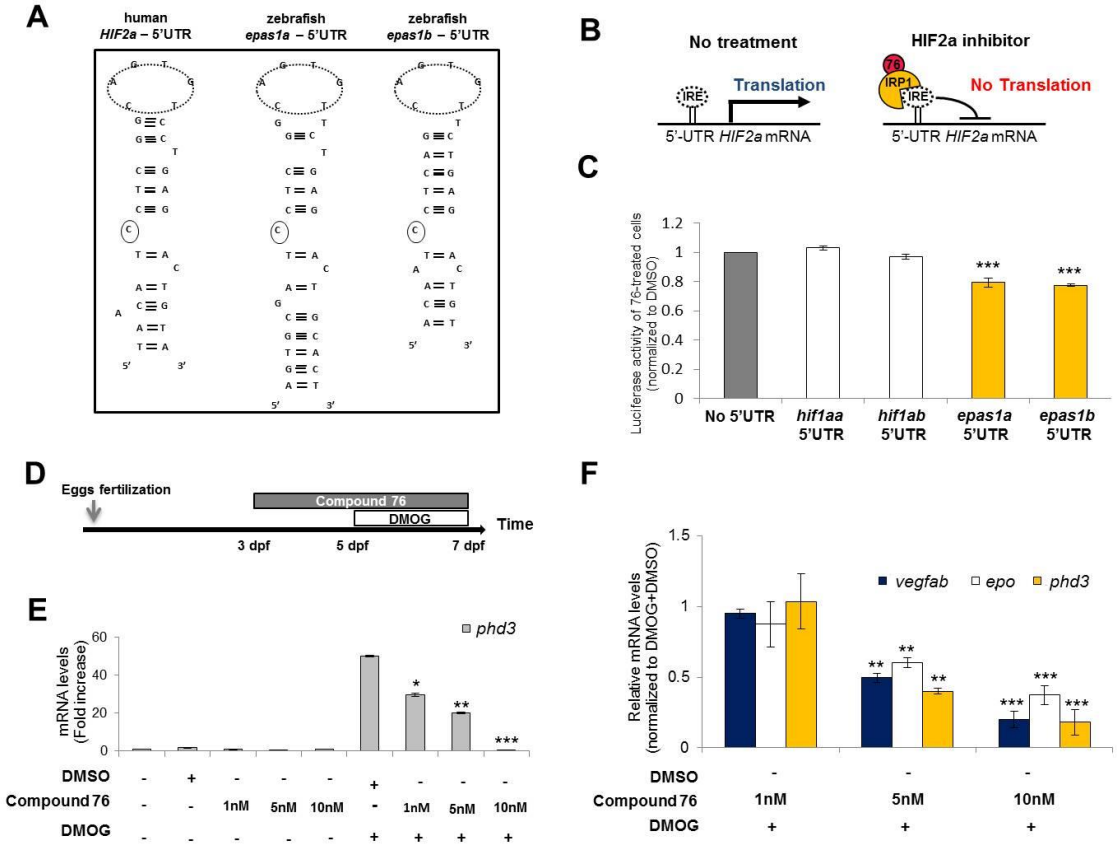

Figure 12 - Small molecule compound 76 suppresses DMOG-induced expression of HIF2α-target genes in wild type zebrafish embryos. (A) Sequence comparison between iron responsive elements (IREs) present in the 5'-UTR of human *HIF2α*, zebrafish *epas1a* and zebrafish *epas1b*. The IRE consensus loop and the mandatory 5' cytosine are circled. **(B)** Iron responsive protein 1 (IRP1) binds to *HIF2α* IRE, suppressing the translation of *HIF2α* mRNA. Compound 76 promotes binding of IRP1 to *HIF2α* IRE and inhibits HIF2α translation. **(C)** Luciferase expression in U2OS cells transfected with pTol2 vectors containing the 5'-UTR sequences of *HIF1αa*, *HIF1αb*, *epas1a* or *epas1b* upstream of the luciferase ORF. The cells were treated with 5µM of compound 76 or DMSO control for 30 hours. Luciferase expression levels were normalized by protein levels. **(D)** Treatment protocol: Wild type embryos were treated with compound 76 or DMSO vehicle control from 3-7 dpf. Embryos were challenged with the hypoxia chemical mimetic DMOG from 5-7 dpf. **(E)** mRNA expression of the HIF-target gene *phd3* in wild type embryos challenged with 100µM of DMOG and treated with compound 76 (as indicated) or vehicle only control. Gene expression levels were normalized by *18S* gene expression. **(F)** Relative mRNA levels of HIF-target genes *phd3*, *epo* and *vegfab*, normalized to DMOG-challenged samples treated with vehicle only control. All experiments were performed in biological triplicate. Data represents mean ± SEM. Unpaired, two-tailed *t* test was used for statistical analysis.* $p<0.05$, ** $p<0.01$, *** $p<0.001$.

To test whether the prototypic HIF2α inhibitor (compound 76) suppresses HIF activity in vivo we challenged wild type zebrafish embryos with the chemical hypoxia mimetic Dimethyloxalylglycine (DMOG) in the presence of compound 76 or vehicle only control. DMOG inhibits HIF prolyl-hydroxylases, which target HIF for degradation, and therefore treatment of wild type embryos with this chemical mimetic is expected to stabilize the regulatory subunits of Hif paralogs and activate their downstream-targets [162,213]. Wild type (*wt*) embryos treated with 100μM DMOG for 48 hours (***Figure 12D***) exhibit a remarkable upregulation of the bona-fide Hif-target genes Prolyl-hydroxylase 3 (*phd3*), Erythropoietin (*epo*), and Vascular Endothelial Growth Factor ab (*vegfab*) (***Figure 12E, Figure 12F and Figure S2***). Pre-incubation of embryos with 1, 5, and 10nM of compound 76 is sufficient to significantly inhibit DMOG-induced Hif signaling in a dose-dependent manner, as assessed by qRT-PCR of Hif-target genes from whole embryo derived mRNA (***Figure 12E and 12F***). The compound 76 did not decrease the expression of the non-Hif target genes Neurofibromin 2a (*nf2a*) and Retinoblastoma 1 (*rb1*) (data not show).

HIF2α inhibitors suppress hypoxia-induced erythrocytosis and angiogenesis

Hypoxia leads to HIF-dependent erythrocytosis and angiogenesis, through activation of Erythropoietin (*EPO*) and Erythropoietin Receptor (*EPO-R*) as well as several of the angiogenesis promoting genes [83,214,215]. Given the biochemical evidence that compound 76 inhibits Hif-target genes in vivo, we tested whether it can alter the animal's physiology in response to hypoxia.

To image the combined effect of angiogenesis (expansion of the vascular bed) and erythrocytosis (increase in intravascular erythrocyte mass) we stained wild type embryos with O-dianisidine, a dye that stains hemoglobin. Treatment of wild type embryos with DMOG activates

Hif, leading to both erythrocytosis and sprouting of blood vessels. This effect is particularly visible in the animal trunk and it is completely rescued by treatment with 10nM of compound 76 (***Figure 13A***). We objectively quantified the differences in O-dianisidine staining by creating a computer-assisted classifier that recognizes the stained pixels in the image (***Figure 13B***). Image analysis shows that 48 hour treatment of zebrafish embryos with DMOG induces a 2-fold increase in their hemoglobin content and angiogenic sprouting, both of which are suppressed by treatment with 10nM compound 76 (***Figure 13C***).

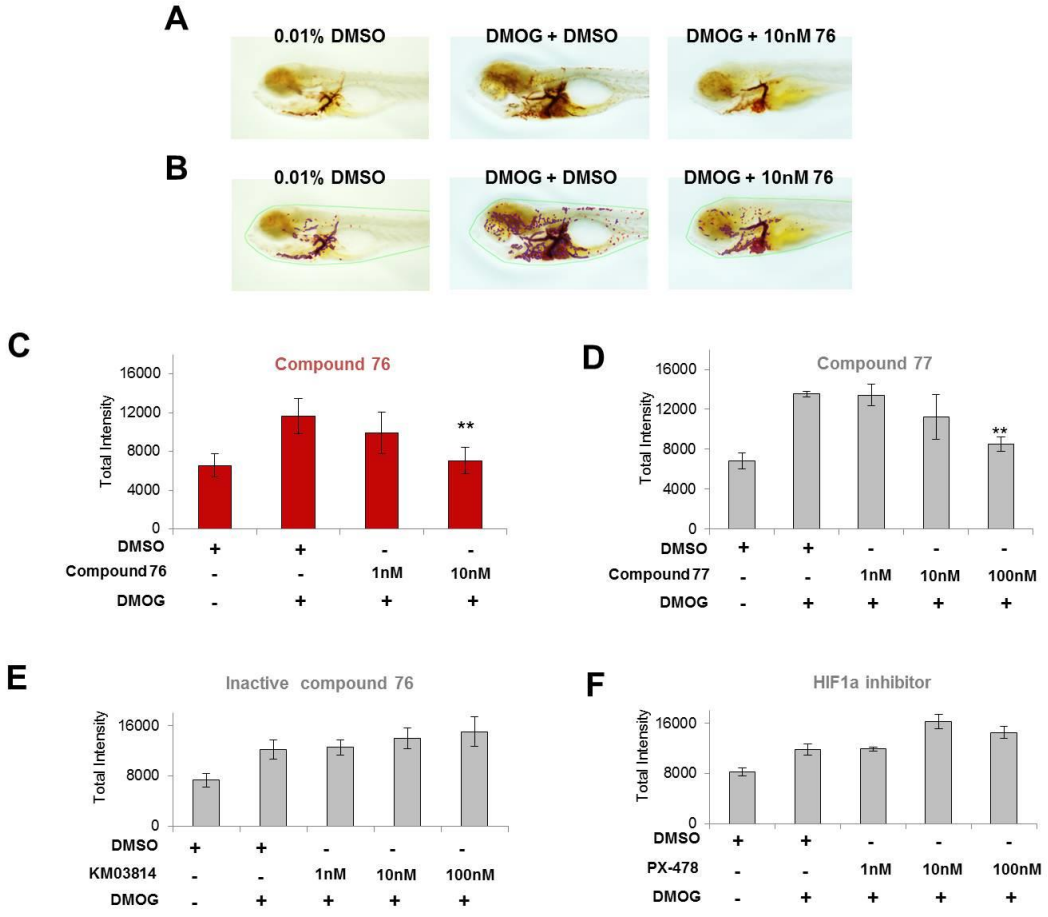

Figure 13 - Small molecule compound 76 suppresses DMOG-induced erythropoiesis and angiogenesis in wild type zebrafish embryos. (A) O-dianisidine staining of 7dpf embryos challenged with DMOG and treated with compound 76 at 10 nM or vehicle only control. **(B)** Analysis of the images by a computerized pixel-quantification algorithm. **(C)** Computerized quantification of total intensity for *wt* embryos treated with HIF2α inhibitor compound 76; **(D)** Computerized quantification of

total intensity for *wt* embryos treated with HIF2α inhibitor compound 77; **(E)** Computerized quantification of total intensity for *wt* embryos treated with an inactive form of compound 76; **(F)** Computerized quantification of total intensity for *wt* embryos treated with PX-478 (HIF1α inhibitor). The computerized quantification of each group was based on the analysis of at least 10 embryos. All experiments were performed in biological triplicate. Data represents mean ± SEM. Unpaired, two-tailed *t* test was used for statistical analysis. ** $p<0.01$

As previously described, compound 76 is a specific inhibitor of HIF2α and not HIF1α in both the mammalian and the fish models. This specificity is further supported by the observation that a second HIF2α inhibitor (compound 77) rescues DMOG-induced erythrocytosis and angiogenic sprouting (***Figure 13D***), while an inactive form of compound 76, compound KM03814, and the HIF1α inhibitor PX-478 failed to do so (***Figure 13E and 13F***).

The zebrafish orthologs of mammalian HIF2α are critical for the zebrafish erythropoiesis

Zebrafish harbour four distinct hypoxia inducible factor genes but their specific roles in hypoxia signaling are unclear. To investigate the relative contribution of the zebrafish paralogs in the response of the animals to hypoxia we compared wild type zebrafish embryos (*wt*) to embryos in which *HIF1αb* or *epas1b* were knocked out (referred to as *HIF1αb* or *epas1b* embryos). Treatment of *wt* embryos with the chemical mimetic DMOG resulted in a specific 2-fold upregulation of *epas1a* mRNA expression, while the expression of the other Hif paralog mRNAs did not change significantly (***Figure 14A***). The DMOG-mediated induction of *epas1a* mRNA was even greater in the *HIF1αb* mutants and *epas1b* mutants (4-fold increase compared to *wt* animals) (***Figure 14B***). These observations suggest that *epas1a* putatively contributes greater than the other Hif paralogs to the overall response of the animals to hypoxia, at least at embryo stage of development. The increased expression of *epas1a* mRNA in the *HIF1αb* and *epas1b* mutants correlates with an enhanced ability of compound 76 to suppress the DMOG-induced upregulation of *epo* in these mutants (***Figure 14C***). The above data suggest that *epas1a*

is the main paralog that mediates the hypoxic upregulation of *epo* and it is likely the main target of compound 76.

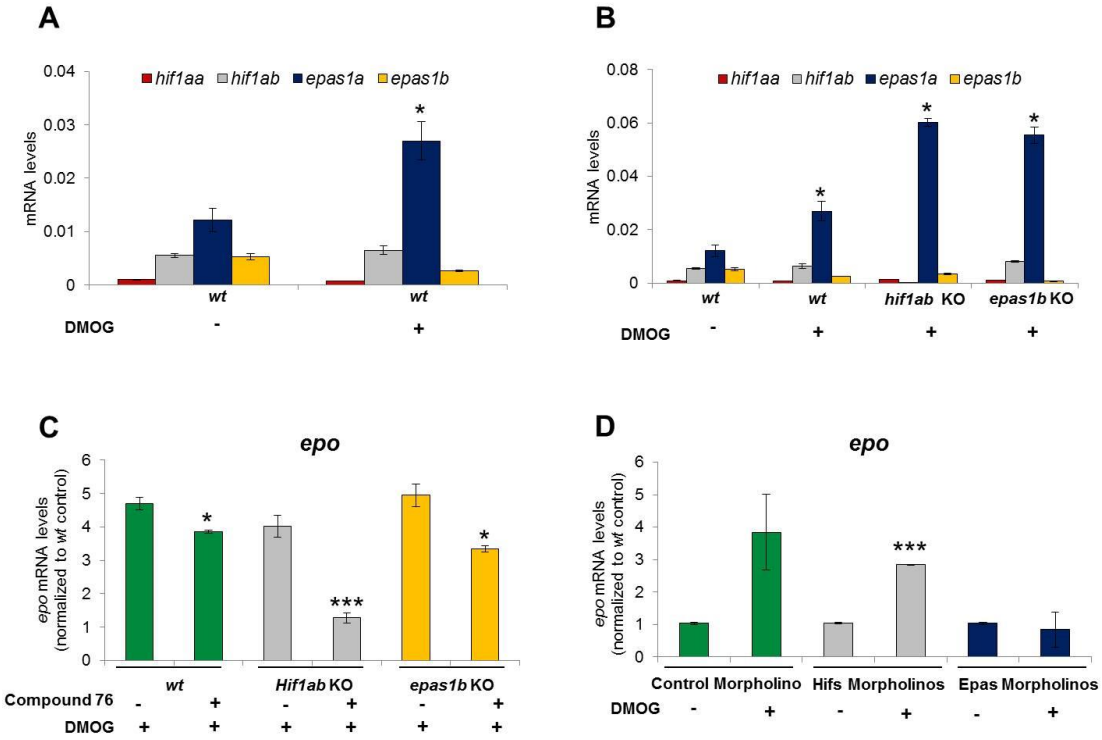

Figure 14 - *Epas1a* paralog is significantly upregulated by hypoxic conditions and is the main paralog transactivating Erythropoietin. (A) Expression of *HIF1αa*, *HIF1αb*, *epas1a* and *epas1b* paralogs in *wt* embryos treated with DMOG or vehicle control from 2dpf to 4dpf. **(B)** Expression of zebrafish *hif* paralogs (*HIF1αa*, *HIF1αb*, *epas1a*, *epas1b*) in *HIF1αb* and *epas1b* mutant embryos (*HIF1αb* KO and *epas1b* KO) treated with DMOG or vehicle control from 2dpf to 4dpf. **(C)** Effect of compound 76 on erythropoietin (*epo*) expression in *wt*, *HIF1αb* KO or *epas1b* KO embryos treated with DMOG or vehicle control from 3dpf to 5dpf. **(D)** Changes in DMOG-induced expression of erythropoietin in *wt* embryos injected with control morpholino, *HIF1αa* and *HIF1αb* combined morpholinos (hifs morpholinos) or *epas1a* and *epas1b* combined morpholinos (epas morpholinos) and treated with DMOG from 3dpf to 4dpf. Gene expression levels were obtained by qRT-PCR and normalized to the expression of *18S*. All experiments were performed in biological triplicate. Data represents mean ± SEM. Unpaired, two-tailed *t* test was used for statistical analysis. * $p<0.05$, *** $p<0.001$

To further corroborate the role of the zebrafish orthologs of mammalian *HIF2α* (*epas1a* and *epas1b*) in the hypoxia phenotype, we injected *wt* embryos with morpholinos targeting either the translation of *epas1a* and *epas1b* in combination or *HIF1αa* and *HIF1αb* in combination, and quantified the expression of *epo* in response to DMOG. The specificity of the morpholinos for

each paralog was verified in reporter experiments (***Figure S3***). Combined targeting of *epas1a* and *epas1b* led to ablation of *epo* and *vegfab* induction (***Figure 14D and Figure S4***). In contrast, combined targeting of *HIF1αa* and *HIF1αb* proteins did not significantly change *epo* induction by DMOG. Taken together these data suggest that the hypoxic upregulation of *epo* is preserved between zebrafish and mammals and is mediated by the *HIF2α* homologs. This indicates that the HIF2α inhibitors used in this work mainly act by supressing translation of *HIF2α* homologs.

HIF2α inhibitors suppress aberrant expression of HIF target genes in the vhl mutant zebrafish

Vhl$^{-/-}$ zebrafish display the human VHL disease signature phenotypes of erythrocytosis and inappropriate vessel proliferation [162,163] (***Figure 15A***). In humans, HIF2α is a critical target of VHL tumor suppressor protein and inactivation of HIF2α in genetically engineered mice ameliorates the loss-of-pVHL phenotypes [83,94,159,202,216]. As described above, zebrafish expresses four Hif paralogs. To provide insights into the putative contribution of each paralog to the development of the *vhl*$^{-/-}$ embryo phenotype we compared the expression of *HIF1αa* and *HIF1αb* (homologs of mammalian *HIF1α*) as well as *epas1a* and *epas1b* (homologs of mammalian *HIF2α*) during the development of *vhl*$^{-/-}$ animals to their wild type or heterozygote siblings (***Figure 15B***). In wild type embryos *epas1* mRNA is the main paralog expressed over the period spanning 24 hours to 12 dpf (***Figure 15B***, lower panel). In the *vhl*$^{-/-}$ embryos *epas1a* expression raises sharply at 3dpf and, in contrast to sibling wild type or heterozygote embryos, it does not diminish at 4 dpf, but remains elevated up to 7dpf. Of note, the *epas1a* paralog is both the main paralog constitutively expressed in *vhl*$^{-/-}$ zebrafish embryos and the one induced by chemical hypoxia mimetics in *wt* embryos, as we showed above. *Epas1a* is the ortholog of the mammalian *HIF2α*; the latter was shown to mediate many loss-of-pVHL phenotypes in *VHL* KO mice [83,94,159,216] and to drive the growth of pVHL-deficient renal cell carcinoma in humans.

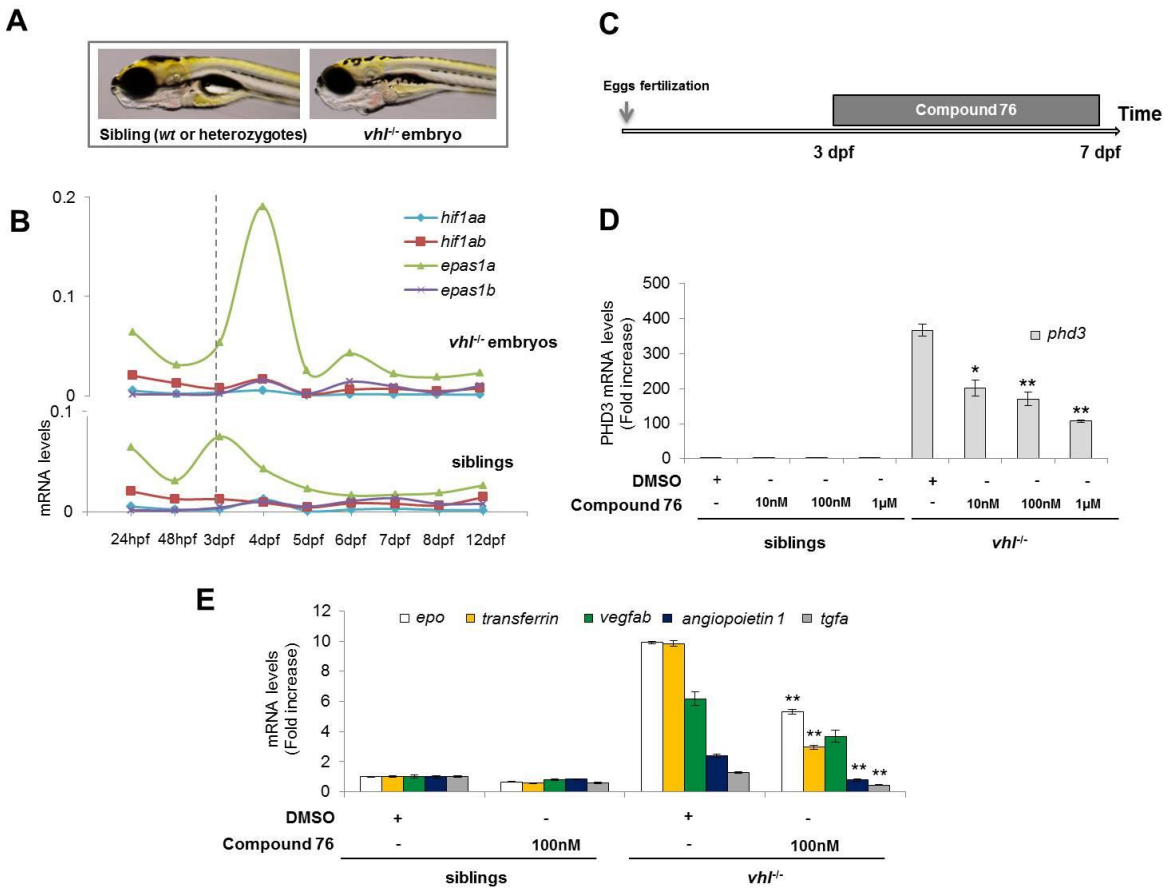

Figure 15 - HIF2α inhibitor compound 76 suppresses the expression of HIF-target genes in *vhl*$^{-/-}$ embryos. (A) Morphologic differences between *vhl*$^{-/-}$ embryos and their siblings (*wt* or *vhl*$^{+/-}$ embryos) at 7dpf. **(B)** Expression profile of zebrafish orthologs of human *HIF1A* (*HIF1αa* and *HIF1αb*) and human *HIF2A* (*epas1a* and *epas1b*) during development of *vhl*$^{-/-}$ embryos and their siblings. **(C)** Treatment protocol. *Vhl*$^{-/-}$ embryos and their siblings were treated with compound 76 or DMSO vehicle control from 3-7 dpf, at the indicated concentrations. **(D-E)** Expression of the HIF-target genes *phd3* **(D)** and *epo, transferrin, vegfab, angiopoietin 1* and transforming growth factor alpha (*tgfα*) **(E)**, in 7dpf *vhl*$^{-/-}$ embryos and their siblings, treated with compound 76 at the indicated concentrations or vehicle only control. Gene expression levels were obtained by qRT-PCR and normalized to the expression of 18S. All experiments were performed in biological triplicate. Data represents mean ± SEM. Unpaired, two-tailed *t* test was used for statistical analysis. * $p<0.05$, ** $p<0.01$

To test whether compound 76 suppresses Hif signaling in *vhl*$^{-/-}$ embryos, we treated 3dpf *vhl*$^{-/-}$ animals and their wild type or heterozygous siblings with this inhibitor for four days (***Figure 15C***). The elevated expression of HIF homologs in the *vhl*$^{-/-}$ zebrafish results in a robust activation of Hif signaling. For example, expression of *phd3*, a bona fide Hif target gene, is

increased 400-fold in *vhl*$^{-/-}$ embryos, compared to sibling embryos (*wt* or heterozygotes) (***Figure 15D***). Treatment of *vhl*$^{-/-}$ embryos with compound 76 significantly suppressed the expression of *phd3* in a dose-dependent manner (***Figure 15D***). In addition, all Hif-target genes tested (erythropoietin, transferrin, vascular endothelial growth factor ab, angiopoetin 1, and transforming growth factor alpha) were significantly downregulated by compound 76 (***Figure 15E***).

HIF2α inhibitors suppress pathologic erythropoiesis and angiogenesis in vhl$^{-/-}$ *embryos*

One of the most prominent phenotypes of *vhl*$^{-/-}$ embryos is the development of erythrocytosis and sprouting of blood vessels in the trunk [162], as shown by O-dianisidine staining (***Figure 16A-B***). Treatment of 5dpf *vhl*$^{-/-}$ embryos with compound 76 significantly decreased O-dianisidine staining intensity (***Figure 16A-B***).

Staining with O-dianisidine reflects the amount of hemoglobin/number of red blood cells and their distribution in the expanded vascular bed. To test the effect of compound 76 on each of these processes we quantified separately the changes induced by compound 76 on erythroid hematopoiesis and the formation of vasculature.

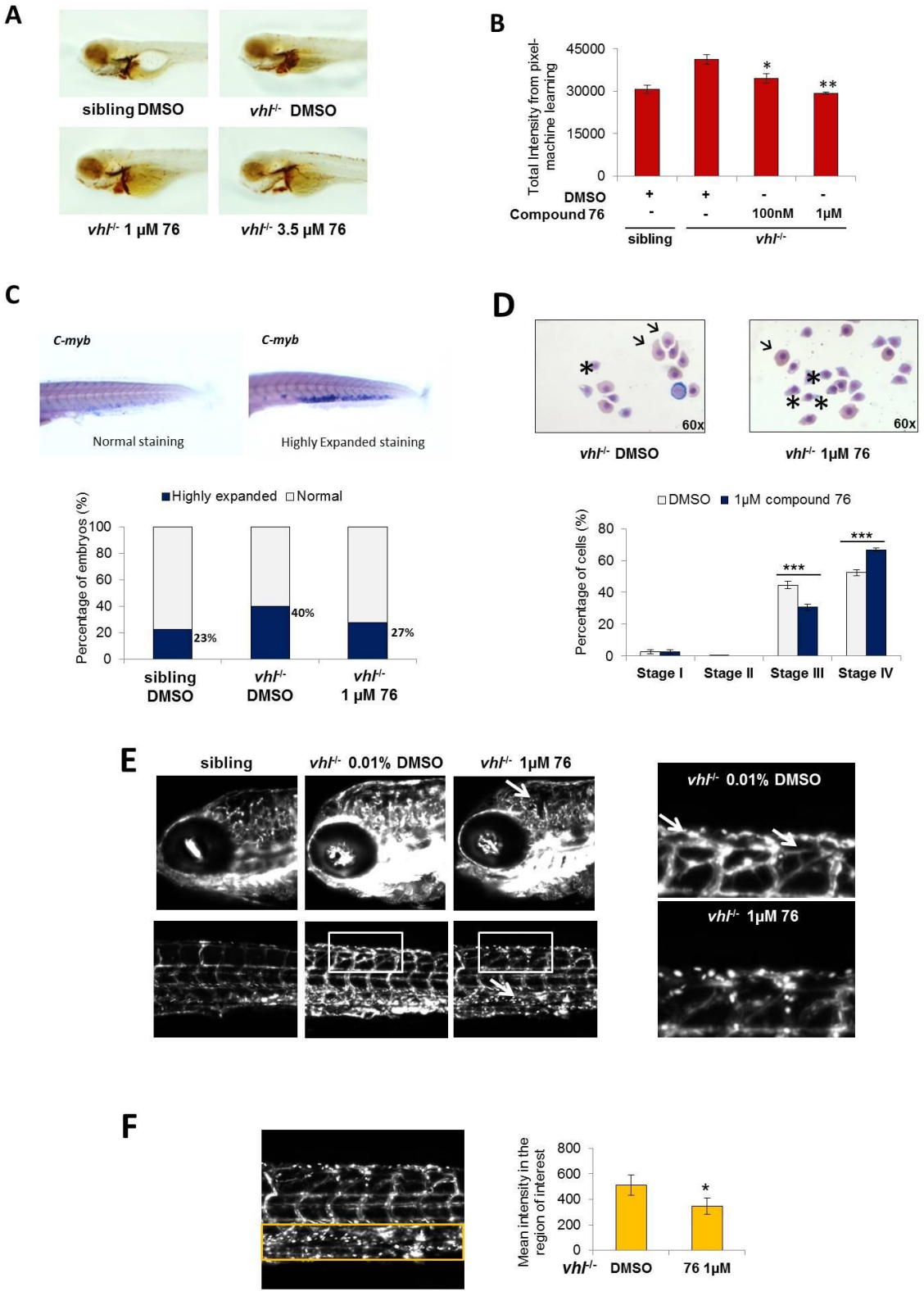
A
sibling DMSO
vhl-/- DMSO
vhl-/- 1 µM 76
vhl-/- 3.5 µM 76
B
Total Intensity from pixel-machine learning
45000
30000
15000
0
*
**
DMSO
Compound 76
100nM
1µM
sibling
vhl-/-
C
C-myb
Normal staining
Highly Expanded staining
Highly expanded
Normal
Percentage of embryos (%)
23%
40%
27%
sibling DMSO
vhl-/- DMSO
vhl-/- 1 µM 76
D
60x
vhl-/- DMSO
vhl-/- 1µM 76
DMSO
1µM compound 76
Percentage of cells (%)
***
Stage I
Stage II
Stage III
Stage IV
E
sibling
vhl-/- 0.01% DMSO
vhl-/- 1µM 76
F
Mean intensity in the region of interest
800
600
400
200
0
vhl-/- DMSO
76 1µM

Figure 16 - HIF2α inhibitor compound 76 rescues abnormal erythropoiesis and ameliorates the brain and trunk pathology of *vhl*$^{-/-}$ embryos. (A) O-dianisidine staining of 5dpf *vhl*$^{-/-}$ and *wt* embryos, treated with compound 76 or DMSO. The staining intensity was analyzed by a computerized pixel-quantification algorithm **(B)**. **(C)** Whole mount *in situ* hybridization of the erythroid progenitor marker c-*myb* in 5dpf *wt* and *vhl*$^{-/-}$ embryos treated with 1μM compound 76 or DMSO. Embryos were imaged and divided into categories according to a normal or highly expanded c-*myb* staining in the caudal hematopoietic tissue (CHT). **(D)** May-Grunwald/Giemsa staining of red blood cells obtained from 8dpf *vhl*$^{-/-}$ embryos treated with compound 76 or DMSO. Stained red blood cells were imaged with a 40X objective and divided into four differentiation stages: I – basophilic erythroblast; II – polychromatophilic erythroblast; III – orthochromatophilic erythroblast (black arrow); IV – erythrocyte (black asterisk). **(E)** Vessel proliferation in 5dpf Fli1-GFP *vhl*$^{-/-}$ embryos and siblings; Fli1-GFP *vhl*$^{-/-}$ embryos treated with compound 76 or DMSO from 3-5dpf. Z-series of confocal microscopy images were obtained with a 10X objective and merged. **(F)** GFP intensity signal in the CHT of 7dpf *vhl*$^{-/-}$; Fli1-GFP embryos treated with compound 76 or DMSO from 3dpf to 7dpf. Using a GFP image of the tail, the region of interest (ROI) was selected and centered in the CHT (orange rectangle). The mean intensity within the selected ROI was quantified using Image-J. Data represents mean ± SEM. Unpaired, two-tailed *t* test was used for statistical analysis. * $p<0.05$; ** $p<0.01$; *** $p<0.001$

Vhl$^{-/-}$ embryos display an increased number of circulating erythroid progenitors and erythroid markers when compared to *wt* embryos [162]. In order to investigate whether compound 76 could affect erythropoiesis and erythroid progenitors, whole-mount *in situ* hybridization for the erythroid progenitor marker *c-myb* was carried out in 5dpf *vhl*$^{-/-}$ embryos. The results indicate that compound 76 decreased the percentage of *vhl*$^{-/-}$ embryos with expanded erythroid progenitor marker *c-myb* in the caudal hematopoietic tissue (***Figure 16C***). Moreover, compound 76 significantly decreased the number of orthochromatophilic erythroblasts (undifferentiated red blood cells in stage III; indicated by black arrows) present in the 8dpf *vhl*$^{-/-}$ blood smears (from 45% to 31%), and increased the number of differentiated erythrocytes (from 52% to 67%; indicated by black asterisks) (***Figure 16D***). These data indicate that this HIF2α inhibitor decreases the amount of red blood cells in *vhl*$^{-/-}$ embryos possibly by promoting their differentiation.

In order to quantify the effect of compound 76 in the pathologic angiogenesis of *vhl*$^{-/-}$ embryos, we crossed the transgenic GFP-*fli1*$^{+/+}$ with the *vhl*$^{+/-}$ line. Fli1 is an established marker of endothelial cells in mice and Fli1 promoter-driven GFP labels the vasculature of zebrafish embryos [217]. *Vhl*$^{-/-}$ embryos form an abnormal vascular network in the brain, the retina and the tail (***Figure 16E***), reminiscent of the highly vascularized human retinal and CNS

hemangioblastomas encountered in VHL patients. A two-day treatment from 3dpf to 5dpf with compound 76 was sufficient to diminish the complex vascularity in the brain and the tail of *vhl*$^{-/-}$ embryos (white arrows in ***Figure 16E***), abrogating some of the abnormal connections between the segmental vessels (***Figure 16E***, right panel).

Interestingly, the Fli1-driven GFP intensity in the caudal hematopoietic tissue (CHT) of *vhl*$^{-/-}$ embryos is also decreased after treatment with HIF2α inhibitor (***Figure 16E***). This hematopoietic tissue works as an intermediate hematopoietic site, being situated between the caudal artery and the caudal vein [218]. It sprouts out of the single vessel caudal vein by extensive angiogenesis at 24hpf, forming a closed and highly vascular plexus with hematopoietic activity. To quantify the GFP intensity in the CHT of *vhl*$^{-/-}$ embryos, we selected a region of interest (ROI) in the image (orange rectangle in ***Figure 16F***), and for each image we quantified the mean intensity within this region. The intensity of GFP positive cells in the CHT of *vhl*$^{-/-}$ embryos is highly enhanced when compared with the siblings (***Figure 16E***, lower panels). As previously described, *vhl*$^{-/-}$ embryos exhibit highly proliferative hematopoiesis in the different hematopoietic tissues, including in the CHT [162]. This enhanced Fli1-GFP intensity in the CHT of *vhl*$^{-/-}$ embryos was not attenuated by treatment with cediranib, a potent and selective inhibitor of VEGF receptor (data not shown), but in contrast, it was diminished after two days of treatment with compound 76 (***Figure 16F***).

HIF2α inhibitor improves cardiac contractility in vhl$^{-/-}$*embryos and enhances their viability*

The zebrafish *vhl*$^{-/-}$ mutants die at the larval stage, around 13 dpf. Severe heart defects and respiratory complications represent possible reasons for the early death, since they display cardiomegaly and pericardial edema. To test whether treatment with compound 76 can rescue

this phenotype we measured the ventricle performance of *vhl*$^{-/-}$ embryos and siblings at 5dpf. A landmark measurement of ventricle performance is given by the fractional shortening, the difference between ventricle diameter during systole and diastole [173]. *Vhl*$^{-/-}$ embryos exhibit a decreased ventricle performance shown by a low fractional shortening value (r=0.54) when compared to siblings (r=0.62) (***Figure 17A***). Treatment with compound 76 significantly improves ventricle fractional shortening of *vhl*$^{-/-}$ embryos (r=0.61, p<0.05).

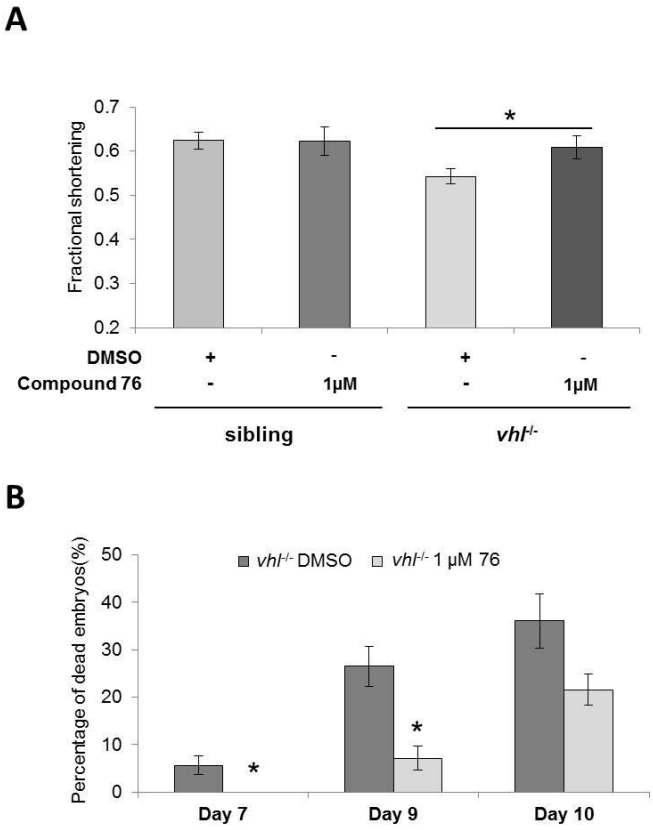

Figure 17 - HIF2α inhibitor compound 76 rescues cardiac contractility of *vhl*$^{-/-}$ embryos and improves their early lethality. **(A)** Quantification of ventricular fractional shortening, a measurement of cardiac performance, in 5dpf *wt* and *vhl*$^{-/-}$ embryos treated with compound 76 for 48 hours (n=12). First way ANOVA test was used for statistical analysis of fractional shortening differences. **(B)** *Vhl*$^{-/-}$ embryos were selected at 3dpf and treated with compound 76 or vehicle only control, until death (n=30). Each experiment was repeated four times. Percentage of dead embryos over time is presented. Unpaired, two-tailed *t* test was used for statistical analysis. Data represents mean ± SEM. * p<0.05

Finally, we investigated whether the molecular and physiologic changes induced by HIF2α inhibitor compound 76 would increase the lifespan of *vhl*$^{-/-}$ embryos. To this end we monitored the survival rates of *vhl*$^{-/-}$ embryos treated with compound 76 or vehicle only control since 3dpf. *Vhl*$^{-/-}$ embryos start dying at 7dpf (***Figure 17B***), potentially due to respiratory and severe heart defects and/or malnutrition. Their death rate increases overtime, and around day 12 post fertilization nearly all animals are dead. Treatment with compound 76 significantly enhances the early animal viability, specifically on 7dpf and 9dpf (***Figure 17B***). This significant improvement in early survival could be attributed to an overall "normalization" of Hif signaling, leading to a combined improvement in erythrocytosis, blood volume, vascular bed and cardiac function.

We used a zebrafish model for VHL disease to provide compelling evidence that pharmacologic targeting of HIF2α can treat VHL phenotypes, and to validate the presented HIF2α inhibitors as promising lead compounds for treatment of VHL disease.

4.3. Discussion

Patients with VHL disease develop clear cell RCC, hemangioblastomas (HB) of the CNS including the retina, erythrocytosis, pancreatic neuroendocrine tumors and pheochromocytomas. The current treatment of the disease is based on repeated surgeries that may result in renal insufficiency or severe neurologic deficits [1]. Medical therapy with VEGF inhibitors has a modest, at best, effect on RCC lesions only. Published reports indicated a partial response of metastatic or locally advanced RCC in VHL patients [219–222]. No medical therapy for HB exists so far; there has been no evidence of HB response to VEGF inhibitors in the VHL patients treated for RCC. Experiments in xenograft or genetically engineered animal models of VHL disease strongly suggest that HIF2α is a critical therapeutic target for VHL-deficient tumors [119,121,202]. Here we used specific HIF2α small molecule inhibitors to treat the phenotypes linked to loss-of-VHL function in the best available model for the human disease, the *vhl* mutant zebrafish embryo [162,163]. There are many pharmacologic differences between clinically administering a compound to higher vertebrates and testing its in vivo efficacy by adding it to the medium used in the zebrafish colony. Nevertheless, testing a compound in zebrafish models controls for acute and obvious toxicities and provides evidence of efficacy in a vertebrate model that resembles VHL disease. This is why zebrafish has been regarded as a great model organism for chemical screens, leading to discovery of clinically promising compounds [223].

Our work presents for the first time a paradigm of pharmacological treatment of VHL phenotypes in a vertebrate animal model. The HIF2α inhibitors we used (compounds 76 and 77) are non-optimized hits from a cell-based screen [205]. Their mode of action consists of enhancing the binding of IRP1 to the 5'-UTR of *HIF2α* and therefore suppressing HIF2α translation. It is quite remarkable that even without further chemical optimization these inhibitors display

promising activity in vivo and they have the ability to partially reverse the VHL phenotype of a zebrafish model of VHL disease. We are currently using medicinal chemistry to modify these compounds, based on structure-activity analysis, with the goal of developing derivatives suitable for pre-clinical and clinical testing.

Targeting transcription factors has been regarded as a challenging problem in drug development. Early attempts to interfere with protein-DNA interactions failed and only recent approaches utilizing stapled peptides appear promising in directly interfering with transcriptional activity [224]. The clinical applicability and efficacy of the stapled peptide approach remain to be tested. Pharmacologic inhibition of the interaction between transcription factors and their cognate co-activators or histone modifiers appears promising [225]. The HIF2α inhibitors that we discovered function by specifically repressing the translation of this transcription factor. To the best of our knowledge, the only other available small molecule with specific HIF2α inhibitor activity employs a different mode of action; it disrupts HIF2α-ARNT heterodimerization [226]. No data on the efficacy of this compound in vivo has been published. It is conceivable that multiple inhibitors of HIF2α, with different mechanisms of action, can be combined for treatment of VHL disease.

The inhibitors used in the current study not only suppress HIF signaling biochemically at a potency which is reasonable for hit compounds (10nM – 1μM) but they also induce changes in the physiology of the *vhl* phenotype: they significantly inhibit erythrocytosis, trim vessel expansion, improve cardiac contractility and promote survival. Erythrocytosis and vascular proliferation are established outcomes of the transcriptional activity of HIF2α [83,202,227]. On the other hand, the mechanisms leading to cardiac dysfunction and embryo death are likely complex and have not yet been elucidated. A direct link between HIF2α activity and cardiomyocyte

physiology has been postulated [228]. In addition, a recent study showed that HIF2α activation in IRP1 knockout mice stimulates erythropoietin and endothelin-1 and promotes pulmonary hypertension in the animals [208]. Endothelin-1 is a potent vasoconstrictor peptide, which is released by endothelial cells in conditions of hypertension, myocardial infarction and congestive heart failure [229,230]. The expression of endothelin-1 promotes low fractional shortening of the left ventricle of hypertensive mice. These data implicate the HIF-driven gene endothelin-1 in cardiac failure [231]. It is possible that zebrafish endothelin-1 is upregulated in *vhl*$^{-/-}$ embryos cardiomyocytes, leading to impaired ventricular function. Treatment with HIF2α inhibitors promptly improved cardiac ventricular function in *vhl*$^{-/-}$ embryos. It was previously proposed that *vhl*$^{-/-}$ embryos die due to cardiac failure [162]. Therefore the improvement of ventricular function and the potential delay of cardiac failure may explain the effect of HIF2α inhibitors on *vhl*$^{-/-}$ embryo viability during early larval stages.

Inhibition of HIF2α led to a significant decrease in the Fli1-GFP driven fluorescence of the CHT, a highly vascular plexus with rapid proliferation of hematopoietic stem cells (HSC) [218]. *Vhl*$^{-/-}$ embryos exhibit an increase in c-myb^{+} hematopoietic stem cells (HSC) in the CHT [162] and Fli1 promoter marks macrophages and myeloid cells in addition to vascular endothelial cells [217]. HIF directly transactivates transcription factors that promote “stemness” [104] and HIF2α has been reported as necessary for maintenance of glioblastoma stem cells [118]. Therefore, it is conceivable that HIF2α inhibition leads to a combined suppression of both the vascular and the HSC component of CHT. It is possible that the complex vascular and hematopoietic CHT compartment of the zebrafish mimics the microenvironment that promotes the development of brain stem hemangioblastomas. If this is the case, the *vhl*$^{-/-}$ embryo will provide an attractive model to screen for inhibitors of the VHL-related hemangioblastoma disease, in addition to the HIF2α inhibitors we present here.

4.4. Supplemental data

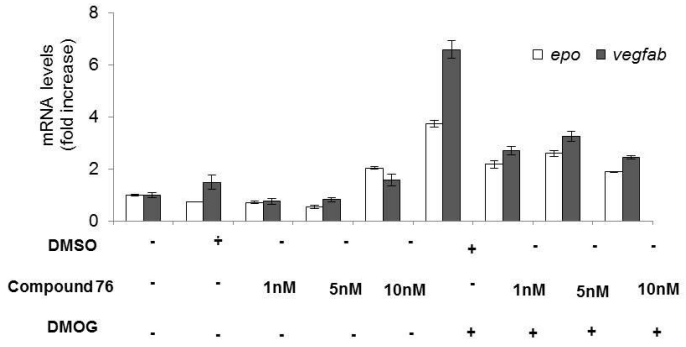

Figure S2: Small molecule compound 76 suppresses DMOG-induced expression of HIF2α-target genes in wild type zebrafish embryos. mRNA expression of the HIF-target genes *epo* and *vegfab* in wild type embryos challenged with 100µM of DMOG and treated with compound 76 (as indicated) or vehicle only control. Gene expression levels were normalized by *18S* gene expression. All experiments were performed in biological triplicates. Data represents mean ± SEM.

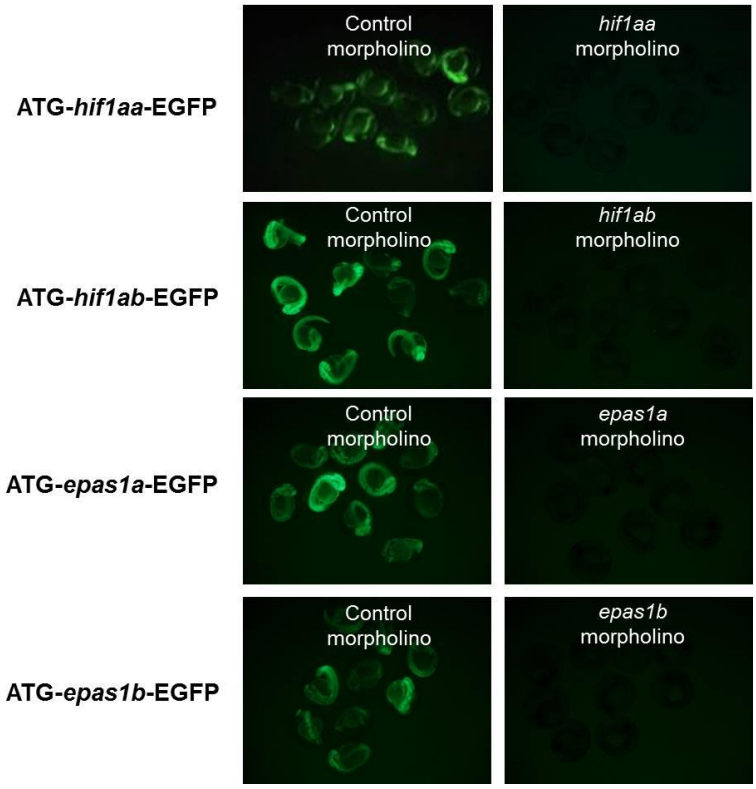

Figure S3: Inhibition of *HIF1αa, HIF1αb, epas1a* and *epas1b* translation by morpholinos is specific for the cognate paralog. Single-cell embryos were injected with the indicated morpholino combined with the morpholino target sequence upstream of EGFP mRNA (indicated on the left side of each figure). A scrambled morpholino was used as control. Each morpholino inhibited the translation of the cognate only paralog but not the translation of the non-targeting paralogs.

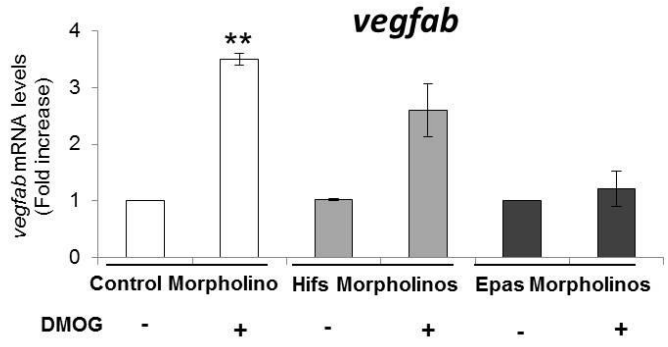

Figure S4: *Epas1a* and *epas1b* are the main paralogs transactivating Vascular Endothelial Growth Factor ab (*vegfab*). Changes in DMOG-induced expression of *vegfab* in *wt* embryos injected with control morpholino, *HIF1αa* and *HIF1αb* combined morpholinos (hifs morpholinos) or *epas1a* and *epas1b* combined morpholinos (epas morpholinos) and treated with DMOG from 3dpf to 4dpf. Gene expression levels were obtained by qRT-PCR and normalized to the expression of *18S*. All experiments were performed in biological triplicates. Data represents mean ± SEM. Unpaired, two-tailed *t* test was used for statistical analysis. ** $p<0.01$

Figure S5: The sequences of the *HIF1ab* and *epas1b* knock-out mutations. Exon sequences are in upper case letters, whereas intron sequences are in lower case letters. The dashes indicate the deletions in the mutant allele. *wt*, wild-type; mt, mutant. The numbers on top of the sequences indicate the number of the nucleotide in its coding sequence.

CHAPTER 5

Establishment of Hemangioblastoma cell lines and an orthotopic mouse model

5.1. Scientific Background

Hemangioblastomas (HBs) are benign tumors from the Central Nervous System (CNS) that develop sporadically or in association with the hereditary VHL disease [1]. These tumors are characterized by a strong endothelial component that forms a leaky network of blood vessels around the tumor cells (called HB *stromal* cells). CNS HBs are diagnosed by an intense uptake of contrast agents and a consequent bright signal in T1-weighted MRI [232].

The histological diagnosis of CNS HB tumor cells is difficult considering several factors: the heterogeneity of these tumors, the unclear origin of the tumor *stromal* cells and the few molecular markers that are consistently expressed across individual HBs. The main marker used to identify HB tumor *stromal* cells and to distinguish HBs from other brain metastasis is podoplanin (PDPN) [37]. PDPN (which is also known as D240, T1a, E11 antigen and gp38) has initially been studied as an important protein involved in the embryonic development of the lymphatic and vascular systems, the heart, the lungs and the brain [38,233,234]. Although it is widely used as a marker of lymphatic endothelial cells [235,236], this protein is also present in other cell types such as fibroblastic reticular cells of the lymph nodes [237], alveolar type I cells [238], macrophages and specific subsets of T cells [239–241]. PDPN function relates to its heavily glycosylated extracellular domain that binds to the receptor CLEC-2 to promote the aggregation of platelets or other cell types, maintaining the integrity of vascular vessels. In the developing brain, PDPN is expressed in neuro-epithelial cells and allows the recruitment of pericytes to the emerging endothelium, sustaining the integrity of the cerebrovascular structure [234]. Interestingly, PDPN is highly expressed in brain tumors [242,243], as well as skin cancers [244], osteosarcomas [245], squamous cell carcinomas [246], malignant mesotheliomas [247,248] and cancer-associated fibroblasts[249]. The role and molecular function of PDPN in CNS HB biology is unknown.

In addition to HB *stromal* cells, these benign brain tumors are characterized by a rich tumor microenvironment with the presence of endothelial cells, pericytes and different hematopoietic cells (including red blood cells and mast cells) [10–12]. The relationship and interaction between these microenvironmental cells and the tumor *stromal* cells is thought to be important but not well understood. While some studies proposed that tumor *stromal* cells could differentiate into endothelial and hematopoietic progenitors [6,11], our previous data showed that only a small percentage of the cells within the tumor mass harbor the somatic *VHL* mutation and therefore most of the tumor mass is formed by reactive normal endothelial and hematopoietic cells from the microenvironment. Nevertheless, they represent an important component of CNS HB biology and should be studied as part of these heterogeneous and complex tumors.

An important feature of CNS HBs, similarly to other VHL-associated tumors, is the activation of the HIF signaling pathway. After loss of the tumor suppressor gene *VHL*, the HB tumor cells stabilize HIF1α and HIF2α transcription factors and upregulate a large group of HIF downstream targets genes involved in angiogenesis (*VEGFA*, *PDGFB*), erythropoiesis (*EPO*) and metabolism (*GLUT1*, *PLIN2*) [77]. The activation of the HIF signaling pathway promotes the strong angiogenic phenotype of CNS HBs (with the release of high levels of VEGFα), and the abnormal lipid metabolism with extensive accumulation of cytoplasmic lipid droplets [91,123]. These phenotypes are not only characteristic of CNS HBs but they also occur in other VHL-negative tumors, such as ccRCCs [52,92].

As rare and benign tumors of the CNS, HBs are not deeply studied. In fact, with no cell lines or mouse models recapitulating the disease, there is a lack of scientific resources that greatly compromises the research in the field. With this work we aimed to establish long-term HB-derived cell lines from CNS HB fresh tumors. These cell populations express markers of HB tumor cells (such as PDPN, VEGFα and HIF) and can be used to study the biology of human

CNS HBs *in vitro*. Additionally, through orthotopic injection of HB-derived cells we established, for the first time, a mouse model to study CNS HBs. These brain tumors are highly angiogenic, uptake gadolinium-based contrast agents and accumulate large amounts of intracellular lipids, recapitulating the human CNS HBs. Therefore, they represent a faithful model of the human disease and should be used in the future for the development of new therapeutic drugs and strategies for the treatment of CNS HBs.

5.2. Experimental Results

Establishment of CNS Hemangioblastoma-derived cell lines from human fresh tumors

In order to establish primary and stable cell lines from fresh CNS Hemangioblastomas we collected different HB specimens from the Neurosurgery Department at Massachusetts General Hospital in Boston. The first specimen was collected from a VHL-associated HB tumor that developed in the cerebellum of the patient (designated AM1 tumor). The tissue was quickly processed and incubated using two different methods and medium conditions: a) *ACL4*, which is a rich medium with epithelial growth factor (EGF) that promotes cell growth without immortalizing the cells, and b) the *Schlegel's Method*, which is used to grow normal and tumor cells conditioned with TCM medium in the presence of ROCK inhibitor and a monolayer of irradiated fibroblasts [175] (***Figure 18C***).

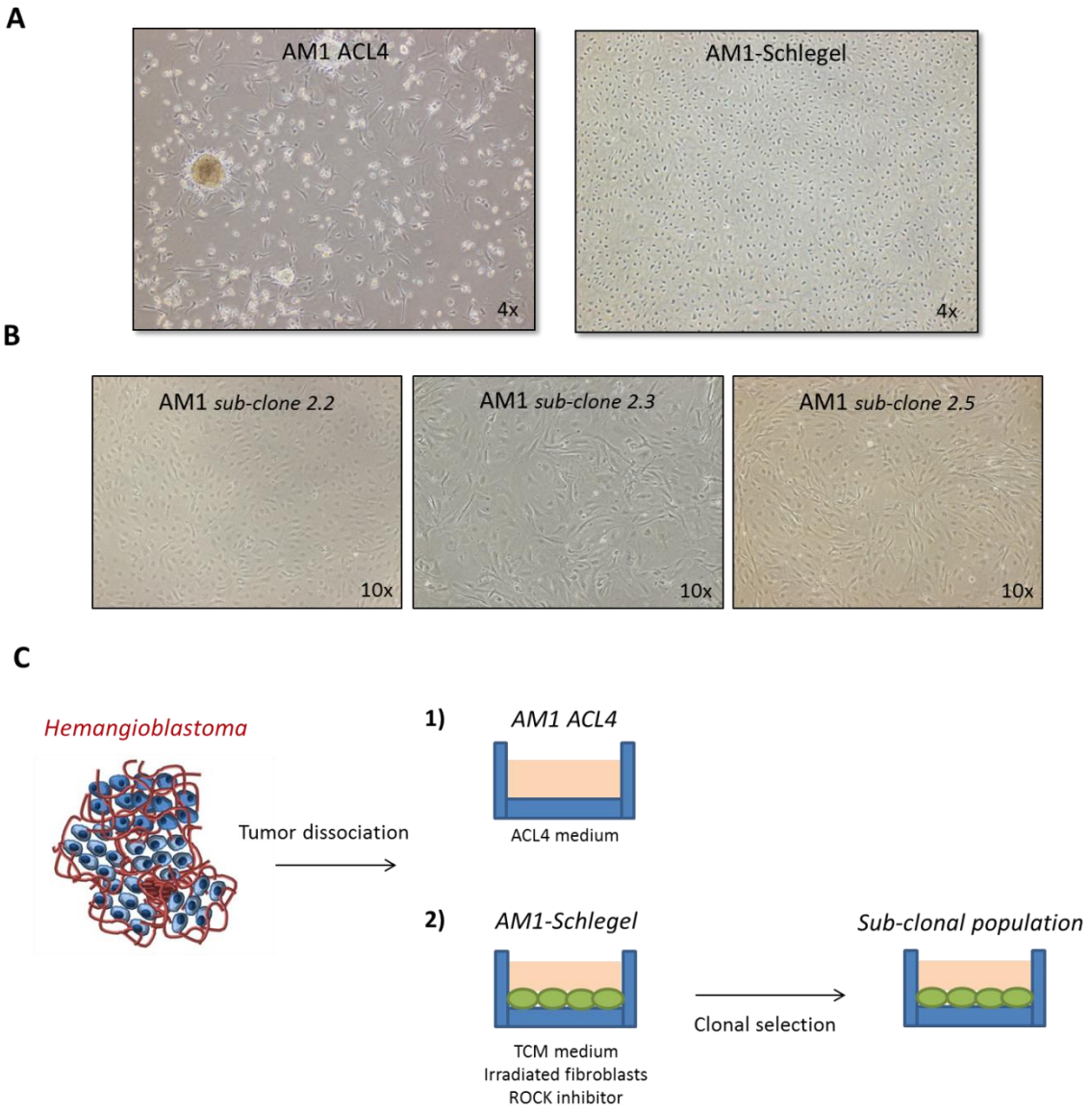

Figure 18 – Establishment of Hemangioblastoma-derived cell lines from fresh human tumors. A) Microscope images of polyclonal populations *AM1 ACL4* and *AM1-Schlegel* both established from the same VHL-associated tumor (AM1). **(B)** Representative images of different sub-clones with heterogeneous morphology isolated from the *AM1-Schlegel* polyclonal population. **(C)** Scheme representing two distinct methods used, after tumor dissociation, to maintain cell growth *in vitro*: **(C1)** ACL4 - a rich medium with epithelial growth factor (EGF) or **(C2)** the Schlegel's method - a rich medium (TCM) in the presence of ROCK inhibitor and a monolayer of irradiated fibroblasts (depicted in green).

After several weeks, polyclonal and heterogeneous populations of cells started to grow in both plates. The HB-derived cells exposed to ACL4 medium started growing fast and consistently, forming nice and bright spheres that released elongated cells (***Figure 18A, left***

panel). In contrast, the cells processed using the Schlegel's method grew at a slower rate and were formed by a continuous sheet of small cells as seen in ***Figure 18A, right panel***. The establishment of sub-clones from distinct cell types revealed the heterogeneous morphology of cells existing within the same polyclonal population (***Figure 18B***).

CNS HBs are heterogeneous tumors formed by presumed tumor cells (called *stromal* cells), endothelial cells, pericytes and hematopoietic cells. In order to better characterize the HB heterogeneity we isolated single-cells from both AM1 lines, using FACS sorting, and established monoclonal populations derived from individual cell lineages. Despite the initial cell division, these single-cell clones were not able to sustain growth to form an independent line. We then used cell culture cloning rings to isolate sub-clones of distinct morphology that were growing individually in the *AM1 Schlegel* population. Once again, the isolated sub-clones of individual cell lineage were not able to proliferate and started to senesce after the first passages. In contrast, the initial polyclonal and heterogeneous populations of both *AM1 ACL4* and *AM1 Schlegel* grew consistently and healthy up to three months. This result shows that different cellular entities, even if present in small fractions, are necessary to sustain the growth of HB-derived cells *in vitro*, possibly due to the existence of fundamental paracrine signaling pathways and different cell-to-cell interactions characteristic of HB biology.

HB-derived cells express markers of CNS Hemangioblastomas

The two main cellular lineages present in HB tumors are tumor *stromal* cells and endothelial cells, with some HBs also having a strong hematopoietic component (***Image 19A***). In order to identify the main lineage present in *AM1 ACL4*-derived cells, we analyzed the expression of the HB *stromal* cell marker podoplanin (PDPN) and the endothelial marker CD31

by FACS. For the characterization analysis we decided to use *AM1 ACL4* cells only considering their fast growing pattern. The osteosarcoma cell line U2OS and the endothelial cell line HUVEC were used as positive controls for the expression of PDPN and CD31, respectively. Surprisingly, we discovered that 91.7 ± 6.4% of the *AM1 ACL4* cells express PDPN, which is a clinical marker used in the diagnosis of HB *stromal* cells [37] (***Image 19B***). In contrast, *AM1 ACL4* cells do not express CD31, confirming that they are not endothelial cells. This is an important result for two reasons: first, endothelial cells are known to constitute a big fraction of the HB microenvironment and could dominate the HB-derived populations. Secondly, PDPN is a marker of not only HB *stromal* cells but also lymphatic endothelial cells, which are known to express specifically PDPN but also the pan-vascular endothelial marker CD31 [250]. Our data shows that there is no co-expression of PDPN and CD31 in the HB cultured cells, and therefore, the HB-derived cells are not endothelial or lymphatic endothelial cells. Instead, they highly express one of the main markers used to identify HB *stromal* cells.

We then used a second tumor specimen from a sporadic HB tumor to establish the *AM2 ACL4* line using the ACL4 method. Similarly to the *AM1*-derived population, 87.1 ± 4.8 % of *AM2 ACL4* cells express PDPN without expressing CD31 (***Figure 19C***), demonstrating that the ACL4 medium promotes the growth of $PDPN^+$ cells and specifically enriches for this population within the HB microenvironment.

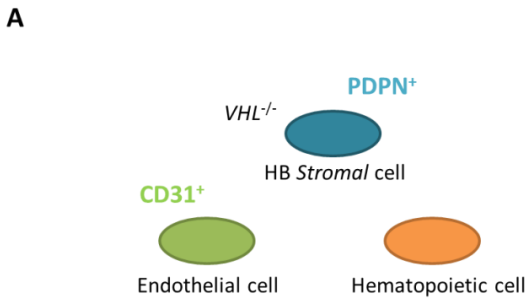

C

Cellular markers	AM1	AM2
PDPN	91.7 ± 6.4 %	87.1 ± 4.8 %
CD31	-	-
VEGFR2	-	1.0 ± 0.4 %
CXCR4	-	1.7 ± 0.7 %
VE-Cadherin	-	0.3 ± 0.2 %
CD133	-	-
CD11b	0.6 ± 0.1 %	-
CD45	17.1 ± 4.3 %	-

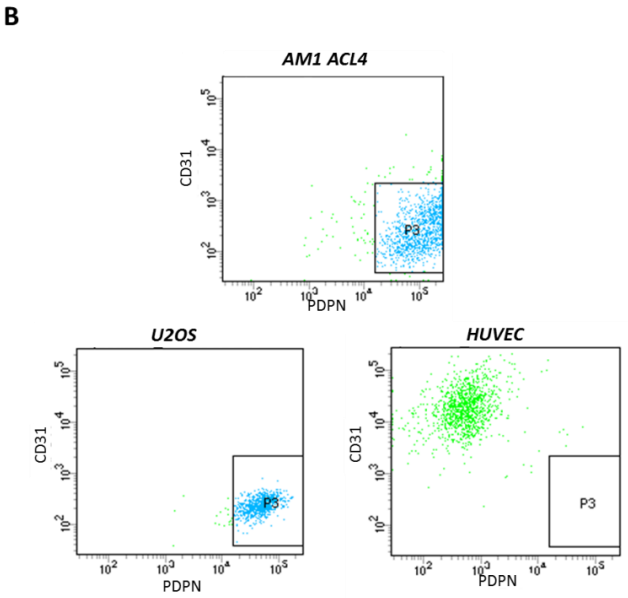

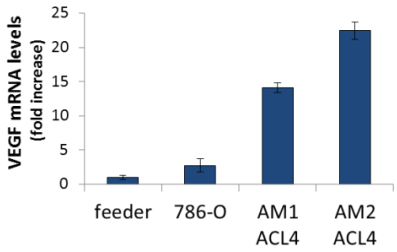

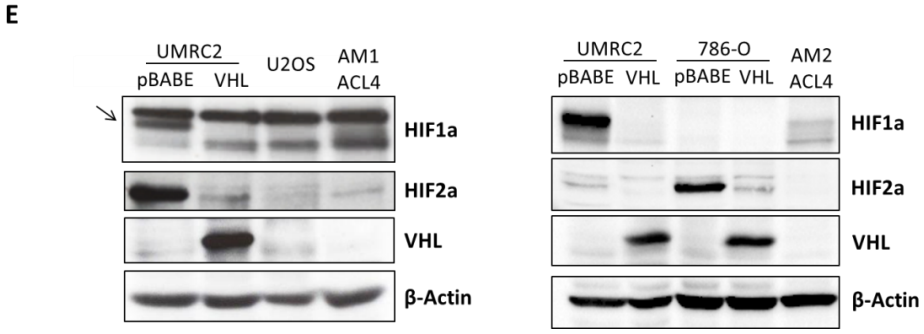

Figure 19 - HB-derived cells express podoplanin (PDPN) and other markers of human HB tumors. (A) Representative scheme of HB cellular heterogeneity and the main cell markers used to identify the stromal cells and the endothelial cells. **B)** Expression of the HB marker PDPN and the endothelial marker CD31 in *AM1 ACL4* line by FACS analysis. U2OS and HUVEC cell lines were used as positive controls of PDPN and CD31 expression, respectively. **(C)** Percentage of cells from *AM1 ACL4* and *AM2 ACL4* expressing the cell-specific markers: PDPN, CD31, VEGFR2, CXCR4, VE-Cadherin, CD133, CD11b and CD45. **(D)** mRNA levels of the bona-fide HIF target gene *VEGFA*, assessed by qRTPCR and normalized to *28S* mRNA levels. Feeder cells (irradiated fibroblasts) were used as negative control and 786-O as positive control. **(E)** Protein levels of the transcription factors HIF1α and HIF2α and the tumor suppressor VHL in *AM1 ACL4* and *AM2 ACL4* cells. The VHL-negative RCC cell lines UMRC2 pBABE and 786-O pBABE were used as positive controls of HIF1α and HIF2α expression (pBABE), and their isogenic pairs with reconstituted VHL protein as negative controls. U2OS is an osteosarcoma cell line used as negative control. β-Actin was used as internal control.

In order to further evaluate the HB-derived cells, we used a panel of cell surface markers specific for: hemangioblasts and endothelial precursor cells (VEGFR2, VE-Cadherin), hematopoietic stem cells and neural stem cells (CXCR4, CD133), microglia (CD11b), macrophages and other immune cells (CD45). We compared the VHL-associated HB line (*AM1 ACL4*) with the sporadic HB-derived line (*AM2 ACL4*) regarding the expression of these cell markers (***Figure 19C***). Interestingly, in the *AM1 ACL4* polyclonal population we identified a significant presence of $CD45^+$ immune cells (17.1 ± 4.3%), possibly macrophages or mast cells, and few $CD11b^+$ microglial cells (0.6 ± 0.1%). On the other hand, while no immune cells were detected in the *AM2 ACL4* line, a small percentage of cells expressed VEGFR2 (1.0 ± 0.4%), CXCR4 (1.7 ± 0.7%) and VE-Cadherin (0.3 ± 0.2%), representing progenitor endothelial cells from the tumor microenvironment. Moreover, and in contrast to IHC studies in human HBs [33,34], we did not detect $CD133^+$ cells in any of the HB-derived lines. In summary, although hematopoietic and endothelial cells were detected in the HB-derived cell populations their presence decreased over time. The main cellular component of these HB-derived cells is represented by $PDPN^+$ cells that seem to be enriched by the specific cultured conditions.

A classic feature of CNS HBs is the activation of the HIF signaling pathway. We confirmed that the *AM1 ACL4* and *AM2 ACL4* cells express high levels of the bona-fide HIF target *VEGFA*, even compared to the VHL-negative ccRCC cell line 786-O, as assessed by qRTPCR (***Figure 19D***). *VEGFA* is a bona-fide HIF target gene involved in angiogenesis and known to accumulate in CNS HBs, therefore the high levels of *VEGFA* mRNA detected in these cells are the first indication of an active HIF signaling in the *AM1 ACL4* and *AM2 ACL4* cells. To further corroborate this result, we detected the protein levels of the transcription factors HIF1α and HIF2α in *AM1 ACL4* and *AM2 ACL4*, by western-blotting (***Figure 19E***). The osteosarcoma cell line U2OS and the ccRCC cell lines UMRC2 and 786-O were used as negative

and positive controls of HIF1α and HIF2α expression, respectively. The VHL-negative cells UMRC2 (pBABE) and 786-O (pBABE) were reconstituted with the functional VHL protein (VHL) to validate the HIF1α and HIF2α protein bands. ***Figure 19E*** shows that while *AM1 ACL4* cells express low levels HIF2α, *AM2 ACL4* cells express HIF1α only. Interestingly and in both cases, ccRCC cells express higher levels of HIFs than HB-derived cells, which can indicate a distinct biology between these two tumor types.

HB-derived cells grow brain tumors in vivo

The only animal model available to study VHL disease and CNS HB biology is the *vhl*$^{-/-}$ zebrafish embryo that develops hypervascularization in the brain and retina, mimicking HB formation [162,163]. Although this represents a good model to study anti-angiogenic mechanisms and to perform drug screenings, it does not fully and faithfully recapitulate the development and growth of human CNS HBs. Therefore, in an attempt to develop a mouse model and to confirm the tumorigenesis of the HB-derived cell lines, we injected *AM1 ACL4* and *AM2 ACL4* cells orthotopically into the right caudate of the brain of immunocompromised NOD/SCID mice. Twelve days after injection of *AM1 ACL4* cells, a small and bright mass was visible in the right brain hemisphere of the first NOD/SCID mouse injected (***Figure 20A,*** *upper left panel*). This small mass grew over time (***Figure 20A,*** *upper right panel*), evolving into a big and heterogeneous mass visible by T2-weighted MRI (***Figure 20A,*** *bottom left panel*). At Day 19 after injection, the *AM1 ACL4*-derived brain tumor was strongly highlighted in a contrast-enhanced T1-weighted MRI, characteristic of human CNS HBs (***Figure 20A,*** *bottom right panel*).

In order to compare VHL-associated HB cells and sporadic HB cells, we calculated the tumor volume over time for *AM1 ACL4* versus *AM2 ACL4*-derived tumors (n=7). While both cell populations formed brain tumors in NOD/SCID mice at a similar rate and with a 100% incidence, the *AM2 ACL4*-tumors grow significantly faster *in vivo* (***Figure 20B***).

The histological comparison of *AM1 ACL4* and *AM2 ACL4*-derived tumors with normal brain tissue by H&E staining shows that the tumor regions are formed by clusters of tightly packed cells very distinct from the distant nuclei seen in the mouse brain parenchyma (***Figure 20C,*** *top panels*). In addition, the presence of an extensive network of blood vessels and a rich hematopoietic compartment (with red blood cells and other immune cells filling the blood vessels) in the *AM1 ACL4* and *AM2 ACL4*-derived tumors faithfully mimics the histology of the human HB tumors (***Figure 20C,*** *bottom panels*). Therefore, and surprisingly, the injection of these HB-derived polyclonal populations in mice recapitulates the cellular heterogeneity seen in the human HB disease. These brain tumors develop within 12 days and can be followed and studied until the tumor volume achieves a maximum limit size (usually up to 20 days). Interestingly, *AM1 ACL4* and *AM2 ACL4* lines derived from two biologically distinct cases (one VHL-associated and one sporadic HB) are both able to form tumors *in vivo* that develop at a similar rate. These characteristics (that might be intrinsic to the biology of each specific CNS HBs) encourage the use of this method in other HB tumors in order to enhance the mouse model repertoire.

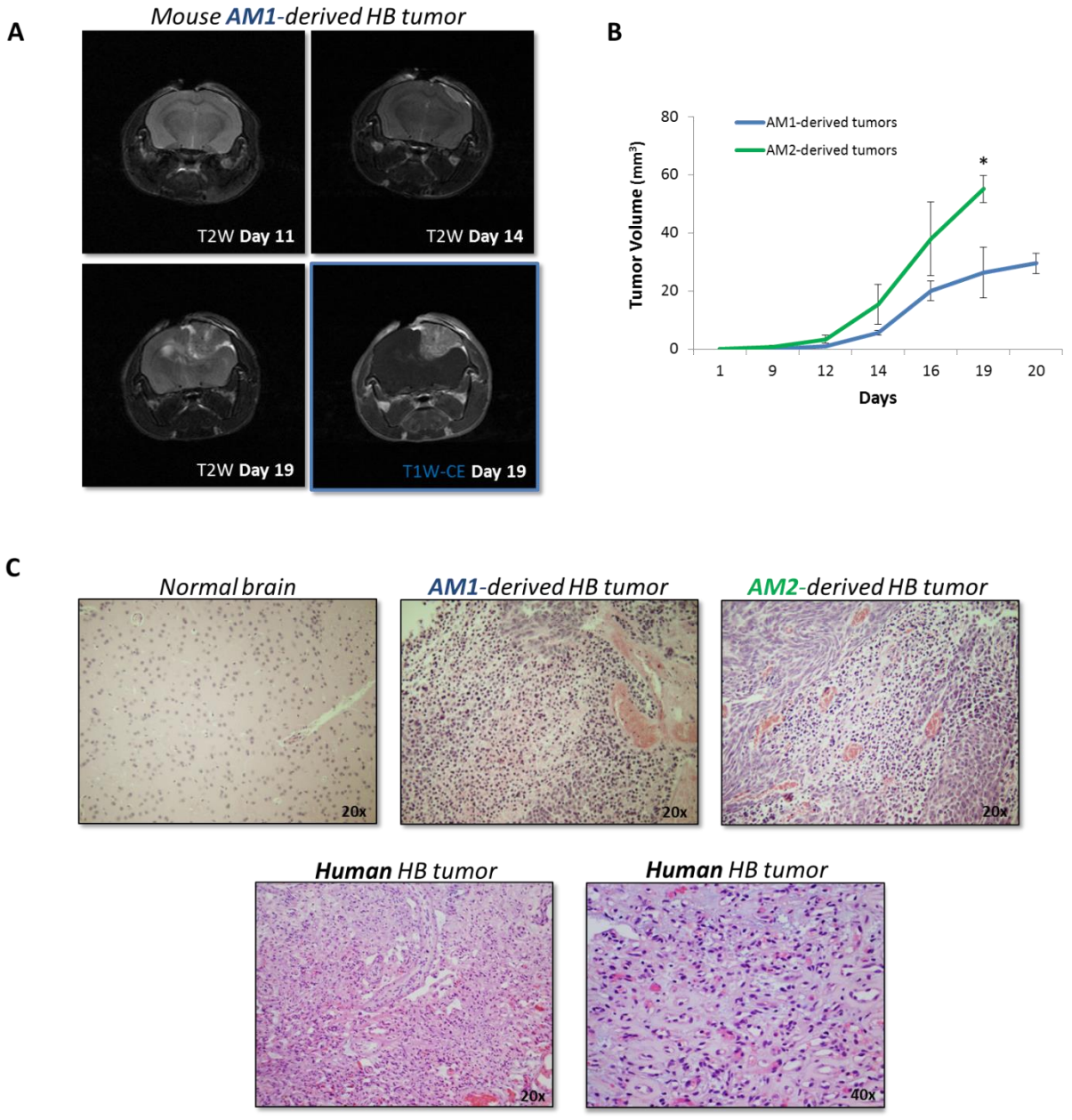

Figure 20 - HB-derived cells form tumors *in vivo* and recapitulate the histology of human HB tumors. A) MRI images of the brain of immunocompromised NOD/SCID mice after orthotopic injection with *AM1 ACL4* cells. At Day 11 after injection, a small mass starts to form in the brain of the mice. The tumor grows and forms a large heterogeneous mass that is well circumscribed, characteristic of a benign tumor. At Day 19, the tumor shows a strong enhanced-T1 weighted signal after injection of a gadolinium-based contrast agent, mimicking the clinical profile of human HB tumors. **B)** Tumor volume of both AM1 and AM2-derived tumors (VHL-associated and sporadic HBs, respectively) over a period of 20 days after the orthotopic injection. **C)** H&E staining of AM1 and AM2-derived brain tumors shows an abnormal proliferation of tumor cells with a rich network of blood vessels filled with red blood cells, which is significantly different from the histology of a normal mouse brain. AM1 and AM2-derived tumors recapitulate the histology of human HB tumors shown in the lower panel. The animals studies were performed in AM1 and AM2-derived HBs (n=7 per group). Data represents mean ± SEM. Unpaired, two-tailed *t* test was used for statistical analysis. * $p<0.05$.

AM1 and AM2-derived tumors are rich in intracellular lipids and highly vascularized

CNS HBs as VHL-negative tumors are rich in cytoplasmic lipid droplets [91]. The abnormal lipid metabolism caused by HIF signaling activation promotes the accumulation of triglycerides that are stored in the cell cytoplasm in the form of lipid vesicles [92,94]. In order to detect the presence of intracellular lipids within the tumor *in vivo*, we selected a volumetric region of interest (*white box*, ***Figure 21A***) to acquire a ^{1}H MRS spectrum within the tumor. As control, we used a region of normal brain on the left side of the cerebrum from the same animal. ***Figure 21B*** shows the comparison between representative ^{1}H MRS spectra of a normal brain and a HB-derived tumor. The mobile lipids (in contrast to the immobilized lipids of the cellular membrane) are detected by ^{1}H MRS at approximately 0.9 and 1.3ppm, which correspond to methyl (CH_3) and methylene $(CH_2)_n$ groups, respectively [251]. As seen in the figure, two clear peaks at approximately those frequencies are detected in the *AM1 ACL4*-derived tumor but not in the normal mouse brain, indicating the presence of lipid droplets within the tumor mass. In order to quantify the intracellular lipid content and compare *AM1 ACL4* and *AM2 ACL4*-derived tumors, we calculated the ratio between lipids (lip13a+lip13b, at 1.3ppm) and normalized to the internal control metabolites creatinine and phosphocreatine (Cr+PCr). As shown in ***Figure 21C***, both *AM1 ACL4* and *AM2 ACL4*-derived tumors have a Lip/Cr+PCr ratio higher than 1, which clearly shows the high concentration of these molecules among other intracellular metabolites.

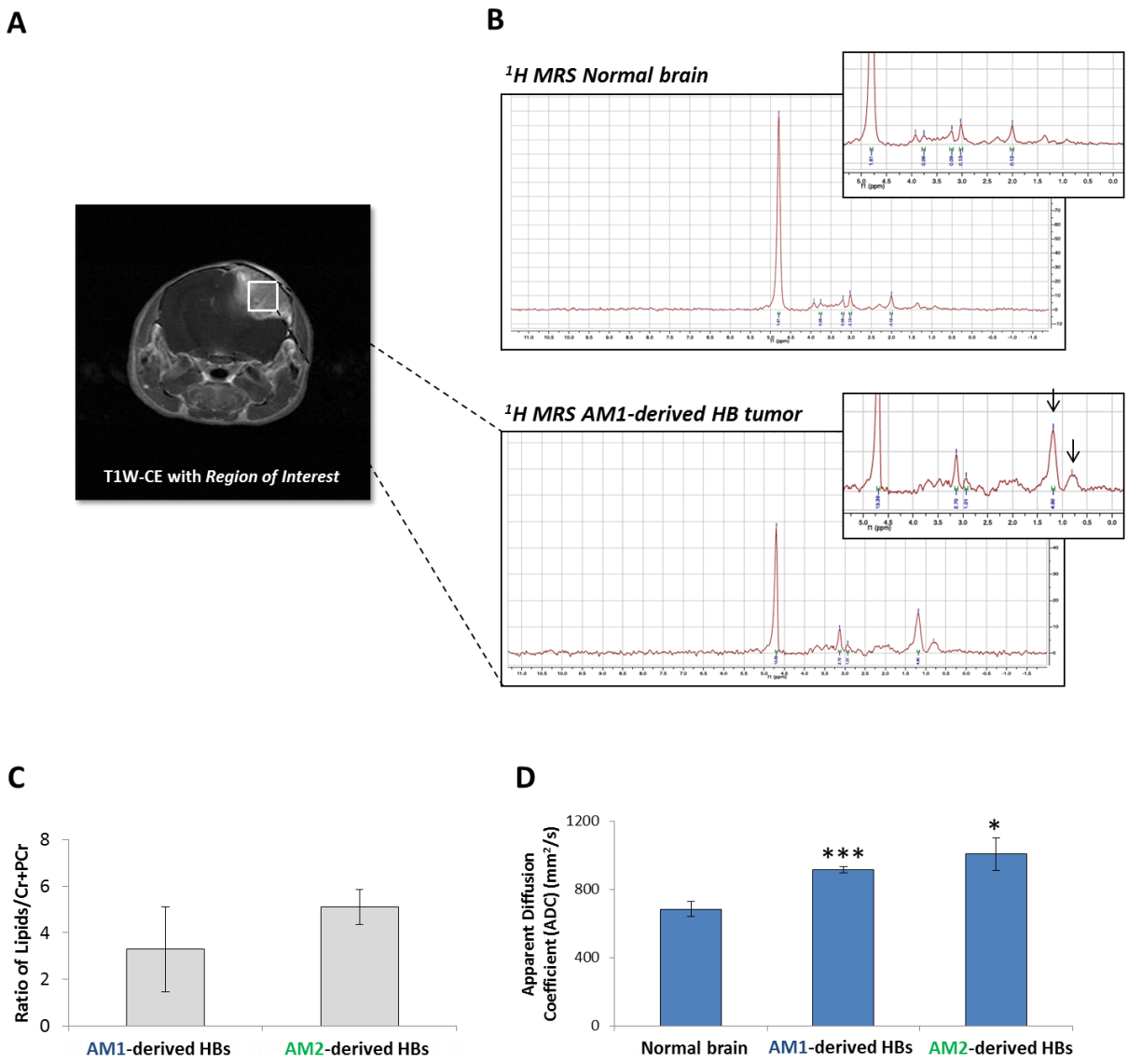

Figure 21 - HB-derived tumors are characterized by high lipid content and intense vascularization. A) Contrast enhanced T1-weighted MRI image (T1W-CE) of a representative AM1-derived tumor with the selected vortex within the tumor area (region of interest) in white. **B)** *In vivo* ^{1}H MRS spectra of the AM1-derived tumor compared to the normal cerebrum. The black arrows point to the ppm region of lipids, highly present within the AM1-derived HB tumor and absent in the normal brain. **C)** Quantification of intracellular lipids (Lipids 1.3ppm/Cre+PCre ratio) present in AM1 and AM2-derived HB tumors based on *in vivo* ^{1}H MRS spectra. **D)** Apparent Diffusion Coefficient (ADC) of AM1 and AM2-derived HB tumors compared to normal cerebrum, calculated using diffusion-weighted imaging. ADC is a diffusion coefficient that increases proportionally with the presence of blood vessels, necrosis or tumor edema. The animals studies were performed in AM1-derived HBs (n=6) and AM2-derived HBs (n=8). Data represents mean ± SEM. Unpaired, two-tailed *t* test was used for statistical analysis. * $p<0.05$; *** $p<0.001$

Finally, in order to characterize the tumor microenvironment, we used diffusion-weighted imaging (DWI) and calculated the Apparent Diffusion Coefficient (ADC) *in vivo*. ADC measures the movement of H_2O molecules within a specific region. This value is higher in the presence of angiogenesis and rich vascular systems, tumor necrosis or edema [252]. By comparing normal brain regions *versus* tumor tissue we detected a significantly higher ADC value in *AM1 ACL4* and *AM2 ACL4*-derived tumors (***Figure 21D***). This increase is statistically significant for both groups of tumors compared to normal brain and indicates an enhanced vascularization present within these tumors. In this experiment only one mouse (out of 14) developed necrosis within the tumor and none of them showed edema. Therefore this high ADC value is attributed to a highly angiogenic tumor profile that faithfully recapitulates the human CNS HB disease *in vivo* [253].

5.3. Discussion

CNS Hemangioblastomas are benign tumors formed by distinct and heterogeneous cell populations [10]. The current state of art to study CNS HBs is extremely scarce and the only scientific resource available to study the disease is the zebrafish *vhl* model that recapitulates some but not all the VHL phenotypes. The *vhl* zebrafish embryo develops abnormal vascularization in the brain and in the retina, which might mimic the HB formation process [162,163,254]. However, and probably due to a short live span, these embryos rarely develop full HB tumors. In addition to this animal model, there are no cell lines or other animal models established to study the HB disease. The methods previously described to grow HB cells *in vitro* were used for short-term cultures [6,255]. With this work, we aimed to establish long-term cell cultures from fresh HB tumors. We compared two distinct methods: primary cultures grown in a rich ACL4 medium *versus* the *Schlegel's Method* that uses a mild immortalization process [175]. The *Schlegel's Method* was initially developed for epithelial cells but it can also be used in other cell lineages, including brain tissue. We initially selected this method considering that it is a mild method of unlimited cell growth (by increasing telomerase expression) and that sustains the proliferation of both normal and tumor cells, which would be helpful to maintain the intratumoral heterogeneity seen in human CNS HBs. However, while the cells processed through the *Schlegel's Method* grew very slowly, the ACL4 primary cultures formed nice and bright spheres that proliferated consistently into elongated cells. Therefore, we selected the ACL4 method, which was successfully used for long periods of culture (up to 3 months). In addition, it promotes the proliferation of $PDPN^+$ cells and maintains some HB heterogeneity without transforming the cells. Moreover, the establishment of HB-derived cells from independent HB fresh tumors (both VHL-associated and sporadic) indicates that this is a reliable method to grow

HB-derived cells. Alternative methods to grow these cells and establish cell lines would be the immortalization with viral oncogenes such as SV40 large T antigen or the introduction of exogenous human telomerase reverse transcriptase (hTERT) [256,257].

The molecular identification and heterogeneity of CNS HB tumors is a topic of avid debate. The unknown origin of the tumor *stromal* cells impairs their clear identification, being PDPN the current molecular marker used to distinguish HB tumor cells from other brain metastasis [37]. In this study we confirmed that the majority of the HB-derived cells express high levels of PDPN, indicating that they might be HB *stromal* cells. Additionally, PDPN can also be expressed in macrophages and normal lymphatic endothelial cells [38]. We therefore confirmed that the majority of the $PDPN^+$ cells were not lymphatic endothelial cells because they did not co-express the pan-vascular endothelial marker CD31. Interestingly, the isolation of single-cells or sub-clones from the parental polyclonal populations failed to grow *in vitro*. This result indicates that different cell populations present in the tumor microenvironment, independently of their fraction within the tumor, are fundamental for the growth of the tumor cells. This might be caused by direct cell-to-cell contact and/or paracrine oncogenic signaling pathways that are known to be active in CNS HBs, such as EPO/EPOR, VEGFα/VEGFR2, PDGFβ/PDGFβR and SDF-1/CXCR4 [11,123–126]. The identification of these different cells present within the HB tumor microenvironment is therefore necessary to fully understand the biology of these tumors. The analysis of specific cell surface markers allowed us to confirm the presence of some endothelial progenitors ($VEGFR2^+$, $VE\text{-}Cadherin^+$). In addition, a larger percentage of hematopoietic progenitor and mature cells were also detected in the samples (mainly $CD45^+$ and $CD11b^+$, but also $CXCR4^+$). This preliminary analysis confirmed that some of the initial heterogeneity from the HB primary tumor seems to be maintained *in vitro*. Nevertheless a deep single-cell profiling of each cell is necessary to classify the individual lineages and fully characterize the HB tumor

microenvironment. Single-cell RNA sequencing is an innovative and exciting method that has been used for this purpose [258] and will be used in the near future to tackle this scientific problem.

HB tumors are known to express both HIF1α and HIF2α as a consequence of loss of VHL function. Some studies reported the initial expression of HIF2α, and not HIF1α, in CNS precursor lesions that later mature into HBs [32]. Likewise, we have previously showed that specific HIF2α, and not HIF1α, inhibitors block the formation of hemangioblastoma-like lesions in the brain of *vhl*$^{-/-}$ zebrafish embryos (***Chapter 4***). These different studies indicate that HIF2α is the potential oncogene and main transcription factor involved in HB tumor initiation, mimicking the oncogenic mechanism of VHL-associated ccRCC [119,121,122]. However, and despite these studies, the paradigm and functional role of HIF1α *versus* HIF2α has not been deeply described in the case of HB tumor biology. Our data shows that different HB-derived lines express distinct HIF isoforms. While the *AM1 ACL4* line expresses low levels HIF2α, the *AM2 ACL4* shows the opposite result expressing HIF1α only. This interesting and contrasting result might be caused by tumor heterogeneity regarding HIF1α and HIF2α expression within primary HB tumors. Otherwise, it might also represent distinct cellular adaptations to the artificial conditions *in vitro*, not faithfully recapitulating the *in vivo* biology of HB tumors. The paradigm between HIF1α and HIF2α expression in human CNS HBs is an important scientific question that needs to be clarified in the near future. In particular, because novel HIF2α-specific inhibitors are now being tested in clinical trials for ccRCC and other HIF2α-driven VHL phenotypes.

The study of CNS HB biology is compromised by the lack of accurate mouse models. The *VHL* knockout (KO) mouse is embryonically lethal between E10.5-12 [158]. The conditional KO of *VHL* in the mouse proximal tubule and hepatocytes (using the Lox-VHL-Lox system with PEPCK-Cre) does not form HBs neither it does the conditional mosaic KO of *VHL* (using the

Lox-VHL-Lox system under the control of β-actin promoter) [159,161]. On the other hand, the conditional KO of *VHL* in the mouse liver (using the Lox-VHL-Lox system with Albumin-Cre) develops vascular lesions designated hemangiomas but not hemangioblastomas [160]. Therefore, and at the moment, there is no mouse model available to study CNS HB formation and development. With the aim of establishing a novel animal model for this disease and to confirm the presence of tumor cells within the HB cell cultures, we injected HB-derived cells orthotopically into the brain of immunocompromised mice. Surprisingly, and for the first time, HB-derived cells formed brain tumors in NOD/SCID mice, proving that the cells maintained in culture are indeed HB tumor cells. The injection of these cells in other tissues (such as subcutaneously or in the kidney parenchyma) does not lead to tumor development, which might indicate an important role of the brain microenvironment in the survival and growth of these cells *in vivo*.

The *AM1 ACL4* and *AM2 ACL4*-derived brain tumors were visible by MRI around 9-12 days after injection, which is a short period of time considering the benign phenotype of CNS HBs. While the human HBs are known to grow slowly over a patient's life time, it is true that they suddenly start growing fast. This phenotype seems to be mimicked by the HB-derived lines *in vivo*, which quickly evolve into large masses that avidly uptake gadolinium-based contrast agents. Interestingly, both VHL-associated and sporadic HB-derived tumors (*AM1 ACL4* and *AM2 ACL4*) start developing at comparable time points after injection, although the *AM2 ACL4*-derived tumors tend to grow faster. Additionally, the histology is similar between both tumor groups and characterized by clusters of tumor cells (*stromal* cells) involved in a network of blood vessels and hematopoietic cells. This recapitulates the histology of the human CNS HBs and validates this model as a faithful representation of the human disease.

Magnetic Resonance Imaging and Spectroscopy (MRI/MRS) are techniques used worldwide in the detection, diagnosis and prognosis of brain tumors. In this study we took advantage of these powerful techniques to not only follow the development of the brain tumors in mice but also characterize the *AM1 ACL4* and *AM2 ACL4*-derived tumors *in vivo*. ^{1}H MRS within the tumor region revealed that *AM1 ACL4* and *AM2 ACL4*-derived brain tumors accumulate large amounts of mobile lipids. This result corroborates with a previous MRS study performed in a human CNS HB [259] and confirms that the high intracellular accumulation of lipids characteristic of CNS HBs is replicated in this mouse model. Moreover, the *AM1 ACL4* and *AM2 ACL4*-derived tumors were not invasive and formed circumscribed tumor masses typical of a benign phenotype. Finally, the comparison between the normal brain tissue and the tumors, through diffusion-weighted imaging, revealed higher ADC values in the tumors, possibly due to the extensive blood vessel network (not necrosis or edema) that promotes the massive extravasation of water molecules to the extravascular space. In fact, human CNS HBs are characterized by a highly vascularized microenvironment and achieve ADC levels superior to other brain metastasis[253].

In summary, we used different HB fresh tumors to establish, for the first time, HB-derived cells that express the HB markers PDPN, VEGFα and HIF. The HB-derived cells are formed by heterogeneous populations of cells that maintain the cell growth *in vitro*. Orthotopic injections of the HB-derived cells in NOD/SCID mice produce brain tumors within 9-12 days that recapitulate the clinical features of human CNS HBs, including extensive vascularization, uptake of contrast agents and high lipid content. The similar histology seen between the mouse and the human HBs reflects the potential of this novel animal model to be used as an essential tool in the study of the biology of CNS HBs.

CHAPTER 6

Concluding Remarks and Scientific Contribution

6.1. Concluding Remarks and Future Directions

In an era of targeted therapy and personalized medicine, different studies have used scientific technologies and disease models to identify and validate novel therapeutic targets. The current state of the art for VHL-associated Hemangioblastomas (HBs) is weak; there is a lack of therapeutic options to treat VHL patients and the knowledge on the biology of HBs is limited. In this doctoral thesis, we aimed to tackle this problem by pioneering the development of scientific resources and specific therapies to treat CNS HBs. We combined unbiased genome-wide profiling with functional target validation studies and mapped HIF2α as a therapeutic target of the disease. We then showed that small-molecule HIF2α inhibitors can treat the VHL-associated phenotypes *in vivo*. Finally, we established the first mouse model of CNS HBs, which can now be used as a preclinical tool to test different therapeutic strategies.

The main shortcoming of targeted therapy is the development of resistant mechanisms that allow the survival and growth of tumor cells in the presence of the therapeutic drug. While transcription factors (such as HIF2α) have not been initially attractive for drug design, they are now been systematically targeted because they are, in several cases, the central oncogenic orchestrators of tumor development. The rationale for using HIF2α inhibitors is that we are targeting the central activator – as a transcription factor – of pathways involved in tumor growth, angiogenesis and aberrant metabolism in the $VHL^{-/-}$ tumor cell, as opposed to inhibiting one or two of the three hundred downstream HIF-target genes which has proved ineffective in the clinic. In fact, until gene therapy evolves to correct the initial germline defect in the *VHL* gene, other therapeutic strategies (such HIF2α inhibition) need to be employed for the long-term treatment of this chronic disease. In this case, the successful blockage of HIF2α activity in these patients is expected not only to prevent HB tumor formation, but also, the development of the

other constellation of phenotypes associated with loss of VHL, such as clear cell renal cell carcinomas (ccRCC), liver hemangiomas and systemic secondary erythropoiesis. While our studies provided preliminary evidence that lead compounds indeed have the potential to treat the VHL disease, they also preceded landmark clinical trials currently testing the efficacy of HIF2a inhibitors in ccRCC and VHL patients (Peloton Therapeutics, PT2385). This is the beginning of a new era for the treatment of the VHL disease, whose outcome we await with much enthusiasm and which, hopefully, will expand the treatment options for CNS HBs.

While new target therapies show promise on VHL patients, the biology of HBs in poorly understood. Most reported studies are focused on the characterization of hypothesis-driven biomarkers in fixed and dead tumors. Therefore, these biased approaches do not capture the *in vivo* dynamic of HBs as well as the cell interactions and active signaling pathways within the tumor microenvironment. Considering the heterogeneous and exciting biology of such tumors (as evidenced herein), genome-wide efforts are necessary to identify the mutational landscape underlying the development of HBs. Such studies should involve single-cell and tumor bulk sequencing techniques on fresh HB biopsies to unbiasedly identify the oncogenic pathways of these brain tumors. Moreover, the development of HB cell lines should be of the utmost priority, to study the behavior of HB cells *in vitro* and test new scientific hypotheses. In this doctoral thesis, we aimed to develop such tools and were able to grow cell cultures from human HB tumors. However, these cells were not immortalized and cannot be expanded indefinitely. Therefore, a major effort in the future should be on continuing this and others' work to develop stable HB cell lines. The study of these cells and their use in lineage tracing experiments is likely to answer the current paradigm of the HB cell of origin. We anticipate this approach will lead to the development of novel therapeutic strategies and additional HB animal models.

The availability of animal models that faithful mimic cancer development is considered as one of the main bottlenecks in cancer research and cancer drug development. The existence of preclinical animal models for a specific disease is fundamental to validate biological hypotheses and test pharmacological drugs. In this context, the difficulty is on mimicking the complex human body without using real patients during the experimentation process. Therefore, animal models should recapitulate most of the disease phenotypes in order to warrant future clinical trials; and the current animal models to study VHL disease are indeed limited. The only model available that recapitulates some of the VHL-associated phenotypes is the zebrafish *vhl* embryo. Yet, while being a great model for drug screenings and genetic manipulation, it does not mimic the complex human physiological system. In this thesis, we aimed to pioneer an alternative model for CNS HBs, and established an orthotopic mouse model that faithfully recapitulates several aspects of the human disease. This model exhibits main morphological features of HBs and thereby represents a new tool to study VHL-associated brain tumors.

This doctoral work elucidated new biology of VHL-associated Hemangioblastomas and established new methodologies to identify, validate and test novel therapeutic strategies for the treatment of this lifelong disease.

"Meeting VHL patients and learning about their daily challenges in person was one of the most inspiring experiences of my doctoral work. I hope this thesis starts to answer some of the most fascinating questions about Hemangioblastomas and, more importantly, that it inspires others to continue this incredible roller-coaster."

6.2. Scientific Contribution

The following scientific publications summarize the academic contribution completed during this doctoral thesis.

- **Metelo AM**, Noonan HR, Li X, Jin Y, Baker R, Kamentsky L, Zhang Y, van Rooijen E, Shin J, Carpenter AE, Yeh JR, Peterson RT, Iliopoulos O. Pharmacological HIF2α inhibition improves VHL disease-associated phenotypes in zebrafish model. *Journal of Clinical Investigation.* 2015;125(5):1987-1997.

- **Metelo AM**, Noonan HR, Iliopoulos O. HIF2α inhibitors for the treatment of VHL disease. *Oncotarget.* 2015;6(27):23036-7.

- **Metelo AM** and Iliopoulos O. Hemangioblastomas of the Central Nervous System. *Rosenberg's Molecular and Genetic Basis of Neurological and Psychiatric Disease*. Academic Press, 5th Edition 2015, 82:955-959.

Publication in preparation

- **Metelo AM**, Kamburov A, Noonan HR, Yizhak K, Kim J, Barker F, Nahed B, Stemmer-Rachamimov A, Getz G, Iliopoulos O. Loss of PNPLA3/Adiponutrin is a recurrent molecular event in VHL-associated CNS Hemangioblastomas. *(in preparation)*

Collaborative projects

- Noonan HR, **Metelo AM**, Kamei CN, Peterson RT, Drummond IA, Iliopoulos O. Loss of vhl in the Zebrafish Pronephros Recapitulates Early Stages of Human Clear Cell Renal Cell Carcinoma. *Disease Models and Mechanisms.* 2016;9(8):873-84.

- Gameiro PA, Yang J, **Metelo AM**, Pérez-Carro R, Baker R, Wang Z, Arreola A, Rathmell WK, Olumi A, López-Larrubia P, Stephanopoulos G, Iliopoulos O. In vivo HIF-mediated reductive carboxylation is regulated by citrate levels and sensitizes VHL-deficient cells to glutamine deprivation. *Cell Metabolism.* 2013;17(3):372-85.

CHAPTER 7

Bibliography

1. Lonser, R. R. *et al.* von Hippel-Lindau disease. **361,** 2059–2067 (2003).

2. Feletti, A. *et al.* Von Hippel-Lindau disease: an evaluation of natural history and functional disability. *Neuro. Oncol.* **18,** 1011-1120 (2016).

3. Doyle, L. A. & Fletcher, C. D. M. Peripheral hemangioblastoma: clinicopathologic characterization in a series of 22 cases. *Am. J. Surg. Pathol.* **38,** 119–127 (2014).

4. López Basave, H. N. *et al.* Primary gastric hemangioblastoma: report of a case. *Rare Tumors* **7,** 7–8 (2015).

5. Shi, H., Li, H., Zhen, T., Zhang, F. & Han, A. Case Report Hemangioblastoma of pelvic cavity : report of a case and review of literature. **7,** 7054–7058 (2014).

6. Park, D. M. *et al.* von Hippel-Lindau disease-associated hemangioblastomas are derived from embryologic multipotent cells. *PLoS Med.* **4,** e60 (2007).

7. Maher, E. R. *et al.* Von Hippel-Lindau disease: a genetic study. *J Med Genet* **28,** 443–447 (1991).

8. Neumann, H. P. & Wiestler, O. D. Clustering of features of von Hippel-Lindau syndrome: evidence for a complex genetic locus. *Lancet (London, England)* **337,** 1052–1054 (1991).

9. Knudson, A. G. Mutation and cancer: statistical study of retinoblastoma. *Proc. Natl. Acad. Sci. U. S. A.* **68,** 820–823 (1971).

10. Stein, A. A., Schilp, A. O. & Whitfield, R. D. The histogenesis of hemangioblastoma of the brain. A review of twenty-one cases. *J. Neurosurg.* **17,** 751–761 (1960).

11. Vortmeyer, A. O. *et al.* Developmental arrest of angioblastic lineage initiates tumorigenesis in von Hippel-Lindau disease. *Cancer Res.* **63,** 7051–7055 (2003).

12. Merrill, M. J., Edwards, N. a & Lonser, R. R. Hemangioblastoma-associated mast cells in von Hippel-Lindau disease are tumor derived. *Blood* **121,** 859–860 (2013).

13. Vortmeyer, A. O. *et al.* von Hippel-Lindau gene deletion detected in the stromal cell component of a cerebellar hemangioblastoma associated with von Hippel-Lindau disease. *Hum. Pathol.* **28,** 540–543 (1997).

14. Lonser, R. R. *et al.* Edema is a precursor to central nervous system peritumoral cyst formation. *Ann. Neurol.* **58,** 392–399 (2005).

15. Filling-Katz, M. R. *et al.* Central nervous system involvement in Von Hippel-Lindau disease. *Neurology* **41,** 41–46 (1991).

16. Rickert, C. H., Hasselblatt, M., Jeibmann, A. & Paulus, W. Cellular and reticular variants of hemangioblastoma differ in their cytogenetic profiles. *Hum. Pathol.* **37,** 1452–1457 (2006).

17. Hasselblatt, M. *et al.* Cellular and reticular variants of haemangioblastoma revisited: a clinicopathologic study of 88 cases. *Neuropathol. Appl. Neurobiol.* **31,** 618–622 (2005).

18. Shively, S. B. *et al.* Protracted haemangioblastic proliferation and differentiation in von Hippel – Lindau disease. 514–520 (2008).

19. Lee, J. *et al.* Loss of Heterozygosity and Somatic Mutations of the VHL Tumor Suppressor Gene in Sporadic Cerebellar Hemangioblastomas. *Cancer Res.* **58,** 504–508 (1998).

20. Omulecka, A., Lach, B., Alwasiak, J. & Gregor, A. Immunohistochemical and ultrastructural studies of stromal cells in hemangioblastoma. *Folia Neuropathol.* **33,** 41–50 (1995).

21. Lach, B., Gregor, A., Rippstein, P. & Omulecka, A. Angiogenic histogenesis of stromal cells in hemangioblastoma: ultrastructural and immunohistochemical study. *Ultrastruct. Pathol.* **23,** 299–310 (1999).

22. Cruz-Sánchez, F. F. *et al.* Haemangioblastoma: histological and immunohistological study of an enigmatic cerebellar tumour. *Histol. Histopathol.* **5,** 407–413 (1990).

23. Ishizawa, K., Komori, T. & Hirose, T. Stromal cells in hemangioblastoma: neuroectodermal differentiation and morphological similarities to ependymoma. *Pathol. Int.* **55,** 377–385 (2005).

24. Huber, T. L., Kouskoff, V., Fehling, H. J. & Palis, J. Haemangioblast commitment is initiated in the primitive streak of the mouse embryo. **432,** 625–630 (2004).

25. Keller, G. Embryonic stem cell differentiation: emergence of a new era in biology and medicine. *Genes Dev.* **19,** 1129–1155 (2005).

26. Gering, M., Rodaway, A. R., Göttgens, B., Patient, R. K. & Green, A. R. The SCL gene specifies haemangioblast development from early mesoderm. *EMBO J.* **17,** 4029–4045 (1998).

27. Choi, K., Kennedy, M., Kazarov, a, Papadimitriou, J. C. & Keller, G. A common precursor for hematopoietic and endothelial cells. *Development* **125,** 725–732 (1998).

28. Kennedy, M., D'Souza, S. L., Lynch-Kattman, M., Schwantz, S. & Keller, G. Development of the hemangioblast defines the onset of hematopoiesis in human ES cell differentiation cultures. *Blood* **109,** 2679–2687 (2007).

29. Gläsker, S. *et al.* Hemangioblastomas share protein expression with embryonal hemangioblast progenitor cell. *Cancer Res.* **66,** 4167–4172 (2006).

30. Vortmeyer, A. O., Yuan, Q., Lee, Y. S., Zhuang, Z. & Oldfield, E. H. Developmental Effects of von Hippel-Lindau Gene Deficiency. *Ann. Neurol.* **55,** 721–728 (2004).

31. Vortmeyer, A. *et al.* Evolution of VHL tumourigenesis in nerve root tissue. *J. Pathol.* **210,** 374–382 (2006).

32. Shively, S. B. *et al.* Developmentally arrested structures preceding cerebellar tumors in von Hippel-Lindau disease. *Mod. Pathol.* **24,** 1023–1030 (2011).

33. Welten, C. M., Keats, E. C., Ang, L. & Khan, Z. A. Hemangioblastoma Stromal Cells Show Committed Stem Cell Phenotype. *Can. J. Neurol. Sci.* **39,** 821–827 (2012).

34. Chan, C.-C., Chew, E. Y., Shen, D., Hackett, J. & Zhuang, Z. Expression of stem cells markers in ocular hemangioblastoma associated with von Hippel-Lindau (VHL) disease. *Mol. Vis.* **11,** 697–704 (2005).

35. Singh, S. K. *et al.* Identification of a cancer stem cell in human brain tumors. *Cancer Res.* **63,** 5821–5828 (2003).

36. Singh, S. K. *et al.* Identification of human brain tumour initiating cells. *Nature* **432,** 396–401 (2004).

37. Roy, S., Chu, A., Trojanowski, J. Q. & Zhang, P. J. D2-40, a novel monoclonal antibody against the M2A antigen as a marker to distinguish hemangioblastomas from renal cell carcinomas. *Acta Neuropathol.* **109,** 497–502 (2005).

38. Astarita, J. L., Acton, S. E. & Turley, S. J. Podoplanin: Emerging functions in development, the immune system, and cancer. *Front. Immunol.* **3,** 1–11 (2012).

39. Hoang, M. P. & Amirkhan, R. H. Inhibin alpha distinguishes hemangioblastoma from clear cell renal cell carcinoma. *Am. J. Surg. Pathol.* **27,** 1152–1156 (2003).

40. Koo, H.-W. *et al.* Hemangioblastomas with leptomeningeal dissemination: case series and review of the literature. *Acta Neurochir. (Wien).* **158,** 1169–1178 (2016).

41. Trimble, M., Caro, J., Talalla, A. & Brain, M. Secondary erythrocytosis due to a cerebellar hemangioblastoma: demonstration of erythropoietin mRNA in the tumor. *Blood* **78,** 599–601 (1991).

42. Huntoon, K. *et al.* Biological and clinical impact of hemangioblastoma-associated peritumoral cysts in von Hippel-Lindau disease. **124,** 1–6 (2015).

43. Jagannathan, J., Lonser, R. R., Smith, R., DeVroom, H. L. & Oldfield, E. H. Surgical management of cerebellar hemangioblastomas in patients with von Hippel-Lindau disease. *J. Neurosurg.* **108,** 210–222 (2008).

44. Moss, J. M. *et al.* Stereotactic radiosurgical treatment of cranial and spinal hemangioblastomas. *Neurosurgery* **65,** 79–85; discussion 85 (2009).

45. Kano, H. *et al.* The role of stereotactic radiosurgery for intracranial hemangioblastomas. *Neurosurgery* **63,** 443-50 (2008).

46. Asthagiri, A. R. *et al.* Prospective evaluation of radiosurgery for hemangioblastomas in von Hippel-Lindau disease. *Neuro. Oncol.* **12,** 80–86 (2010).

47. Boughey, A. M., Fletcher, N. A. & Harding, A. E. Central nervous system haemangioblastoma: a clinical and genetic study of 52 cases. *J. Neurol. Neurosurg. Psychiatry* **53,** 644–648 (1990).

48. Lee, G. J. *et al.* The clinical experience of recurrent central nervous system hemangioblastomas. *Clin. Neurol. Neurosurg.* **123,** 90–95 (2014).

49. Iliopoulos, O., Kibel, A., Gray, S. & Kaelin, W. G. Tumour suppression by the human von Hippel-Lindau gene product. *Nat. Med.* **1,** 822–826 (1995).

50. Latif, F. *et al.* Identification of the von Hippel-Lindau disease tumor suppressor gene. *Science* **260,** 1317–1320 (1993).

51. Gnarra, J. *et al.* Mutations of the VHL tumour suppressor gene in renal carcinoma. *Nat. Genet.* **7,** 85–90 (1994).

52. Iliopoulos, O. Molecular biology of renal cell cancer and the identification of therapeutic targets. *J. Clin. Oncol.* **24,** 5593–5600 (2006).

53. Binderup, M. L. M., Jensen, A. M., Budtz-Jørgensen, E. & Bisgaard, M. L. Survival and causes of death in patients with von Hippel-Lindau disease. *J. Med. Genet.* (2016).

54. Leiserson, M. D. M. *et al.* Pan-cancer network analysis identifies combinations of rare somatic mutations across pathways and protein complexes. *Nat. Genet.* **47,** 106-114 (2014).

55. Iliopoulos, O., Ohh, M. & Kaelin, W. G. pVHL 19 is a biologically active product of the von Hippel – Lindau gene arising from internal translation initiation. *Biochemistry* **95,** 11661–11666 (1998).

56. Kibel, A., Iliopoulos, O., DeCaprio, J. A. & Kaelin, W. G. Binding of the von Hippel-Lindau tumor suppressor protein to Elongin B and C. *Science.* **269,** 1444–1446 (1995).

57. Lonergan, K. M. *et al.* Regulation of hypoxia-inducible mRNAs by the von Hippel-Lindau tumor suppressor protein requires binding to complexes containing elongins B/C and Cul2. *Mol. Cell. Biol.* **18,** 732–741 (1998).

58. Lisztwan, J., Imbert, G., Wirbelauer, C., Gstaiger, M. & Krek, W. The von Hippel-Lindau tumor suppressor protein is a component of an E3 ubiquitin-protein ligase activity. *Genes Dev* **13,** 1822–1833 (1999).

59. Maxwell, P. H. *et al.* The tumour suppressor protein VHL targets hypoxia-inducible factors for oxygen-dependent proteolysis. *Nature* **399,** 271–275 (1999).

60. Ohh, M. *et al.* Ubiquitination of hypoxia-inducible factor requires direct binding to the beta-domain of the von Hippel-Lindau protein. *Nat. Cell Biol.* **2,** 423–427 (2000).

61. Chitalia, V. C. *et al.* Jade-1 inhibits Wnt signalling by ubiquitylating beta-catenin and mediates Wnt pathway inhibition by pVHL. *Nat. Cell Biol.* **10,** 1208–1216 (2008).

62. Ohh, M. *et al.* The von Hippel-Lindau tumor suppressor protein is required for proper assembly of an extracellular fibronectin matrix. *Mol. Cell* **1,** 959–968 (1998).

63. Thoma, C. R. *et al.* pVHL and GSK3beta are components of a primary cilium-maintenance signalling network. *Nat. Cell Biol.* **9,** 588–595 (2007).

64. Jaakkola, P. *et al.* Targeting of HIF-alpha to the von Hippel-Lindau ubiquitylation complex by O2-regulated prolyl hydroxylation. *Science* **292,** 468–472 (2001).

65. Epstein, A. C. *et al.* C. elegans EGL-9 and mammalian homologs define a family of dioxygenases that regulate HIF by prolyl hydroxylation. *Cell* **107,** 43–54 (2001).

66. Ivan, M. *et al.* HIFalpha targeted for VHL-mediated destruction by proline hydroxylation: implications for O2 sensing. *Science* **292,** 464–468 (2001).

67. Ivan, M. *et al.* Biochemical purification and pharmacological inhibition of a mammalian prolyl hydroxylase acting on hypoxia-inducible factor. *Proc. Natl. Acad. Sci. U. S. A.* **99,** 13459–13464 (2002).

68. Depping, R. *et al.* Nuclear translocation of hypoxia-inducible factors (HIFs): Involvement of the classical importin a/b pathway. *Biochim. Biophys. Acta - Mol. Cell Res.* **1783,** 394–404 (2008).

69. Mahon, P. C., Hirota, K. & Semenza, G. L. FIH-1: a novel protein that interacts with HIF-1alpha and VHL to mediate repression of HIF-1 transcriptional activity. *Genes Dev.* **15,** 2675–2686 (2001).

70. Lando, D. *et al.* FIH-1 is an asparaginyl hydroxylase enzyme that regulates the transcriptional activity of hypoxia-inducible factor. *Genes Dev.* **16,** 1466–1471 (2002).

71. Hewitson, K. S. *et al.* Hypoxia-inducible factor (HIF) asparagine hydroxylase is identical to factor inhibiting HIF (FIH) and is related to the cupin structural family. *J. Biol. Chem.* **277,** 26351–26355 (2002).

72. Wang, G. L., Jiang, B. H., Rue, E. A. & Semenza, G. L. Hypoxia-inducible factor 1 is a basic-helix-loop-helix-PAS heterodimer regulated by cellular O2 tension. *Proc. Natl. Acad. Sci. U. S. A.* **92,** 5510–5514 (1995).

73. Tian, H., McKnight, S. L. & Russell, D. W. Endothelial PAS domain protein 1 (EPAS1), a transcription factor selectively expressed in endothelial cells. *Genes Dev.* **11,** 72–82 (1997).

74. Flamme, I. *et al.* HRF, a putative basic helix-loop-helix-PAS-domain transcription factor is closely related to hypoxia-inducible factor-1 alpha and developmentally expressed in blood vessels. *Mech. Dev.* **63,** 51–60 (1997).

75. Ema, M. *et al.* A novel bHLH-PAS factor with close sequence similarity to hypoxia-inducible factor 1alpha regulates the VEGF expression and is potentially involved in lung and vascular development. *Proc. Natl. Acad. Sci. U. S. A.* **94,** 4273–4278 (1997).

76. Hogenesch, J. B. *et al.* Characterization of a subset of the basic-helix-loop-helix-PAS superfamily that interacts with components of the dioxin signaling pathway. *J. Biol. Chem.* **272,** 8581–8593 (1997).

77. Keith, B., Johnson, R. S. & Simon, M. C. HIF1α and HIF2α: sibling rivalry in hypoxic tumor growth and progression. *Nature Rev. Cancer* **12,** 9-22 (2012).

78. Carmeliet, P. & Jain, R. K. Molecular mechanisms and clinical applications of angiogenesis. *Nature* **473,** 298–307 (2011).

79. Tang, N. *et al.* Loss of HIF-1alpha in endothelial cells disrupts a hypoxia-driven VEGF autocrine loop necessary for tumorigenesis. *Cancer Cell* **6,** 485–495 (2004).

80. Yamashita, T. *et al.* Hypoxia-inducible transcription factor-2alpha in endothelial cells regulates tumor neovascularization through activation of ephrin A1. *J. Biol. Chem.* **283,** 18926–36 (2008).

81. Skuli, N. *et al.* Endothelial deletion of hypoxia-inducible factor-2alpha (HIF-2alpha) alters vascular function and tumor angiogenesis. *Blood* **114,** 469–477 (2009).

82. Lee, F. S. & Percy, M. J. The HIF pathway and erythrocytosis. *Annu. Rev. Pathol.* **6,** 165–192 (2011).

83. Rankin, E. B. *et al.* Hypoxia-inducible factor-2 (HIF-2) regulates hepatic erythropoietin in vivo. *J. Clin. Invest.* **117,** 1068–1077 (2007).

84. Iyer, N. V *et al.* Cellular and developmental control of O2 homeostasis by hypoxia-inducible factor 1 alpha. *Genes Dev.* **12,** 149–162 (1998).

85. Ryan, H. E., Lo, J. & Johnson, R. S. HIF-1 alpha is required for solid tumor formation and embryonic vascularization. *EMBO J.* **17,** 3005–3015 (1998).

86. Kim, J., Tchernyshyov, I., Semenza, G. L. & Dang, C. V. HIF-1-mediated expression of pyruvate dehydrogenase kinase: a metabolic switch required for cellular adaptation to hypoxia. *Cell Metab.* **3,** 177–185 (2006).

87. Papandreou, I., Cairns, R. A., Fontana, L., Lim, A. L. & Denko, N. C. HIF-1 mediates adaptation to hypoxia by actively downregulating mitochondrial oxygen consumption. *Cell Metab.* **3,** 187–197 (2006).

88. Gameiro, P. A. *et al.* In vivo HIF-mediated reductive carboxylation is regulated by citrate levels and sensitizes VHL-deficient cells to glutamine deprivation. *Cell Metab.* **17,** 372–385 (2013).

89. Metallo, C. M. *et al.* Reductive glutamine metabolism by IDH1 mediates lipogenesis under hypoxia. *Nature* **481,** 380–384 (2012).

90. Huang, D. *et al.* HIF-1-mediated suppression of acyl-CoA dehydrogenases and fatty acid oxidation is critical for cancer progression. *Cell Rep.* **8,** 1930–1942 (2014).

91. Spence, A. M. & Rubinstein, L. J. Cerebellar capillary hemangioblastoma: its histogenesis studied by organ culture and electron microscopy. *Cancer* **35,** 326–341 (1975).

92. Qiu, B. *et al.* HIF2α-Dependent Lipid Storage Promotes Endoplasmic Reticulum Homeostasis in Clear-Cell Renal Cell Carcinoma. *Cancer Discov.* **5,** 652–667 (2015).

93. Walther, T. C. & Farese, R. V. Lipid droplets and cellular lipid metabolism. *Annu. Rev. Biochem.* **81,** 687–714 (2012).

94. Rankin, E. B. *et al.* Hypoxia-inducible factor 2 regulates hepatic lipid metabolism. *Mol. Cell. Biol.* **29,** 4527–4538 (2009).

95. Genbacev, O., Zhou, Y., Ludlow, J. W. & Fisher, S. J. Regulation of human placental development by oxygen tension. *Science* **277,** 1669–1672 (1997).

96. Simon, M. C. & Keith, B. The role of oxygen availability in embryonic development and stem cell function. *Nat. Rev. Mol. Cell Biol.* **9,** 285–296 (2008).

97. Ezashi, T., Das, P. & Roberts, R. M. Low O2 tensions and the prevention of differentiation of hES cells. *Proc. Natl. Acad. Sci. U. S. A.* **102,** 4783–4788 (2005).

98. Hu, C. *et al.* Differential Regulation of the Transcriptional Activities of Hypoxia-Inducible Factor 1 Alpha (HIF-1a) and HIF-2a in Stem Cells. *Mol. Cell Biol.* **26,** 3514–3526 (2006).

99. Studer, L. *et al.* Enhanced proliferation, survival, and dopaminergic differentiation of CNS precursors in lowered oxygen. *J. Neurosci.* **20,** 7377–7383 (2000).

100. Morrison, S. J. *et al.* Culture in reduced levels of oxygen promotes clonogenic sympathoadrenal differentiation by isolated neural crest stem cells. *J. Neurosci.* **20,** 7370–7376 (2000).

101. Ramírez-Bergeron, D. L. *et al.* Hypoxia affects mesoderm and enhances hemangioblast specification during early development. *Development* **131,** 4623–4634 (2004).

102. Parmar, K., Mauch, P., Vergilio, J.-A., Sackstein, R. & Down, J. D. Distribution of hematopoietic stem cells in the bone marrow according to regional hypoxia. *Proc. Natl. Acad. Sci. U. S. A.* **104,** 5431–5436 (2007).

103. Danet, G. H., Pan, Y., Luongo, J. L., Bonnet, D. A. & Simon, M. C. Expansion of human SCID-repopulating cells under hypoxic conditions. *J. Clin. Invest.* **112,** 126–35 (2003).

104. Keith, B. & Simon, M. C. Hypoxia-inducible factors, stem cells, and cancer. *Cell* **129,** 465–472 (2007).

105. Covello, K. L. *et al.* HIF-2alpha regulates Oct-4: effects of hypoxia on stem cell function, embryonic development, and tumor growth. *Genes Dev.* **20,** 557–570 (2006).

106. Gordan, J. D., Bertout, J. A., Hu, C.-J., Diehl, J. A. & Simon, M. C. HIF-2alpha promotes hypoxic cell proliferation by enhancing c-myc transcriptional activity. *Cancer Cell* **11,** 335–347 (2007).

107. Gustafsson, M. V. *et al.* Hypoxia requires Notch signaling to maintain the undifferentiated cell state. *Dev. Cell* **9,** 617–628 (2005).

108. Raval, R. R. *et al.* Contrasting properties of hypoxia-inducible factor 1 (HIF-1) and HIF-2 in von Hippel-Lindau-associated renal cell carcinoma. *Mol. Cell. Biol.* **25,** 5675–5686 (2005).

109. Gunaratnam, L. *et al.* Hypoxia inducible factor activates the transforming growth factor-alpha/epidermal growth factor receptor growth stimulatory pathway in VHL(-/-) renal cell carcinoma cells. *J. Biol. Chem.* **278,** 44966–44974 (2003).

110. Hu, C., Wang, L., Chodosh, L. A., Keith, B. & Simon, M. C. Differential Roles of HIF-1 and HIF-2 in Hypoxic Gene Regulation. *Mol. Cell. Biol.* **23,** 9361–9374 (2003).

111. Matrone, C. *et al.* HIF-1alpha reveals a binding activity to the promoter of iNOS gene after permanent middle cerebral artery occlusion. *J. Neurochem.* **90,** 368–378 (2004).

112. Jung, F., Palmer, L. A., Zhou, N. & Johns, R. A. Hypoxic regulation of inducible nitric oxide synthase via hypoxia inducible factor-1 in cardiac myocytes. *Circ. Res.* **86,** 319–325 (2000).

113. Staller, P. *et al.* Chemokine receptor CXCR4 downregulated by von Hippel-Lindau tumour suppressor pVHL. *Nature* **425,** 307–311 (2003).

114. Wykoff, C. C. *et al.* Hypoxia-inducible expression of tumor-associated carbonic anhydrases. *Cancer Res.* **60,** 7075–7083 (2000).

115. Erler, J. T. *et al.* Lysyl oxidase is essential for hypoxia-induced metastasis. *Nature* **440,** 1222–1226 (2006).

116. Petrella, B. L., Lohi, J. & Brinckerhoff, C. E. Identification of membrane type-1 matrix metalloproteinase as a target of hypoxia-inducible factor-2 alpha in von Hippel-Lindau renal cell carcinoma. *Oncogene* **24,** 1043–1052 (2005).

117. Esteban, M. A. *et al.* Regulation of E-cadherin expression by VHL and hypoxia-inducible factor. *Cancer Res.* **66,** 3567–3575 (2006).

118. Heddleston, J. M. *et al.* Hypoxia-induced mixed-lineage leukemia 1 regulates glioma stem cell tumorigenic potential. *Cell Death Differ.* **19,** 428–439 (2012).

119. Zimmer, M., Doucette, D., Siddiqui, N. & Iliopoulos, O. Inhibition of Hypoxia-Inducible Factor Is Sufficient for Growth Suppression of VHL − / − Tumors 1 *Mol. Cancer Res.* **2,** 89-95 (2004).

120. Noguera, R. *et al.* HIF-1alpha and HIF-2alpha are differentially regulated in vivo in neuroblastoma: high HIF-1alpha correlates negatively to advanced clinical stage and tumor vascularization. *Clin. Cancer Res.* **15,** 7130–7136 (2009).

121. Kondo, K., Kim, W. Y., Lechpammer, M. & Kaelin, W. G. Inhibition of HIF2alpha is sufficient to suppress pVHL-defective tumor growth. *PLoS Biol.* **1,** E83 (2003).

122. Kondo, K., Klco, J., Nakamura, E., Lechpammer, M. & Kaelin, W. G. Inhibition of HIF is necessary for tumor suppression by the von Hippel-Lindau protein. *Cancer Cell* **1,** 237–246 (2002).

123. Wizigmann-Voos, S., Breier, G., Risau, W. & Plate, K. H. Up-regulation of vascular endothelial growth factor and its receptors in von Hippel-Lindau disease-associated and sporadic hemangioblastomas. *Cancer Res.* **55,** 1358–1364 (1995).

124. Böhling, T. *et al.* Expression of growth factors and growth factor receptors in capillary hemangioblastoma. *J. Neuropathol. Exp. Neurol.* **55,** 522–527 (1996).

125. Shankar, G. M. *et al.* Sporadic hemangioblastomas are characterized by cryptic VHL inactivation. *Acta Neuropathol. Commun.* **2,** 1–12 (2014).

126. Zagzag, D. *et al.* Stromal cell-derived factor-1alpha and CXCR4 expression in hemangioblastoma and clear cell-renal cell carcinoma: von Hippel-Lindau loss-of-function induces expression of a ligand and its receptor. *Cancer Res.* **65,** 6178–6188 (2005).

127. Reifenberger, G., Reifenberger, J., Bilzer, T., Wechsler, W. & Collins, V. P. Coexpression of transforming growth factor-alpha and épidermal growth factor receptor in capillary hemangioblastomas of the central nervous system. *Am. J. Pathol.* **147,** 245–250 (1995).

128. Merrill, M. J., Edwards, N. a & Lonser, R. R. Notch receptor and effector expression in von Hippel-Lindau disease-associated central nervous system hemangioblastomas. *J. Neurosurg.* **115,** 512–517 (2011).

129. Kaelin, W. G. Molecular basis of the VHL hereditary cancer syndrome. *Nat. Rev. Cancer* **2,** 673–682 (2002).

130. Creighton *et al.* Comprehensive molecular characterization of clear cell renal cell carcinoma. *Nature* **499,** 43–49 (2013).

131. Ding, L. *et al.* Somatic mutations affect key pathways in lung adenocarcinoma. *Nature* **455,** 1069–1075 (2008).

132. Cancer Genome Atlas Research Network. Comprehensive genomic characterization defines human glioblastoma genes and core pathways. *Nature* **455,** 1061–1068 (2008).

133. Cancer Genome Atlas Network. Comprehensive molecular characterization of human colon and rectal cancer. *Nature* **487,** 330–337 (2012).

134. Brastianos, P. K. *et al.* Exome sequencing identifies BRAF mutations in papillary craniopharyngiomas. *Nat. Genet.* **46,** 161–165 (2014).

135. Lawrence, M. S. *et al.* Mutational heterogeneity in cancer and the search for new cancer-associated genes. *Nature* **499,** 214–218 (2013).

136. Vogelstein, B. *et al.* Cancer Genome Landscapes. *Science* **339,** 1546–1558 (2013).

137. Davies, H. *et al.* Mutations of the BRAF gene in human cancer. *Nature* **417,** 949–954 (2002).

138. Sosman, J. A. *et al.* Survival in BRAF V600-mutant advanced melanoma treated with vemurafenib. *N. Engl. J. Med.* **366,** 707–714 (2012).

139. Hauschild, A. *et al.* Dabrafenib in BRAF-mutated metastatic melanoma: a multicentre, open-label, phase 3 randomised controlled trial. *Lancet (London, England)* **380,** 358–365 (2012).

140. Engelman, J. A. *et al.* Effective use of PI3K and MEK inhibitors to treat mutant Kras G12D and PIK3CA H1047R murine lung cancers. *Nat. Med.* **14,** 1351–1356 (2008).

141. Artale, S. *et al.* Mutations of KRAS and BRAF in primary and matched metastatic sites of colorectal cancer. *J. Clin. Oncol.* **26,** 4217–4219 (2008).

142. Lee, C. K. *et al.* Impact of EGFR inhibitor in non-small cell lung cancer on progression-free and overall survival: a meta-analysis. *J. Natl. Cancer Inst.* **105,** 595–605 (2013).

143. Turajlic, S., Larkin, J. & Swanton, C. SnapShot: Renal Cell Carcinoma. *Cell* **163,** 1556–1556.e1 (2015).

144. Motzer, R. J. *et al.* Sunitinib versus interferon alfa in metastatic renal-cell carcinoma. *N. Engl. J. Med.* **356,** 115–124 (2007).

145. Escudier, B. *et al.* Sorafenib in advanced clear-cell renal-cell carcinoma. *N. Engl. J. Med.* **356,** 125–134 (2007).

146. Yang, J. C. *et al.* A randomized trial of bevacizumab, an anti-vascular endothelial growth factor antibody, for metastatic renal cancer. *N. Engl. J. Med.* **349,** 427–434 (2003).

147. Escudier, B. *et al.* Phase III trial of bevacizumab plus interferon alfa-2a in patients with metastatic renal cell carcinoma (AVOREN): final analysis of overall survival. *J. Clin. Oncol.* **28,** 2144–2150 (2010).

148. Sternberg, C. N. *et al.* Pazopanib in locally advanced or metastatic renal cell carcinoma: results of a randomized phase III trial. *J. Clin. Oncol.* **28,** 1061–1068 (2010).

149. Motzer, R. J. *et al.* Axitinib versus sorafenib as second-line treatment for advanced renal cell carcinoma: overall survival analysis and updated results from a randomised phase 3 trial. *Lancet. Oncol.* **14,** 552–562 (2013).

150. Hudes, G. *et al.* Temsirolimus, interferon alfa, or both for advanced renal-cell carcinoma. *N. Engl. J. Med.* **356,** 2271–2281 (2007).

151. Motzer, R. J. *et al.* Phase 3 trial of everolimus for metastatic renal cell carcinoma : final results and analysis of prognostic factors. *Cancer* **116,** 4256–4265 (2010).

152. Jonasch, E. *et al.* Pilot trial of sunitinib therapy in patients with von Hippel-Lindau disease. *Ann. Oncol.* **22,** 2661–2666 (2011).

153. Kim, B. Y. S., Jonasch, E. & McCutcheon, I. E. Pazopanib therapy for cerebellar hemangioblastomas in von Hippel-Lindau disease: case report. *Target. Oncol.* **7,** 145–149 (2012).

154. Migliorini, D. *et al.* Recurrent multiple CNS hemangioblastomas with VHL disease treated with pazopanib: a case report and literature review. *CNS Oncol.* **4,** 387–392 (2015).

155. Seystahl, K., Weller, M., Bozinov, O., Reimann, R. & Rushing, E. Neuropathological characteristics of progression after prolonged response to bevacizumab in multifocal hemangioblastoma. *Oncol. Res. Treat.* **37,** 209–212 (2014).

156. Omar, A. I. Bevacizumab for the treatment of surgically unresectable cervical cord hemangioblastoma: a case report. *J. Med. Case Rep.* **6,** 238 (2012).

157. Slim, E., Antoun, J., Kourie, H. R., Schakkal, A. & Cherfan, G. Intravitreal bevacizumab for retinal capillary hemangioblastoma: A case series and literature review. *Can. J. Ophthalmol.* **49,** 450–457 (2014).

158. Gnarra, J. R. *et al.* Defective placental vasculogenesis causes embryonic lethality in VHL-deficient mice. *Proc. Natl. Acad. Sci. U. S. A.* **94,** 9102–9107 (1997).

159. Rankin, E. B., Tomaszewski, J. E. & Haase, V. H. Renal cyst development in mice with conditional inactivation of the von Hippel-Lindau tumor suppressor. *Cancer Res.* **66,** 2576–2583 (2006).

160. Haase, V. H., Glickman, J. N., Socolovsky, M. & Jaenisch, R. Vascular tumors in livers with targeted inactivation of the von Hippel-Lindau tumor suppressor. *Proc. Natl. Acad. Sci. U. S. A.* **98,** 1583–1588 (2001).

161. Ma, W. *et al.* Hepatic vascular tumors, angiectasis in multiple organs, and impaired spermatogenesis in mice with conditional inactivation of the VHL gene. *Cancer Res.* **63,** 5320–5328 (2003).

162. van Rooijen, E. *et al.* Zebrafish mutants in the von Hippel-Lindau tumor suppressor display a hypoxic response and recapitulate key aspects of Chuvash polycythemia. *Blood* **113,** 6449–6460 (2009).

163. van Rooijen, E. *et al.* von Hippel-Lindau tumor suppressor mutants faithfully model pathological hypoxia-driven angiogenesis and vascular retinopathies in zebrafish. *Dis. Model. Mech.* **3,** 343–353 (2010).

164. Noonan, H. R. *et al.* Loss of vhl in the zebrafish pronephros recapitulates early stages of human clear cell renal cell carcinoma. *Dis. Model. Mech.* **9,** 873–884 (2016).

165. Fisher, S. *et al.* A scalable, fully automated process for construction of sequence-ready human exome targeted capture libraries. *Genome Biol.* **12,** R1 (2011).

166. Cibulskis, K. *et al.* Sensitive detection of somatic point mutations in impure and heterogeneous cancer samples. *Nat. Biotechnol.* **31,** 213–219 (2013).

167. Beroukhim, R. *et al.* Assessing the significance of chromosomal aberrations in cancer: methodology and application to glioma. *Proc. Natl. Acad. Sci. U. S. A.* **104,** 20007–20012 (2007).

168. Mermel, C. H. *et al.* GISTIC2.0 facilitates sensitive and confident localization of the targets of focal somatic copy-number alteration in human cancers. *Genome Biol.* **12,** R41 (2011).

169. Cade, L. *et al.* Highly efficient generation of heritable zebrafish gene mutations using homo-and heterodimeric TALENs. *Nucleic Acids Res.* **40,** 8001–8010 (2012).

170. Sommer, C., Straehle, C., Koethe, U. & Hamprecht, F. A. in *8th IEEE International Symposium on Biomedical Imaging (ISBI 2011)* (2011).

171. Kamentsky, L. *et al.* Improved structure, function and compatibility for CellProfiler: modular high-throughput image analysis software. *Bioinformatics* **27,** 1179–1180 (2011).

172. Thompson, M. A. *et al.* The cloche and spadetail genes differentially affect hematopoiesis and vasculogenesis. *Dev. Biol.* **197,** 248–269 (1998).

173. Shin, J. T., Pomerantsev, E. V, Mably, J. D. & MacRae, C. a. High-resolution cardiovascular function confirms functional orthology of myocardial contractility pathways in zebrafish. *Physiol. Genomics* **42,** 300–309 (2010).

174. Crystal, A. S. *et al.* Patient-derived models of acquired resistance can identify effective drug combinations for cancer. *Science* **346,** 1480–1486 (2014).

175. Liu, X. *et al.* ROCK inhibitor and feeder cells induce the conditional reprogramming of epithelial cells. *Am. J. Pathol.* **180,** 599–607 (2012).

176. Pérez-Carro, R., Cauli, O. & López-Larrubia, P. Multiparametric magnetic resonance in the assessment of the gender differences in a high-grade glioma rat model. *EJNMMI Res.* **4,** 44 (2014).

177. Provencher, S. W. Automatic quantitation of localized in vivo 1H spectra with LCModel. *NMR Biomed.* **14,** 260–264 (2001).

178. Feldman, A. T. & Wolfe, D. Tissue processing and hematoxylin and eosin staining. *Methods Mol. Biol.* **1180,** 31–43 (2014).

179. Vortmeyer, A. O. *et al.* Somatic point mutation of the wild-type allele detected in tumors of patients with VHL germline deletion. *Oncogene* 1167–1170 (2002).

180. Beckner, M. E. *et al.* Loss of heterozygosity reveals non-VHL allelic loss in hemangioblastomas at 22q13. *Hum. Pathol.* **35,** 1105–1111 (2004).

181. Wilson, P. A., Gardner, S. D., Lambie, N. M., Commans, S. A. & Crowther, D. J. Characterization of the human patatin-like phospholipase family. *J. Lipid Res.* **47,** 1940–1949 (2006).

182. Kumari, M. *et al.* Adiponutrin functions as a nutritionally regulated lysophosphatidic acid acyltransferase. *Cell Metab.* **15,** 691–702 (2012).

183. Zack, T. I. *et al.* Pan-cancer patterns of somatic copy number alteration. *Nat. Genet.* **45,** 1134–1140 (2013).

184. Greenspan, P., Mayer, E. P. & Fowler, S. D. Nile red: a selective fluorescent stain for intracellular lipid droplets. *J. Cell Biol.* **100,** 965–973 (1985).

185. Chazotte, B. Labeling nuclear DNA using DAPI. *Cold Spring Harb. Protoc.* (2011).

186. Resh, M. D. Covalent lipid modifications of proteins. *Curr. Biol.* **23,** R431-435 (2013).

187. Zhou, F., Xue, Y., Yao, X. & Xu, Y. CSS-Palm: palmitoylation site prediction with a clustering and scoring strategy (CSS). *Bioinformatics* **22,** 894–896 (2006).

188. Carter, S. L. *et al.* Absolute quantification of somatic DNA alterations in human cancer. *Nat. Biotechnol.* **30,** 413–421 (2012).

189. Walmsley, S. R. *et al.* Neutrophils from patients with heterozygous germline mutations in the von Hippel Lindau protein (pVHL) display delayed apoptosis and enhanced bacterial phagocytosis. *Blood* **108,** 3176–3178 (2006).

190. Alexandrov, L. B. *et al.* Signatures of mutational processes in human cancer. *Nature* **500,** 415–421 (2013).

191. Gläsker, S. *et al.* Reconsideration of biallelic inactivation of the VHL tumour suppressor gene in hemangioblastomas of the central nervous system. *J. Neurol. Neurosurg. Psychiatry* **70,** 644–648 (2001).

192. Cai, Y. *et al.* Loss of Chromosome 8p Governs Tumor Progression and Drug Response by Altering Lipid Metabolism. *Cancer Cell* **29,** 751–766 (2016).

193. Romeo, S. *et al.* Genetic variation in PNPLA3 confers susceptibility to nonalcoholic fatty liver disease. *Nat. Genet.* **40,** 1461–1465 (2008).

194. Burza, M. A. *et al.* PNPLA3 I148M (rs738409) genetic variant is associated with hepatocellular carcinoma in obese individuals. *Dig. Liver Dis.* **44,** 1037–1041 (2012).

195. Yung, Y. C., Stoddard, N. C., Mirendil, H. & Chun, J. Lysophosphatidic Acid signaling in the nervous system. *Neuron* **85,** 669–682 (2015).

196. Bollu, L. R. *et al.* Intracellular activation of EGFR by fatty acid synthase dependent palmitoylation. *Oncotarget* **6,** 34992–5003 (2015).

197. Baenke, F., Peck, B., Miess, H. & Schulze, A. Hooked on fat: the role of lipid synthesis in cancer metabolism and tumour development. *Dis. Model. Mech.* **6,** 1353–1363 (2013).

198. Maher, E. & Kaelin, W. G. von Hippel-Lindau Disease. *Medicine (Baltimore).* **76,** 381–391 (1997).

199. Majmundar, A. J., Wong, W. J. & Simon, M. C. Hypoxia-inducible factors and the response to hypoxic stress. *Mol. Cell* **40,** 294–309 (2010).

200. Vanharanta, S. *et al.* Epigenetic expansion of VHL-HIF signal output drives multiorgan metastasis in renal cancer. *Nat. Med.* **19,** 50–56 (2013).

201. Shen, C. *et al.* Genetic and functional studies implicate HIF1α as a 14q kidney cancer suppressor gene. *Cancer Discov.* **1,** 222–235 (2011).

202. Rankin, E. B. *et al.* Hypoxia-inducible factor-2 regulates vascular tumorigenesis in mice. *Oncogene* **27,** 5354–5358 (2008).

203. Kaelin, W. G. Treatment of kidney cancer: Insights provided by the VHL tumor-suppressor protein. in *Cancer* **115,** 2262–2272 (2009).

204. Rathmell, W. K. & Chen, S. VHL inactivation in renal cell carcinoma: implications for diagnosis, prognosis and treatment. *Expert Rev. Anticancer Ther.* **8,** 63–73 (2008).

205. Zimmer, M. *et al.* Small-molecule inhibitors of HIF-2a translation link its 5'UTR iron-responsive element to oxygen sensing. *Mol. Cell* **32,** 838–848 (2008).

206. Sanchez, M., Galy, B., Muckenthaler, M. U. & Hentze, M. W. Iron-regulatory proteins limit hypoxia-inducible factor-2alpha expression in iron deficiency. *Nat. Struct. Mol. Biol.* **14,** 420–426 (2007).

207. Anderson, S. a *et al.* The IRP1-HIF-2α Axis Coordinates Iron and Oxygen Sensing with Erythropoiesis and Iron Absorption. *Cell Metab.* **17,** 282–290 (2013).

208. Ghosh, M. C. *et al.* Deletion of iron regulatory protein 1 causes polycythemia and pulmonary hypertension in mice through translational derepression of HIF2α. *Cell Metab.* **17,** 271–281 (2013).

209. Wilkinson, N. & Pantopoulos, K. IRP1 regulates erythropoiesis and systemic iron homeostasis by controlling HIF2a mRNA translation. *Blood* **122,** 1658–1669 (2013).

210. Kajimura, S., Aida, K. & Duan, C. Understanding hypoxia-induced gene expression in early development: in vitro and in vivo analysis of hypoxia-inducible factor 1-regulated zebra fish insulin-like growth factor binding protein 1 gene expression. *Mol. Cell. Biol.* **26,** 1142–1155 (2006).

211. Rojas, D. A. *et al.* Cloning of hif-1alpha and hif-2alpha and mRNA expression pattern during development in zebrafish. *Gene Expr. Patterns* **7,** 339–345 (2007).

212. Paffett-Lugassy, N. *et al.* Functional conservation of erythropoietin signaling in zebrafish. *Blood* **110,** 2718–2726 (2007).

213. Santhakumar, K. *et al.* A zebrafish model to study and therapeutically manipulate hypoxia signaling in tumorigenesis. *Cancer Res.* **72,** 4017–4027 (2012).

214. Haase, V. H. Regulation of erythropoiesis by hypoxia-inducible factors. *Blood Rev.* **27,** 41–53 (2013).

215. Krock, B. L., Skuli, N. & Simon, M. C. Hypoxia-induced angiogenesis: good and evil. *Genes Cancer* **2,** 1117–1133 (2011).

216. Gruber, M. *et al.* Acute postnatal ablation of Hif-2alpha results in anemia. *Proc. Natl. Acad. Sci. U. S. A.* **104,** 2301–2306 (2007).

217. Lawson, N. D. & Weinstein, B. M. In vivo imaging of embryonic vascular development using transgenic zebrafish. *Dev. Biol.* **248,** 307–318 (2002).

218. Murayama, E. *et al.* Tracing hematopoietic precursor migration to successive hematopoietic organs during zebrafish development. *Immunity* **25,** 963–975 (2006).

219. Kim, H. C. *et al.* Sunitinib treatment for metastatic renal cell carcinoma in patients with von hippel-lindau disease. *Cancer Res. Treat.* **45,** 349–353 (2013).

220. Jimenez, C. *et al.* Use of the tyrosine kinase inhibitor sunitinib in a patient with von Hippel-lindau disease: Targeting angiogenic factors in pheochromocytoma and other von Hippel-Lindau disease-related tumors. *J. Clin. Endocrinol. Metab.* **94,** 386–391 (2009).

221. Roma, A. *et al.* First-Line sunitinib in patients with renal cell carcinoma (RCC) in von Hippel-Lindau (VHL) disease: clinical outcome and patterns of radiological response. *Fam. Cancer* **2,** 309-316 (2014).

222. Matin, S. F. Words of wisdom: re: pilot trial of sunitinib therapy in patients with von hippel-lindau disease. *Eur. Urol.* **63,** 770 (2013).

223. Zon, L. I. & Peterson, R. T. In vivo drug discovery in the zebrafish. *Nat. Rev. Drug Discov.* **4,** 35–44 (2005).

224. Verdine, G. L. & Hilinski, G. J. Stapled peptides for intracellular drug targets. *Methods Enzymol.* **503,** 3–33 (2012).

225. Delmore, J. E. *et al.* BET bromodomain inhibition as a therapeutic strategy to target c-Myc. *Cell* **146,** 904–917 (2011).

226. Scheuermann, T. H. *et al.* Allosteric inhibition of hypoxia inducible factor-2 with small molecules. *Nat. Chem. Biol.* **9,** 271–276 (2013).

227. Skuli, N. *et al.* Endothelial HIF-2α regulates murine pathological angiogenesis and revascularization processes. *J. Clin. Invest.* **122,** 1427–1443 (2012).

228. Minamishima, Y. A. *et al.* Somatic inactivation of the PHD2 prolyl hydroxylase causes polycythemia and congestive heart failure. *Blood* **111,** 3236–3244 (2008).

229. Yanagisawa, M. *et al.* A novel potent vasoconstrictor peptide produced by vascular endothelial cells. *Nature* **332,** 411–415 (1988).

230. Haynes, W. G. & Webb, D. J. The endothelin family of peptides: local hormones with diverse roles in health and disease? *Clin. Sci. (Lond).* **84,** 485–500 (1993).

231. Iwanaga, Y. *et al.* Cardiac endothelin-1 plays a critical role in the functional deterioration of left ventricles during the transition from compensatory hypertrophy to congestive heart failure in salt-sensitive hypertensive rats. *Circulation* **98,** 2065–2073 (1998).

232. Schunemann, V., Huntoon, K. & Lonser, R. R. Personalized Medicine for Nervous System Manifestations of von Hippel-Lindau Disease. *Front. Surg.* **3,** 39 (2016).

233. Douglas, Y. L. *et al.* Pulmonary vein, dorsal atrial wall and atrial septum abnormalities in Podoplanin knockout mice with disturbed posterior heart field contribution. *Pediatr. Res.* **65,** 27–32 (2009).

234. Lowe, K. L. *et al.* Podoplanin and CLEC-2 drive cerebrovascular patterning and integrity during development. *Blood* **125,** 3769–3777 (2015).

235. Schacht, V. *et al.* T1a/podoplanin deficiency disrupts normal lymphatic vasculature formation and causes lymphedema. *EMBO J.* **22,** 3546–3556 (2003).

236. Fu, J. *et al.* Endothelial cell O-glycan deficiency causes blood / lymphatic misconnections and consequent fatty liver disease in mice. *J. Clin. Invest.* **118,** 3725–3737 (2008).

237. Herzog, B. H. *et al.* Podoplanin maintains high endothelial venule integrity by interacting with platelet CLEC-2. *Nature* **502,** 105–109 (2013).

238. Ramirez, M. I. *et al.* T1a, a lung type I cell differentiation gene, is required for normal lung cell proliferation and alveolus formation at birth. *Dev. Biol.* **256,** 61–72 (2003).

239. Hou, T. Z. *et al.* A distinct subset of podoplanin (gp38) expressing F4/80+ macrophages mediate phagocytosis and are induced following zymosan peritonitis. *FEBS Lett.* **584,** 3955–3961 (2010).

240. Peters, A. *et al.* Th17 cells induce ectopic lymphoid follicles in central nervous system tissue inflammation. *Immunity* **35,** 986–996 (2011).

241. Kerrigan, A. M. *et al.* CLEC-2 is a phagocytic activation receptor expressed on murine peripheral blood neutrophils. *J. Immunol.* **182,** 4150–4157 (2009).

242. Ernst, A. *et al.* Genomic and expression profiling of glioblastoma stem cell-like spheroid cultures identifies novel tumor-relevant genes associated with survival. *Clin. Cancer Res.* **15,** 6541–6550 (2009).

243. Peterziel, H. *et al.* Expression of podoplanin in human astrocytic brain tumors is controlled by the PI3K-AKT-AP-1 signaling pathway and promoter methylation. *Neuro. Oncol.* **14,** 426–439 (2012).

244. Durchdewald, M. *et al.* Podoplanin is a novel fos target gene in skin carcinogenesis. *Cancer Res.* **68,** 6877–6883 (2008).

245. Kunita, A., Kashima, T. G., Ohazama, A., Grigoriadis, A. E. & Fukayama, M. Podoplanin is regulated by AP-1 and promotes platelet aggregation and cell migration in osteosarcoma. *Am. J. Pathol.* **179,** 1041–1049 (2011).

246. Kato, Y. *et al.* Enhanced expression of Aggrus (T1alpha/podoplanin), a platelet-aggregation-inducing factor in lung squamous cell carcinoma. *Tumour Biol.* **26,** 195–200 (2005).

247. Kimura, N. & Kimura, I. Podoplanin as a marker for mesothelioma. *Pathol. Int.* **55,** 83–86 (2005).

248. Ordóñez, N. G. D2-40 and podoplanin are highly specific and sensitive immunohistochemical markers of epithelioid malignant mesothelioma. *Hum. Pathol.* **36,** 372–380 (2005).

249. Kitano, H. *et al.* Podoplanin expression in cancerous stroma induces lymphangiogenesis and predicts lymphatic spread and patient survival. *Arch. Pathol. Lab. Med.* **134,** 1520–1527 (2010).

250. Pusztaszeri, M. P., Seelentag, W. & Bosman, F. T. Immunohistochemical expression of endothelial markers CD31, CD34, von Willebrand factor, and Fli-1 in normal human tissues. *J. Histochem. Cytochem.* **54,** 385–395 (2006).

251. Delikatny, E. J., Chawla, S., Leung, D.-J. & Poptani, H. MR-visible lipids and the tumor microenvironment. *NMR Biomed.* **24,** 592–611 (2011).

252. Padhani, A. R. *et al.* Diffusion-weighted magnetic resonance imaging as a cancer biomarker: consensus and recommendations. *Neoplasia* **11,** 102–125 (2009).

253. She, D., Yang, X., Xing, Z. & Cao, D. Differentiating Hemangioblastomas from Brain Metastases Using Diffusion-Weighted Imaging and Dynamic Susceptibility Contrast-Enhanced Perfusion-Weighted MR Imaging. *AJNR. Am. J. Neuroradiol.* (2016).

254. Metelo, A. M. *et al.* Pharmacological HIF2α inhibition improves VHL disease-associated phenotypes in zebrafish model. *J. Clin. Invest.* **125,** 1987–1997 (2015).

255. Albiñana, V. *et al.* Propranolol reduces viability and induces apoptosis in hemangioblastoma cells from von Hippel-Lindau patients. *Orphanet J. Rare Dis.* **10,** 118 (2015).

256. Roig, A. I. *et al.* Immortalized epithelial cells derived from human colon biopsies express stem cell markers and differentiate in vitro. *Gastroenterology* **138,** 1012-1021 (2010).

257. Van der Haegen, B. A. & Shay, J. W. Immortalization of human mammary epithelial cells by SV40 large T-antigen involves a two step mechanism. *In Vitro Cell. Dev. Biol.* **29A,** 180–182 (1993).

258. Wilson, N. K. *et al.* Combined Single-Cell Functional and Gene Expression Analysis Resolves Heterogeneity within Stem Cell Populations. *Cell Stem Cell* **16,** 712–724 (2015).

259. Isobe, T. *et al.* Proton magnetic resonance spectroscopy findings of hemangioblastoma. *Jpn. J. Radiol.* **28,** 318–321 (2010).